To the Graduate Council:

I am submitting herewith a dissertation written by Cheng Heng Zhang entitled "Soft X-ray Emission Spectroscopy and its Application in Dilute Al in Mg and LiAl Alloys." I have examined the final copy of this dissertation for form and content and recommend that it be accepted in partial fulfillment of the requirements for the degree of Doctor of Philosophy, with a major in Physics.

Thomas A. Callcott

Thomas A. Callcott, Major Professor

We have read this dissertation
and recommend its acceptance:

E T Arakawa

J R Thompson

R. H. Ritchie

J E Epperson

Accepted for the Council:

Lew Minkel

Vice Provost
and Dean of the Graduate School

SOFT X-RAY EMISSION SPECTROSCOPY AND ITS APPLICATION IN DILUTE AL IN MG AND LIAL ALLOYS

A Dissertation

Presented for the

Doctor of Philosophy

Degree

The University of Tennessee, Knoxville

Cheng Heng Zhang

March 1987

ACKNOWLEDGMENTS

I whish to express my sincere thanks to Dr. T. A. Callott for his guidance in completing this work. His determination to become involved in a new approach to some hard problems and his dedication to the project have inspired me to explore ways of solving the question and are greatly appreciated. Thanks are due also to Dr. D. L. Ederer, who with his wisdom, experience and attractive personality contributed much throughout this work; and to Dr. K. L. Tsang for his unselfish assistance. To the other members of my thesis committee, Dr. E. T. Arakawa, Dr. R. H. Ritchie, Dr. J. E. Spruiell and Dr. J. R. Thompson, I extend my appreciation for their participation and suggestions.

Many years of financial support were provided by the Department of Physics, the University of Tennessee. I acknowledge also the financial support provided by National Science Foundation, by the Science Alliance Centers of Excellence grant from the State of Tennessee, by the Department of Energy and by the National Bureau of Standards (NBS). Considerable thanks are due to the hospitality of all staff members at SURF II NBS; also to the

National Synchrotron Light Sourse of the Brookhaven National Laboratory, where part of this work was completd.

Finally, I wish to express my deepest thanks to my parents, Mr. & Mrs. An-ying and Ning-yee Zhang for their understanding and encouragement.

ABSTRACT

A new soft x-ray emission spectrometer designed for use with photon excitation from synchrotron light sources is described and characterized. Special design features, including a close-spaced input slit, large toroidal gratings, and a two-dimensional charge-coupled-device, Si-array based detector system, provide measuring efficiency 10^4 times greater than that of a conventional spectrometer in a 5-m Rowland circle design. Descriptions of the spectrometer's design and calibration procedures, and of the photon flux distribution through the beam line from the synchrotron light sources are emphasized.

Measurements of (1) the Mg double ionization L-satellite spectrum and the Al $L_{2,3}$ spectra for dilute alloys of 0.5%, 1.0%, and 2.0% Al in Mg, and of (2) the Al $L_{2,3}$ and Li K spectra for LiAl(50% - 50%) alloy have been made with greatly improved resolution. For dilute Al in Mg alloys, the spectra of the Mg satellite and of the Al impurity contain similar features associated with screening of the extra core hole, but are otherwise dissimilar. The threshold peak is broadended in both spectra. The L_3-L_1 intercore transition

in doubly ionized Mg is observed. A second, weak, high energy satellite is observed that may be produced by transitions from the $^1S_0$ state of the doubly ionized core levels.

For LiAl alloy, we have found extreme sensitivity of the spectral features for both Al $L_{2,3}$ and Li K emission to the presence of pure Li on the surfaces. The reproducible spectra have been compared with p-partial density of state (PDOS) for Li K emission and with (s + d)-PDOS for Al $L_{2,3}$ emission calculated by Asada et al. The match of Al $L_{2,3}$ with theoretical results is good except a broad bump centered at -2.5 eV from Fermi edge which shows the features of p-PDOS. It may imply a breakdown of the selection rules for a disordered alloy system. The fit between Li K spectrum and p-PDOS is poorer than for Al L spectrum. We attribute this effect to a strong transition matrix element effect on a PDOS calculation.

TABLE OF CONTENTS

SECTION		PAGE
I.	INTRODUCTION	1
	A. Historical Review	1
	B. Basic Principles of SXE Spectra	5
	C. Electron and Photon Excitation Sources	13
	D. The Synchrotron Radiation Source	15
	E. Scope of the Present Work	21
II.	THEORETICAL ASPECTS	23
	A. Soft X-ray Emission from Solids	23
	B. Synchrotron Radiation	36
	C. Photon Flux Distribution through Optical Elements	49
	D. The Rowland Circle	57
III.	SOFT X-RAY EMISSION SPECTROMETER	63
	A. Introduction	63
	B. Design Procedures	66
	C. MCP-CCD Detector System	74
	D. Performance of Spectrometer	92
IV.	BEAM LINE	97
	A. Beam Line design	97
	B. Flux Distribution and Power Load	100
	C. Photon Excitation	106
V.	SXE SPECTRA OF DILUTE AL IN MG AND LIAL ALLOYS	109
	A. Introduction	109
	B. Experimental Procedures	117
	C. Results and Discussion	126
LIST OF REFERENCES		145
APPENDIXES		156
Appendix A		157
Appendix B		160
VITA		167

LIST OF FIGURES

FIGURE		PAGE
1-1.	Diagram of Electron Energy Levels and Radiative Transitions in Solids	7
1-2.	Electron Inelastic Mean Free Paths for Aluminum	10
1-3.	Absorption Coefficient for Aluminum	11
1-4.	Synchrotron Radiation Spectra for 400 MeV, 700 MeV, 1.5 Gev, and 2.5 Gev Electrons in Ring	17
1-5.	The Vertical Angular Distribution of Parallel and Perpendicular Polarization Components of SR	19
2-1.	Partial Density of States for s-, p-, and d-Symmetry Electrons Calculated by Free Electron Model	27
2-2.	Typical SXE Spectrum for Simple Metal Mg	30
2-3.	Intensity Ratio, J_0/J, between Satellite Band and Main Band for Light Metals as a Function of r_s, the Electron Density Parameter	37
2-4.	Diagram of Vertical and Horizontal Divergence of SR for the Beam Line	42
2-5.	Flux Distribution Function $F_1(\lambda_c / \lambda)$	50
2-6.	Flux Distribution Function $F_4(\lambda_c / \lambda)$	51
2-7.	Ratio Curves of Parallel and Perpendicular Components to Total Radiation over All Vertical Divergence from the SR Source	52
2-8.	Diagram of Polarization Components at Interface between Vacuum and Medium	55

FIGURE PAGE

2-9. Diagram of the Rowland Circle Geometry 58

3-1. Diagram of Synchrotron Light Beam Line Used for Photon Excitation of Soft X-ray and the SXE Spectrometer 65

3-2. Rowland Circle Geometry 68

3-3. Diagram of Soft X-ray Spectrometer with Cross Section Taken on the Optic Axis 69

3-4. Focusing Properties of Toroidal Gratings from Ray Tracing Studies 72

3-5. Resolution of Four Gratings Installed in Spectrometer Using 50μm Input Slit Width 75

3-6. Diagram of Detector System 77

3-7. Diagram of Data-acquisition Electronics 80

3-8. Average Lateral Response of the 2D Detector in the Dispersion Direction,Obtained by Averaging over the Orthogonal Direction Using Method B in Appendix B 84

3-9. Same Response Curve Using Method C in Appendix B 85

3-10. Aluminum $L_{2,3}$ Spectra Assembled from Data Obtained in Three Adjacent Spectral Regions 87

3-11. Signal-to-noise Ratio for the Detector System .. 91

3-12. Silicon $L_{2,3}$ Spectra Showing Primary Spectrum and Satellite with Approximately 1.0% the Intensity of the Primary Spectrum 93

4-1. Fluxes Available for Excitation of Samples at the NBS SURF II Synchrotron Light Facility 101

FIGURE PAGE

4-2. Flux Distributions I at the BNL NSLS VUV Ring .. 103

4-3. Flux Distributions II at the BNL NSLS VUV Ring . 104

4-4. Li Spectrum Obtained with (a) 600 eV e-beam Excitation, and (b) Photon Excitation 107

5-1. The SXE Spectrum of 1.0% Al in Mg Alloy 120

5-2. The Mg L Satellite and Al $L_{2,3}$ Spectra for Mg and 0.5%, 1.0%, and 2.0% Al in Mg Alloys 122

5-3. The Al $L_{2,3}$ Impurity Spectra for Al in Mg Alloys after Subtraction of the Mg Satellite Spectrum . 123

5-4. The Mg Satellite Spectrum Compared to the Primary Mg $L_{2,3}$ Spectrum 128

5-5. The Al Impurity Spectrum for the 1.0% Alloy Compared to the $L_{2,3}$ Spectra of Pure Al and Mg .. 132

5-6. The Threshold Region of the Al Impurity Spectrum Compared to Pure Al and Mg 133

5-7. The Mg L Satellite, the 1.0% Al $L_{2,3}$, and KLV Auger Spectra Compared 135

5-8. The Total SXE Spectrum from LiAl (50%-50%) 139

5-9. The Li K Spectrum for LiAl (50%-50%) and the Calculated p-PDOS of Li in LiAl 140

5-10. The Al $L_{2,3}$ Spectrum for LiAl (50%-50%) and the Calculated (s+d)-PDOS of Al in LiAl 141

A-1. CCD-MCP Detector System and the Rowland Circle Geometry 158

A-2. Scheme of Measurement for Transmission Factor, T(n), of MCP-CCD System 162

LIST OF TABLES

TABLE		PAGE
1-1.	Soft X-ray Energies (eV) of Prominent Transitions for the Elements with Z < 26	9
2-1.	Energy Separations between $^3P_2$ and $^3P_{1,0}$, $^1D_2$, $^1S_0$ States for Free Ions of Al and Mg	35
2-2.	Different Polarization Conditions for General Harmonic Wave	44
A-1.	Calculated Results for Projection of $\Delta\ell$ on Detector System	158

I. INTRODUCTION

A. Historical Review

Soft x-ray emission (SXE) spectroscopy of solids has a long history, going back as far as that of the band theory of solids [1.1]. The pioneer experiments were performed by Siegbahn, Skinner, O'Brian, Farineau and their co-workers [1.2,1.3]. In their early work, the SXE spectra for light metals were recorded photographically by a grazing incidence spectrometer with a concave grating. Mott later described these results, saying, "What stood out a mile was that these emission bands had sharp upper limits, just as the Sommerfeld-Bethe theory predicted" [1.1]. In later years, many complex questions relating to the SXE band spectra from solids were defined, discussed and ultimately resolved. These included many questions of theoretical interpretation, such as the many-electron nature of the transitions, and the time scales of importance to the processes [1.4], as well as problems of experimental technique. We briefly summarize some of these developments below.

The early interpretation of SXE band spectra was very

simple [1.5]. Using the one electron approximation and ground state wave functions for both the core levels and band states, transmission probabilities were calculated which led to intensity distributions of the form [1.6]

$$I(\omega) \propto \omega^3 \; |\langle \psi_k | \hat{r}_j | \psi_{core} \rangle|^2 \; N(E) \qquad (1\text{-}1)$$

where, ψ_{core} is the core state, ψ_k is the valence and/or conduction band state, N(E) is the partial density of band states (PDOS) selected from the total density of states by the dipole selection rule, and ω is the frequency of emitted light. The SXE spectra were thus interpreted in terms of a PDOS multiplied by a dipole transition probability.

Many modifications have since been made to the simple theory, particularly in the case of metal spectra. Mahan, in 1967, and Nozieres and deDominicis (MND) used many body theory to account for sharp anomalous peaks at the x-ray absorption and emission edges in simple metals [1.7, 1.8]. Measurements of edge widths and of separation between the absorption and emission edges of Li and Na confirmed calculations suggesting that lifetime broadening and partial lattice relaxation about the core hole would have important effects on metallic spectra [1.9,1.10,1.11]. Early workers

had found good agreement between experimental spectra and PDOS's calculated from gound state wavefunctions[1.6]. It was soon noted that different PDOS and less satisfactory agreement would be obtained if calculations were made with wavefunctions calculated with the core hole present. Mahan, von Barth and Grossman resolved the question with many body calculations which led them to propose the final state rule (FSR)[1.12,1.13].

The FSR states that spectra produced by electronic transitions will always resemble one-electron transition PDOS's calculated with the final state wavefunctions. Thus the primary SXE band spectra, whose final state is the ground state of the solid, may be interpreted with the wavefunctions of ordinary band theory. Several other types of spectra are produced by transitions that leave a core hole in the final state, and should be interpreted using wavefunctions which include the extra screening charge around the extra core hole. The theoretical calculations show that for metals, the screening charge associated with the presence of a core hole will enhance the s-PDOS near the bottom of the conduction band and produce an extra peak at the low energy edge of the SXE spectra of simple metals. Such effects are seen in the

SXE spectra of impurities with extra core charges, in the high energy satellite spectra produced by transitions to doubly ionized core levels, and in Auger spectra in which one electron makes a transition between core levels while a second is ejected from the valence band[1.14]. In the experimental part of this thesis, impurity and satellite spectra will be presented and compared to the KLV Auger spectra of other workers[1.12,1.13,1.14].

SXE band spectroscopy, in principle, has a great advantage for the study of alloys, because it gives transition PDOS's localized on one constituent of the alloy. In a review paper, Sellmyer has summarized experimental studies of the electronic structure of metal alloys, including the results of SXE studies[1.15]. Unfortunately, there is to date no theory capable of providing a completely satisfactory interpretation of the observed data for alloys. In recent years Green's function calculations of the KKR (Korringa, Kohn, and Rostoker) type using the coherent potential approximation have been developed which make calculations possible for random substitutional alloys [1.16,1.17,1.18].

Until very recently there have been few improvements in

the design of SXE spectrometers. These conventional, grazing incidence spectrometers, using a Rowland circle geometry, spherical concave gratings, a scanned output slit with photomultiplier detection and conventional vacuum technology have been described in Samson's book on VUV spectroscopy [1.19]. Very recently, great improvements in the conventional design have been made through the use of UHV vacuum methods, toroidal diffraction gratings, and microchannel plate (MCP) enhanced, two dimensional, CCD type Si diode detectors [1.20]. Another recent, high efficiency design has employed a fixed angle, toroidal grating design with holographic gratings to reduce abberrations,and a linear diode array detector [1.21].

B. Basic Principles of SXE Spectra

Soft x-ray emission from a metal alloy results from the radiative decay of core holes localized on the atoms of one constituent of the alloy, when electrons in valence or conduction bands drop into the core hole states. Thus SXE spectroscopy provides information about the filled states in the valence or conduction bands of the alloy.

There are several special features that make SXE spectroscopy a particularly powerful tool for the study of metals and alloys.

1) Since the dipole selection rules govern the radiative transitions, the energy spectrum of the photons emitted is expected to reflect a partial density of states (PDOS) of the valence or conduction band, in which the particular angular momentum symmetry depends on the symmetry of the inner level. Thus transitions to s-core states provide a measure of the p-PDOS and transitions to p-core states provide a measure of the (s+d)-PDOS as illustrated in Figure 1-1. This figure also illustrates the notation commonly used to identify core levels in x-ray and other core level spectroscopies.

2) Because the core states occupy a small fraction of the atomic volume, and different constituents in a metal alloy have different core level depths, SXE spectroscopy provides PDOS's characteristic of a small region localized near individual constituent atoms in the alloy.

3) Grazing incidence spectrometers, working in the photon energy range from 20 eV to 1000 eV, make possible the measurement of spectra from many light elements that are not accessible either to hard x-ray spectromenters using crystal

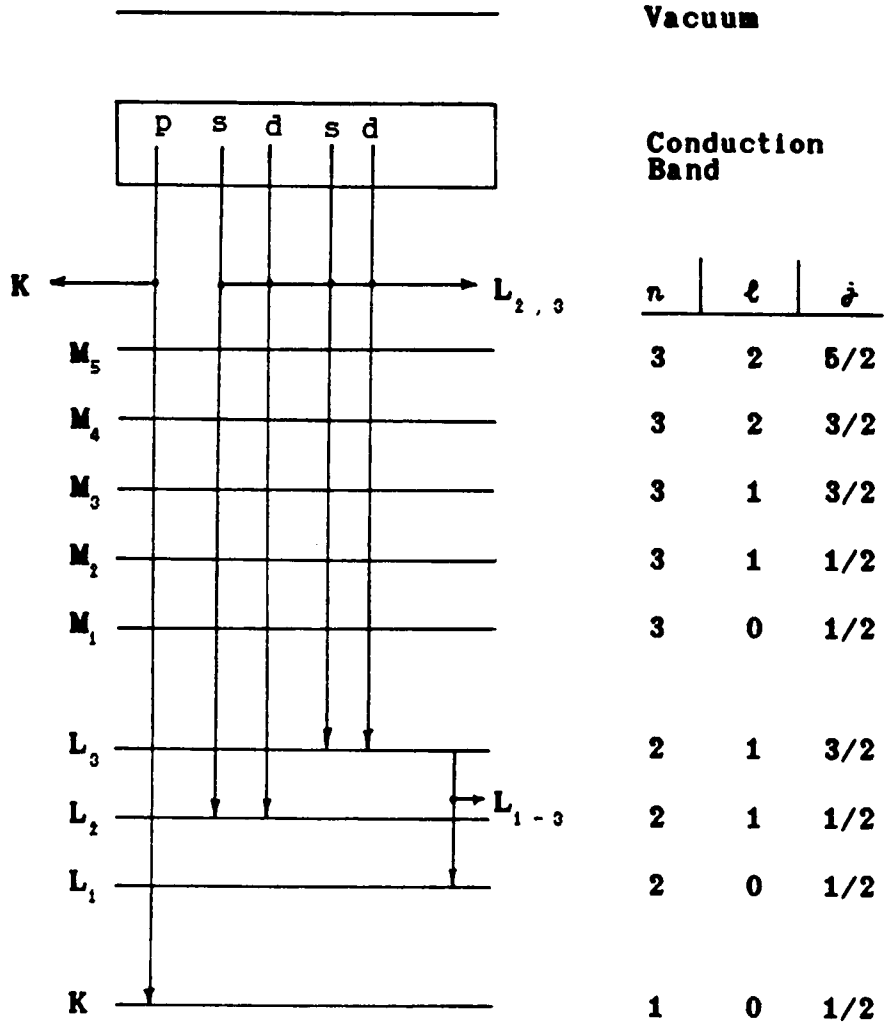

Fig.1-1
Diagram of electron energy levels and radiative transitions in solids. The quantum numbers,n,l,j are given to each levels labeled by K, L, and M. The spectrum for intercore transition between L_2 and L_1 is designated by L_{1-3}.

dispersing elements or to more conventional ultraviolet and visible spectrometers. Table 1-1 provides data that illustrates the range in which K, L and M spectra of various elements are accessible to a soft x-ray spectrometer operating over this range of photon energies [1.22].

4) SXE spectroscopy is less surface sensitive than electron spectroscopies such as x-ray photoemission spectroscopy (XPS) and Auger electron spectroscopy (AES), and thus provides data characteristic of the bulk properties of the alloy. Electron elastic mean free paths, as illustrated in Figure 1-2 for Al, are generally less than 10 Å for a broad range of energies near 100 eV so that the electron spectroscopies provide information from only the top few layers of atoms[1.23]. In contrast, the mean free path for photons is typically much larger. For Al at 100 eV it is almost 50 larger than that of electrons at the same energy, as may be seen from the absorption coefficients for Al shown in Figure 1-3[1.24].

SXE spectroscopy also has some characteristic problems: 1) All SXE spectra are weakly emitted because the radiative yields are low, ranging from 10^{-2} to 10^{-4} in the soft x-ray range. Most core-excited atoms de-excite by non-radiative Auger processes. Krause has compiled data for radiative and

Table 1-1
Soft x-ray energies (eV) of prominent transitions for the elements with Z < 26 [1.22].

Element	$K\alpha_1$ $K\alpha_2$ $[2p-1s]$	$K\beta_{1,3}$ $[3p-1s]$	$K\beta_{2,5}$ $[4p-1s]$	L_I $L_{II,III}$ $[2p-2s]$	$L\beta_{3,4}$ $[3p-2s]$	$L\iota$ $L\eta$ $[3s-2p]$	$L\alpha_{1,2}$ $L\beta_1$ $[3d-2p]$
Carbon	277·7						
Nitrogen	392·4						
Oxygen	524·9						
Fluorine	676·8						
Magnesium	1253·6	1302·2		39·2		49·3	
Aluminium	1486·7 1486·3	1557·4		42·8		72·4	
Silicon	1740·0 1739·4	1835·9				91·5	
Titanium	4510·8 4504·9	4931·8	4962·3			395·3 401·3	452·2 458·4
Vanadium	4952·2 4944·6	5427·3	5462·9		585·0	446·5 453·5	511·3 519·2
Iron	6403·8 6390·8	7058·0	7108·1		792·0	615·2 628·0	705·0 718·5

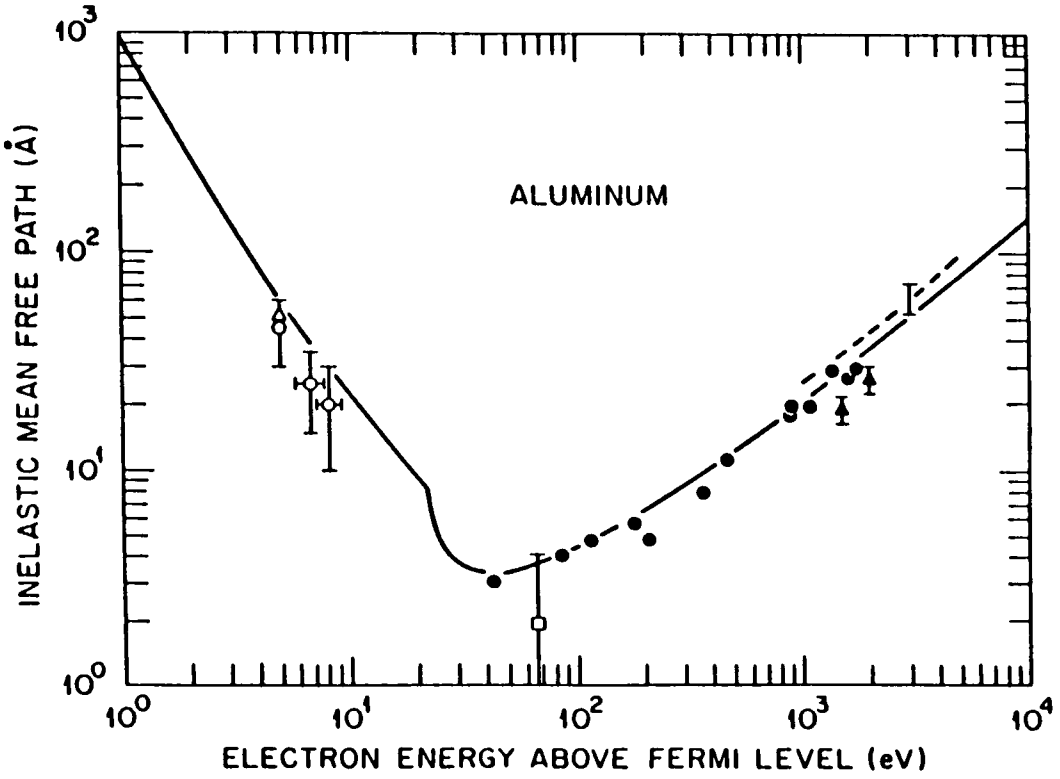

Fig.1-2
Electron inelastic mean free paths for Aluminum [1.23].

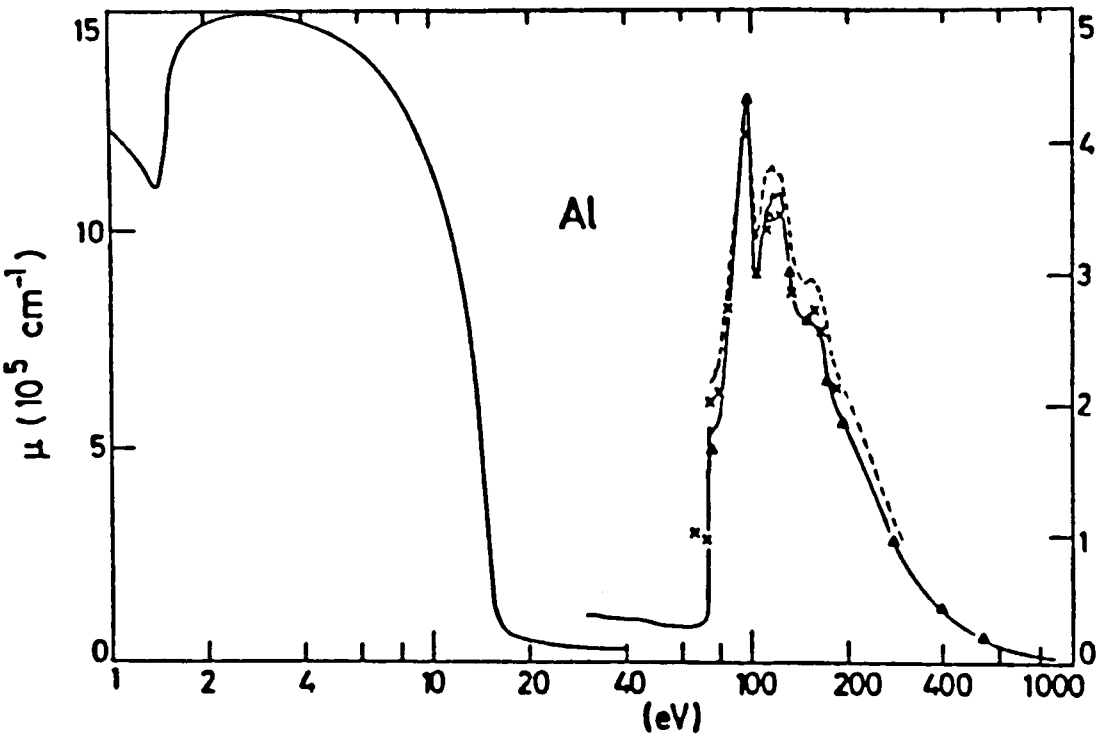

Fig.1-3
Absorption coefficient for Aluminum [1.24].

non-radiative yields for the K and L levels of elements below Z= 20[1.25]. A new SXE spectrometer with very high efficiency described later in the first part of this dissertation was designed specifically to compensate for these low yields, so that SXE spectroscopy could be made into a routinely useful experimental tool.

2) In some cases, yields are so low that SXE spectra are not observed at all. Thus L_1 spectra are never observed [1.25] and L_2 spectra are weaker than would be expected from the statistical weights of the L_2 and L_3 levels. For each shell, the lower lying levels tend to be filled by non-radiative Koster-Kronig transitions from higher levels in the shell so that the strongest SXE spectra are generally those that result from transitions to the highest level within each shell[1.7]. In practice, only transitions to 1s (K-spectra), 2p ($L_{2,3}$ -spectra), and 3d ($M_{4,5}$ -spectra) are observed. This severely limits the amount of PDOS information that can be obtained from a limited spectral range.

3) In alloys containing several constituents, there may be overlap between various spectra of experimental interest. In the studies on the Al-Mg alloys discussed here, such overlap occurs between the $L_{2,3}$ spectrum of dilute Al in Mg and the

satellite spectrum of Mg which results from transitions to a doubly ionized 2p core level. In this case, the two spectra could be separated using data from pure Mg. In other cases, it may be possible to separate such spectra by selectively ionizing particular core levels using monochromatized synchrotron photons.

C. Electron and Photon Excitation Sources

Core holes may be produced by either energetic electrons or by photons from a synchrotron light source. Other photon sources do not have sufficient intensity for general use in the SXE region. Electron excitation sources are compact and relatively inexpensive. The electron energy and incidence angle are easily controlled. This allows some control over the excitation depth, so that a degree of sensitivity to surface versus bulk properties can be obtained. Some microprobe capability can also be achieved if sufficient sensitivity in the spectrometer is available.

But electron beam excitation has two serious drawbacks. The low excitation efficiency and generally shallow excitation depths make studies of fragile materials difficult[1.23].

Such materials are rapidly degraded by the electron beam intensities normally used to produce spectra. A second drawback is that electron excitation generally excites many core levels at the same time so that quite complex and overlapping spectra may be produced in samples with many constituents. Nevertheless, most SXE spectroscopy done to date has employed electron excitation sources[1.21].

Photon excitation from synchrotron sources has several potential advantages. Photon excitation generally produces core holes over depths that are well matched to the escape depths of SXE photons. Using monochromatized light, particular core levels may be selected for excitation. If a band of photon energies between the binding energy of a core level of interest and the next deeper level is used, very high excitation efficiencies can be obtained so that excitation is produced with a minimum of energy deposition to fragile materials. Finally, there are no problems with charging of insulating samples. Nevertheless, there have been very few SXE studies reported which used sychrotron light excitation[1.27]. It was precisely to take advantage of these potential advantages that the experimental facility described herein was built.

There are at least two major disadvantages to the use of photon excitation. One is the inconvenience imposed by operating at a synchrotron light source. Offsite operation is expensive, facilities are crowded, and stringent vacuum and radiation shielding requirements make some types of experiment difficult. Photon excitation brings a second, very difficult problem of suppressing scattered light from the exciting radiation that can easily exceed the intensities of the SXE spectra unless great care is taken.

D. The Synchrotron Radiation Source

Synchrotron radiation (SR) is created when charged particles, electrons or positrons, moving at relativistic velocities, are bent by the magnets in the storage ring. The unique properties of synchrotron radiation have resulted in the explosive growth of interest in using synchrotron radiation as a light source. These properties include[1.28]:

1) A continuous spectrum with high intensity extending from the infrared to the x-ray region,

2) Highly polarized light,

3) Natural collimation,

4) Pulsed time structure,

5) Small source size,

6) Emission intensities that can be accurately calculated from the beam energy, current and bending radius.

Synchrotron radiation spectra for 400 MeV, 700 MeV, 1.5 GeV, and 2.5 GeV electrons are illustrated in Fig. 1-4. The unit of flux is the number of photons per second per horizontal milliradian for 1% $\Delta\lambda/\lambda$ and over all vertical aperture. These spectra provide four orders of photon intensity above that of conventional light sources in the spectral region (2000 Å-0.2 Å, or 6 eV-60 KeV). For work in the soft x-ray region below 1 KeV, it is desirable to work without the added complications of the harder radiation above 1 or 2 KeV. Consequently our beamline is located on the VUV ring at NSLS (750MeV) rather than on the 2.5 GeV X-ring.

Most beam lines operating at energies above 1 or 2 KeV use crystal monochromators, and those operating below about 1 KeV use grazing incidence, grating monochromators to obtain wavelength selectivity[1.28]. More recently, synthetic multilayers such as C-W have been used as bandpass elements on some beamlines[1.30]. Absorption filters, made from monolayer or multilayer metals may also be used as a

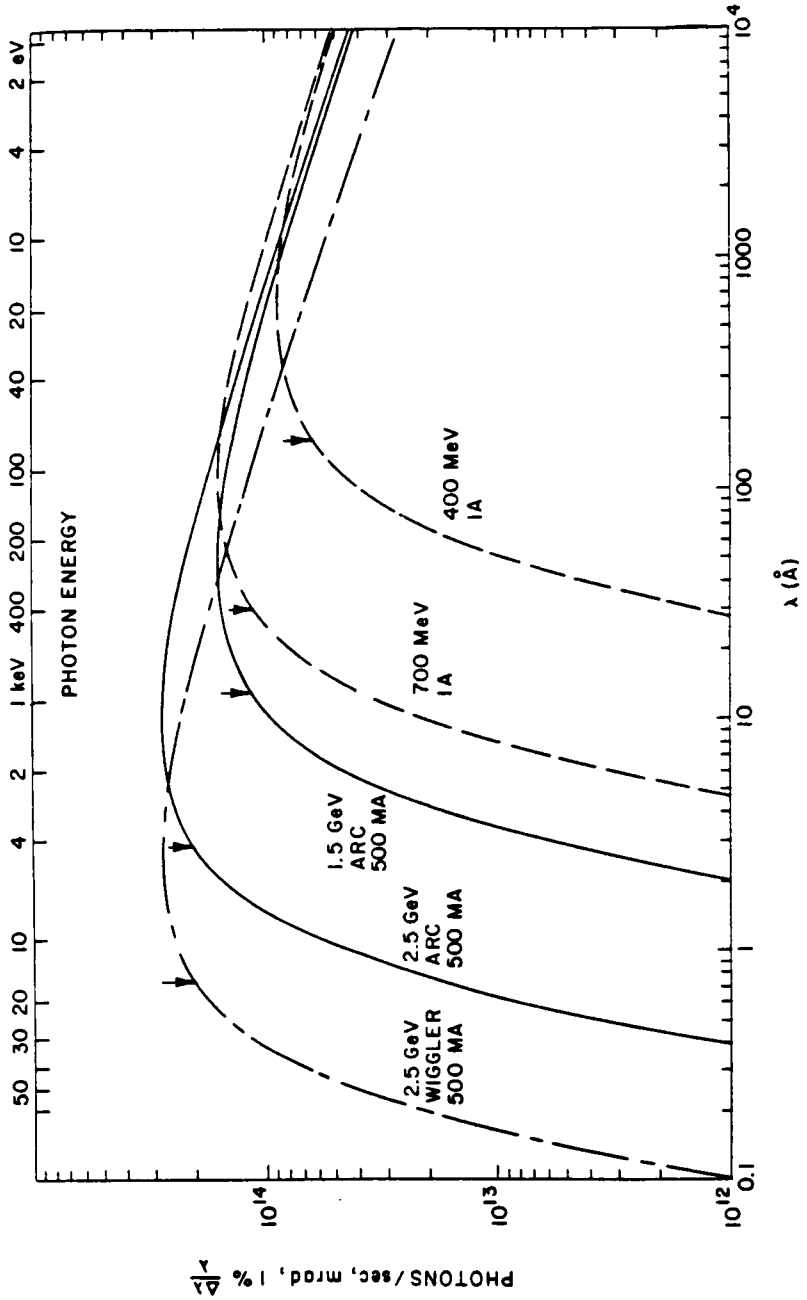

Fig.1-4
Synchrotron radiation spectra for 400 MeV, 700 MeV, 1.5 GeV, and 2.5 GeV electrons in ring [1.29].

broad bandpass element (see Fig. 4-2 and Fig. 4-3)[1.31].

The SXE photon excitation work to date has used a white light beam and one or more such absorption filters. In order to obtain the advantages provided by excitation with monochromatized light, a transmission grating monochromator has been designed and is now under construction for our beamline. The design is based on a transmission grating spectrometer developed at Oak Ridge National Laboratory [1.31-1.33].

The vertical angular distribution of parallel and perpendicular polarization components of synchrotron radiation is shown in Figure 1-5. The most prominant feature is that, on the orbital plane, the spectrum is completely plane polarized with the electric vector parallel to the plane. Away from the plane, SR is strongly collimated in a cone with very small vertical angular divergence. For example, the angular half width is less than 6.8 mrad for the NSLS 750 MeV VUV ring [1.28].

In the storage ring, electrons circulate in packets or bunches. In the NSLS VUV ring, the orbital period is 1.6 x 10^{-7} sec and up to nine bunches can be circulated simultaneously, giving radiation pulses with intervals of

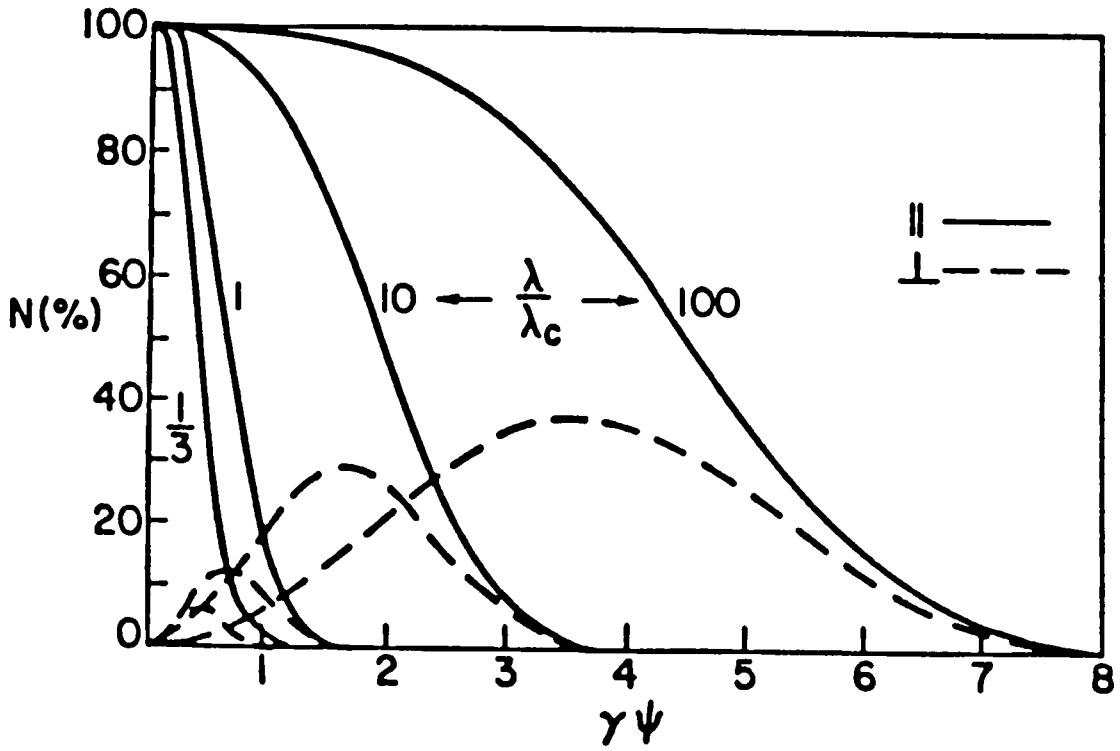

Fig. 1-5
The vertical angular distribution of parallel and perpendicular polarization components of SR [1.28]. λ_c is the critical wavelength [eq. (2-20)], ψ is the vertical angle, and $\gamma=(1-\beta^2)^{-1/2}$ [eq. (2-16)].

1.9×10^{-8} sec. The SXE experiments reported here make no use of the time structure of the radiation.

The electron beam width in the NSLS ring, which determines the vertical source size and brightness is 0.12 mm The horizontal size is determined by the number of horizontal milliradians accepted by the beamline optics. In the UT SXE beamline, one to one optics are used in the beamline which would ideally produce an excitation spot of 0.12 mm x 3.0 mm on the sample. In practice, an excitation spot of about 0.5 mm x 3 mm is obtained.

Work at the synchrotron light source presents several problems. Access to the SR is through a front end containing vacuum and radiation shutters and under the control of storage ring staff. Access is not allowed if the beamline vacuum exceeds about 10^{-9} torr or if organic contaminants are present in the beamline. Thus work on high vapor pressure materials is not possible unless extensive differential pumping is provided. The front end components and general crowding also make the installation and manipulation of upstream optical components difficult and inconvenient. The beam current, and thus the SR intensity, is not constant, but decays slowly with a time constant of

the order of one or two hours, so that beam current must be monitored and appropriate correction should be made. Because of the very long optical lever arm, even very small shifts in the electron orbit result in shifts of the exciting light on the sample. Finally, the large amount of power in the broadband spectrum from the synchrotron source can heat mirrors and destroy components such as absorption filters if care is not taken in their design.

E. Scope of the Present Work

In Section II, we discuss the major theoretical aspects of the research presented here. In section II A,soft x-ray emission theory is first described using the one electron model. Many body effects are then introduced to interpret some special features of the SXE spectra. In II B, the characteristics of SR are described quantitatively [1.29]. In II C these results are combined with a first order expansion of the Fresnel equations to form a theoretical model adequate for the description of the grazing incidence optics used in the beamline. The quantitative description of beamline transmission properties was a major part of my

contribution to the experimental facilities. Finally, in II D, the major equations governing the design of Rowland circle spectrometers are summarized.

Sections III and IV are devoted to descriptions of the design, calibration and performance of the spectrometer and beamline respectively. In the final section the SXE spectra of dilute Al in Mg and LiAl alloys are reported. The SXE spectra of dilute Al in Mg alloys are discussed and compared with spectrum obtained using Auger spectroscopy. These results present new information on both the Al impurity spectra and the high energy satellite spectrum of Mg which results from radiative recombination to a doubly ionized 2p core level. The SXE spectra of LiAl (50% - 50%) alloy are compared with the PDOS for Li K emission and with the (s+d)-PDOS for Al $L_{2,3}$ emission calculated by Asada et al. [5.39].

II. THEORETICAL ASPECTS

A. Soft X-ray Emission from Solids

When electrons make transition from valence states to core states, the SXE spectral intensity is given by

$$I(\omega) = C\omega \sum_{f} |< \Psi_f | T | \Psi_i >|^2 \delta (\hbar\omega - E_f + E_i) \qquad (2\text{-}1)$$

where I is the number of photons radiated per second, the summation is over all final states with the energy $E_f = \hbar\omega + E_i$, C is a constant, and T is the operator which connects the electrons with the radiation field. T is given by

$$T = \sum_{j}^{N} \hat{n}\, \hat{p}_j \exp (i\, \hat{k}\cdot\hat{r}_j) \qquad (2\text{-}2)$$

where $\hat{n}$ is a unit vector for the polarization of the radiation field, $\hat{r}_j$ and $\hat{p}_j$ are the position and momentum operators for electron j, $\lambda = 2\pi/k$ is the wavelength of the radiation and N is the total number of valence electrons. Eq. (2-1) includes all electron-electron and electron-phonon interactions, since the Ψ_i represents N conduction electrons

plus a vacant hole while Ψ_f represents N-1 conduction electrons plus a filled core[2.1]. In the Hartree-Fock approximation, Eq. (2-1) is simplified to[2.2]

$$I(\omega) = C\omega \sum_k |\langle \psi_k \mid T_j \mid \psi_{core} \rangle|^2 \, \delta \, (\hbar\omega - E_k + E_{core}) \tag{2-3}$$

where ψ_{core} is the one electron core wavefunction, the sum is taken over all valence or conduction band wavefunctions with energy $E_k = \hbar\omega + E_{core}$, and $T_j = \hat{n}\,\hat{p}_j \exp(i\hat{k}\cdot\hat{r}_j)$.

Two general conclusions can be drawn from Eq. (2-3). First SXE spectra give valence band information localized only in a small region around the excited core ions, because the non-zero ψ_{core} is localized in a small region in the core of the emitting ion. Second, when the wavefunction describing the core vacancy has s-symmetry, the band information carried by $I(\omega)$ should have p-symmetry due to the dipole selection rule. In the same way, the transition of electrons to core levels with p-symmetry will carry information about band states with s- and d-symmetry. The latter is the case for the $L_{2,3}$ spectra of Al and Mg which will be discussed later in this dissertation.

The Dipole Approximation[2.2]. Expanding $\exp(i\hat{k}\cdot\hat{r}_j)$ in

Eqs. (2-2) and (2-3) in a power series,

$$\exp\,(i\hat{k}\cdot\hat{r}_j) = 1 + i\hat{k}\cdot\hat{r}_j + \frac{(i\hat{k}\cdot\hat{r}_j)^2}{2!} + \cdots \qquad (2\text{-}4)$$

For soft x-ray emmision, since the dimensions of the system, here determined by the $\hat{r}_j$ for the valence electrons, are much smaller than the wavelength $2\pi/k$, the exponent of Eq (2-4) is set equal to unity to obtain the dipole approximation. Then we can rewrite Eq. (20-1) in the form

$$I(\omega) \simeq C\omega \sum_f |\langle\Psi_f| \sum_j^N \hat{n}\,\hat{p}_j\,|\Psi_j\rangle|^2\,\delta(\hbar\omega - E_f + E_i)$$

$$= C\omega^3 \sum_f |\langle\Psi_f| \sum_j^N \hat{n}\,\hat{r}_j\,|\Psi_i\rangle|^2\,\delta(\hbar\omega - E_f + E_i) \qquad (2\text{-}5)$$

and Eq. (2-3) becomes

$$I(\omega) = C\omega^3 \sum_k |\langle\psi_k|\,\hat{r}_j\,|\psi_{core}\rangle|^2\,\delta(\hbar\omega - E_k + E_{core}) \qquad (2\text{-}6)$$

The Free Electron Model. In the free electron model, the potential energy is set equal to zero and there are no interactions between conduction electrons and the ion cores. Solving the Schrodinger equation and using the Pauli exclusion principle, we find the density of states in three dimensions to be[2.4]

$$N(E) = \frac{V}{2\pi^2} \left(\frac{2m}{h^2}\right)^{3/2} E^{1/2} \qquad (2\text{-}7)$$

which gives the number of states per unit energy interval. In the free electron model, ψ_k is proportional to $\exp(i\hat{k}\cdot\hat{r})$. If ψ_k and ψ_{core} are expanded as a series of spherical harmonics and substituted into Eq. (2-6), the transition probability can be written as[2.2]

$$I(\omega) \propto \omega^3 N(E) \left[f_{l+1} j_{l+1}^2 \left(\frac{ka}{2}\right) + f_{l-1} j_{l-1}^2 \left(\frac{ka}{2}\right)\right] \qquad (2\text{-}8)$$

where $N(E) \propto E^{1/2}$, a is the average atomic spacing, j_l are spherical Bessel functions with ℓ angular momentum, f_{l-1} and f_{l+1} are expansion coefficients.

When $\ell = 0$ as for s-states, the s-symmetry partial density of states (PDOS) will rise as $E^{1/2}$ above the band threshold, because $j_0(ka/2)$ is constant near the bottom of the band where $k = 0$ corresponds to $E = 0$. On the other hand, the p-like PDOS will rise as $E^{3/2}$ and the d-like density of states will rise as $E^{5/2}$ at energies just above the bottom of the band as is illustrated in Fig. 2-1, which shows PDOS calculated for free electron bands.

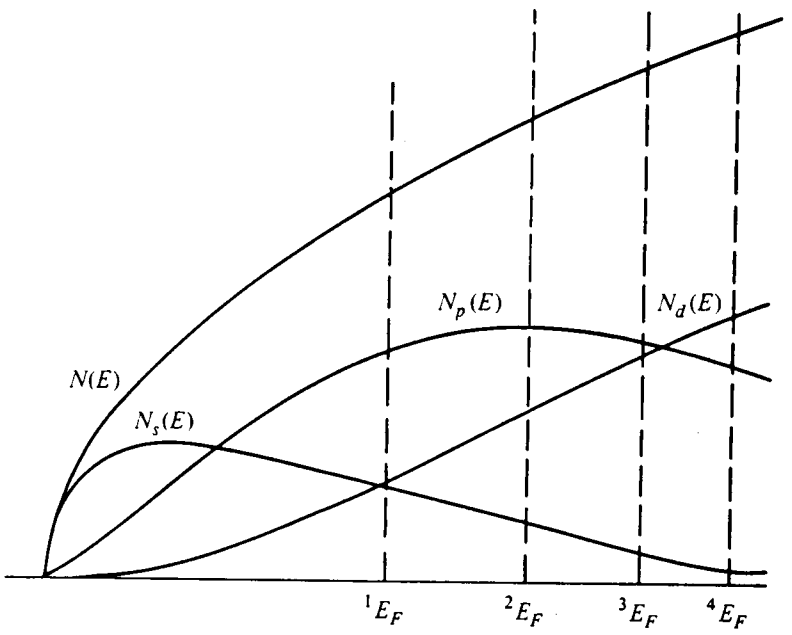

Fig.2-1
Partial density of states for s- p- and d- symmetry electrons calculated by free electron model [2.2].

The Nearly-free-electron Model. The density of states (DOS) within dE of E is given by

$$N(E)\,dE = \frac{v_c}{8\pi^3}\int d^3k \qquad (2\text{-}9)$$

where $\frac{8\pi^3}{v_c}$ is the volume of the Brillouin zone, the integral is over the volume of a shell in $\hat{k}$-space for which $E \leq E_k \leq E + dE$, $v_c = N/V$ is the volume of the unit cell of the real space, N is the number of particles and V is the crystal volume[2.5]. In $\hat{k}$-space, consider as a volume element the cylinder with base d^2k on the surface defined by E = constant and height $dk = dE/\nabla_k E$ perpendicular to the surface, so $d^3k = d^2k\,\frac{d\,E}{\nabla_k E}$; here

$$\nabla_k E = \left(\frac{\partial E}{\partial k_x}, \frac{\partial E}{\partial k_y}, \frac{\partial E}{\partial k_z} \right).$$

Then we can write Eq. (2-9) in the form

$$N(E)\,dE = \frac{2}{8\pi^3 N}\int \frac{d^2k}{\nabla_k E}\,dE, \qquad (2\text{-}10)$$

and the DOS is given by

$$N(E) = \frac{1}{4\pi^3 N}\int \frac{d^2k}{\nabla_k E}. \qquad (2\text{-}11)$$

Here the electrons of opposite spin have been summed to give a factor of two, and the integral is taken over the surface

with constant E. Eq. (2-6) can now be written in the form

$$I(\omega) \propto \omega^3 \int \frac{d^2k}{\nabla_k E} |\langle \psi_k | \hat{n}_j | \psi_{core} \rangle|^2 \qquad (2\text{-}12)$$

where the integral is taken over the constant energy surface with $E_k = h\omega + E_{core}$ in $\hat{k}$-space. If the matrix element were independant of $\hat{k}$, Eq. (2-12) would become

$$I(\omega) \propto \omega^3 |\langle \psi_k | \hat{r}_j | \psi_{core} \rangle|^2 \, N(E) \qquad (2\text{-}13)$$

In this approximation, the SXE spectrum is simply related to the features of the one electron PDOS calculated from the wavefunctions of band theory. Several such interpretations have been made of the Mg and Al $L_{2,3}$ emission spectra [2.3, 2.6].

In the next four sections, we will briefly consider a series of many body phenomena which effect the SXE spectra. We will discuss primarily the simple metals, because most theoretical analyses of SXE spectra using many body theory have been restricted to simple metals , and because Mg and Al can, for many purposes, be described as nearly-free-electron simple metals.

In Fig. 2-2 several prominant features that are relevant to the discussion are identified on the primary Mg $L_{2,3}$ spectrum

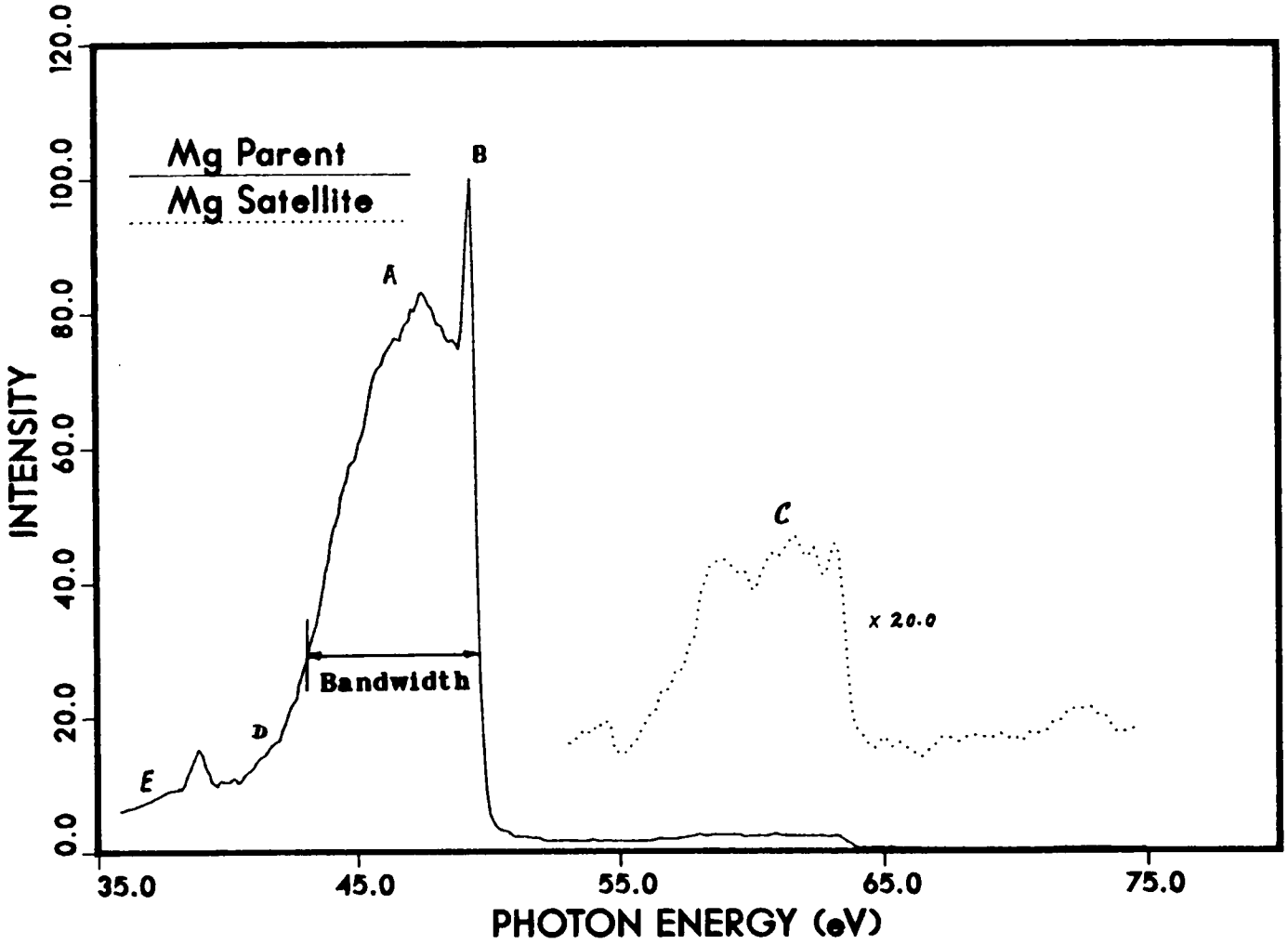

Fig.2-2
Typical SXE spectrum for simple metal Mg. Features designated by letter are A). the density of states; B). the MND edge singularity; C). the double ionization satellite; D). the Auger tail; and E).the plasmon satellite.

and on the associated double ionization satellite. They are: A - a density of states feature that is consistent with the application of the final state rule; B - the MND edge singularity; C - the double ionization satellite; D - the Auger tail (Auger assisted emission); and E - the plasmon satellite.

The Final State Rule. We note that in the one electron approximation, the ψ_{core} in Eq. (2-12) is simply an atomic core function. But in order to obtain ψ_k, one must determine what potential energy should be used in the Schrodinger equation. The possible choices are: (a) the ground state potential corresponding to a final state with a filled core hole, and (b) the potential in the presence of the core hold with screening valence electrons around it. The rather surprising result embodied in the Final State Rule (FSR) is that the proper choice is (a). This conclusion comes from direct comparisons of many-body calculations based on Eq. (2-5) and one-electron calculations based on Eq. (2-6) using ground state and screened core hole potentials [2.7,2.8]. As we noted in the introduction, this conclusion is consistant with the large body of experimental data that has been

interpreted with DOS's derived from ground state band calculations. The FSR also suggests that there may be similarities between the $L_{2,3}$ spectrum for impurity Al imbedded in a Mg host, and the double ionization satellite of pure Mg, since both have an extra core charge in the final state of the system [2.9].

The MND Edge Singularity. The $L_{2,3}$ spectra of simple metals such as Na, K, Al and Mg are observed to have sharp peaks at their high energy edges. Using many body theory, Mahan, Nozieres, and deDominicis (MND) derived an expression for the shape of the edge in the form of a power law [2.10, 2.11, 2.12, 2.13]

$$I(h\omega) \propto [\frac{\xi}{h\omega - E_F}]^{\alpha} \theta(\hbar\omega - E_F) \qquad (2\text{-}14)$$

For $L_{2,3}$ spectra,

$$\alpha = \alpha_0 = \frac{2\delta_0}{\pi} - 2 \sum_{j}^{\infty} (2j + 1) (\frac{\delta_j}{\pi})^2 > 0, \qquad (2\text{-}15a)$$

and for K spectra,

$$\alpha = \alpha_1 = \frac{2\delta_1}{\pi} - 2 \sum_{j}^{\infty} (2j + 1) (\frac{\delta_j}{\pi})^2 < 0, \qquad (2\text{-}15b)$$

where ξ is a constant with the dimension of energy, E_F is

the threshold energy, θ is the usual step function, and δ_ℓ (ℓ = 0,1) are the Friedel phase shifts. For $L_{2,3}$ spectra, since $\alpha > 0$, the edge is enhanced and shows a sharp spike. The feature B in Fig. 2-2 may be attributed in part to this MND anomaly, although in the case of Mg, the interpretation of the threshold spike is complicated by the presence of a threshold peak in the ordinary density of states.[2.14]. For K spectra, for which $\alpha < 0$, the edge should be rounded off. The rounding of K spectra by many body effects has not been unambiguously confirmed. In the case of Li, the strong rounding of the K edge is thought to result primarily from lattice relaxation around the core hole (a phonon-core hole interaction) rather than from the MND many-body rounding [2.15].

The Double-ionization Satellite. Two electrons may be removed from the L shell in the core. When one of the holes is filled by a radiative transition, a weak satellite spectrum is produced on the high energy side of the primary L spectrum. Using the notation of LS coupling, the doubly ionized core can form states of $^3P_{2,1,0}$, $^1D_2$, and $^1S_0$ symmetry. The $^1S_0$ state is most tightly bound to the core

and the P states lie closest to the valence states. If all the states were excited equally, and all were radiatively de-excited with equal probability, the intensities for the resulting satellites would be in the ratio of the degeneracies P : D : S = 9 : 5 : 1 [2.16]. In fact, only the $^3P_2$ spectrum is generally observed, as was recently demonstrated in an analysis of data for Mg, Al and Na[2.17]. Previous workers had suggested that the observed structure of satellite resulted from overlapping P and D spectra [2.18]. It is believed that spectra from the more tightly bound $^1S_0$ and $^1D_2$ states are not observed because these states are rapidly filled by non-radiative transitions before radiative transitions can occur with significant probability. In our data from Mg, we have identified a very weak spectral feature that may result from radiative transitions to these deeper levels. Consequently, we present here in Table 2-1 the energy seperations between the $^3P_2$ state and states of other symmetry calculated for the free ions of Mg and Al [2.19].

The Auger Tail and Plasmon Satellite. The extended low energy tail of the SXE spectra from metals is attributed to Auger processes that accompany the radiative transitions.

Table 2-1
Energy separations between $^3P_2$ and $^3P_{1,0}$, $^1D_2$, $^1S_0$ states for free ions of Al and Mg [2.19].

	$^3P_1$	$^3P_0$	$^1D_2$	$^1S_0$
Al	0.27	0.54	4.5	11.2
Mg	0.14	0.18	3.87	9.64

To our knowledge, a satisfactory quantitative calculation of this effect has not been made for Al and Mg, though the effect has been discussed by several workers [2.19,2.20]. Another contribution to the low energy tail is produced by a plasmon satellite produced when a plasmon with energy is excited before emission occurs. Rooke first reported the observation of plasmon satellites on the low energy edges of the Al and Mg spectra in agreement with earlier predictions [2.22,2.23]. Fig. 2-3 gives the intensity ratio between the satellite band and main band as a function of r_s, an electron density parameter. J_i (i = 1,0) is defined as

$$J_i = \int_0^\infty I_i(\omega)\, d\omega$$

where $I_i(\omega)$ is the SXE intensity for the satellite (i = 1) and parent (i = 0) spectra, ω is the emission frequency. We note that for the simple metals, the $L_{2,3}$ spectra have weaker plasmon satellites than the K spectra.

B. Synchrotron Radiation

Green has summarized the characteristics of SR in parametic form with many useful tables and graphs [2.24].

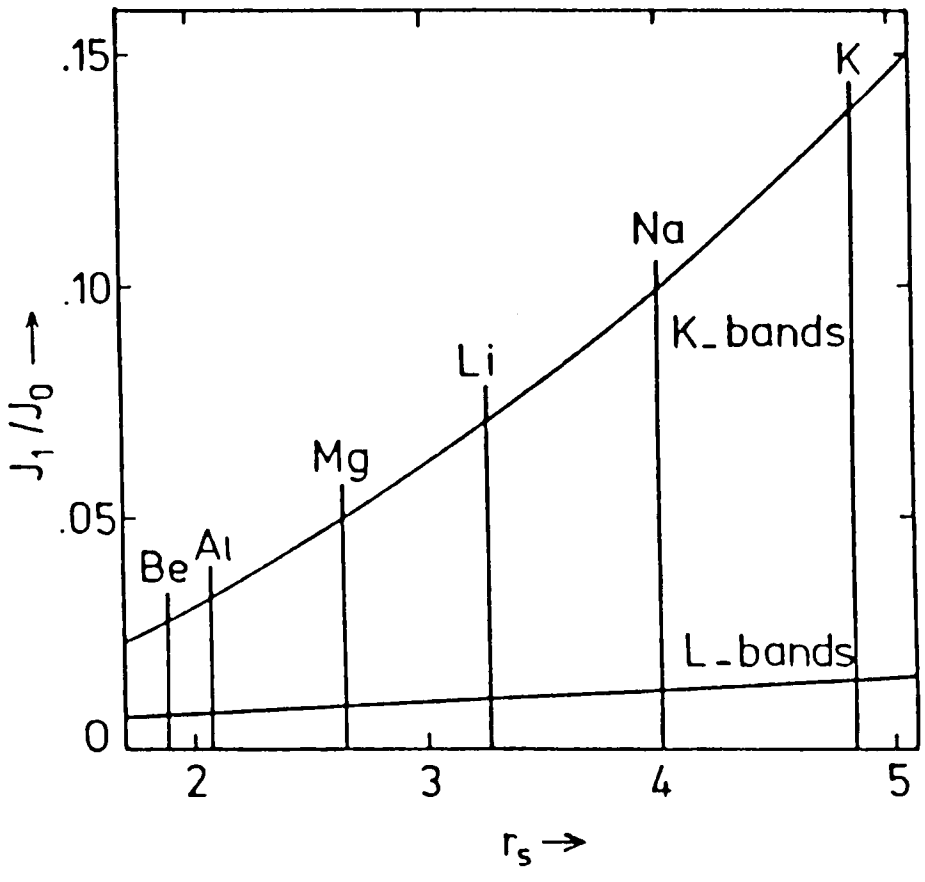

Fig.2-3
Intensity ratio, J_0 / J, between satellite band and main band for light metals as a function of r_s, the electron density parameter [2.23].

His work greatly simplies the process of calculating photon fluxes, including angular distributions, polarization, and total radiation intensities. A description of the general characteristics of SR can be found elsewhere[2.24, 2.25,2.26].

Basic Equations. The total energy of an electron moving with velocity v is

$$E = \frac{m_0}{\sqrt{1 - \beta^2}} = \gamma\, m_0 c^2,$$

with $\beta = v / c$, where c is the velocity of light, and m_0 is the electron rest mass. Since $m_0 = 0.511$ MeV,

$$\gamma = 1957\, E, \qquad (2\text{-}16)$$

with E the electron beam energy in GeV.

When the electron is traveling at relativistic velocity with a large value of γ, the kinetic energy K is approximately equal to E

$$K = E - m_0 c^2 \cong \gamma\, m_0 c^2,$$

and

$$\beta = \sqrt{1 - 1/\gamma^2} \cong 1.$$

The total instantaneous power radiated in a circlar path in a magnetic field B is

$$P = \frac{2}{3} \frac{e^2 c \beta^4}{R^2} \gamma^4,$$

where, R is the radius of curvature

$$R = \frac{m_0 \beta \gamma c^2}{eB}.$$

The energy radiated per revolution by an electron is

$$\delta E = \frac{2\pi R}{c\beta} P = \frac{4\pi}{3} \frac{e^2 \beta^3 \gamma^4}{R}. \qquad (2\text{-}17)$$

Schwinger's Equations. In order to obtain a detailed description of SR and its dependence on the ring parameters, Schwinger derived an expression for radiative power per unit angular frequency of the radiation by an electron

$$P_0(\omega,t) = \frac{3^{3/2}}{4\pi} \frac{e^2 \gamma^4}{R} \frac{\omega_0 \omega}{\omega_c^2} \int_{\omega/\omega_0}^{\infty} K_{5/3}(\eta)\, d\eta, \qquad (2\text{-}18)$$

with $\omega_0 = c/R$ and $\omega_c = \frac{3}{2} \omega_0 \gamma^3$. The K ($\eta$) is the modified Bessel Function of the second kind.

Using

$$\omega = 2\pi\nu = 2\pi \frac{c}{\lambda},$$

$$\omega_c = 2\pi \frac{c}{\lambda_c} ,$$

$$\frac{\omega}{\omega_c} = y ,$$

$$k = \Delta\lambda/\lambda,$$

$$P'(\lambda,t) = \frac{\text{radiation}}{\text{time}\cdot\text{wavelength}\cdot\text{ an electron}} \ (\text{erg}\cdot\text{sec}^{-1}\cdot\text{Å}^{-1})$$

$$= \frac{\omega}{\lambda} P_0(\omega,t)$$

$$= \frac{3^{5/2}}{16\pi^2} \frac{e^2 c\gamma^7}{R^3} \left(\frac{\lambda_c}{\lambda}\right)^3 \int_y^\infty K_{5/3}(\eta)\, d\eta . \qquad (2\text{-}19a)$$

$$N_k'(\lambda,t) = \frac{\text{emitted photons}}{\text{time}\cdot\text{ an electron}} \ (\text{sec}^{-1})$$

$$= \frac{k\lambda}{h\nu} P'(\lambda,t)$$

$$= 3^{1/2} \frac{ke^2\gamma}{hR} \left(\frac{\lambda_c}{\lambda}\right) \int_y^\infty K_{5/3}(\eta)\, d\eta \quad \text{from } \lambda \text{ to } \lambda+d\lambda, \qquad (2\text{-}19b)$$

where the critical wavelength λ_c can be written as

$$\lambda_c = \frac{4\pi R}{3\gamma^3}. \qquad (2\text{-}20)$$

Note that the number of electrons, n, is related to ring current by

$$n = \frac{2\pi R}{e} \left(\frac{I}{10}\right). \qquad (2\text{-}21)$$

with I the ring current in amps. Referring to Fig. 2-4, the radiated power (erg·sec^{-1}) into all vertical angles ψ per unit of ring current I (A), per horizontal angle θ (radian) and per unit λ(Å) becomes

$$P(\lambda,t) = \frac{n}{2\pi} P'(\lambda,t)$$

$$= \frac{3^{5/2}}{160\pi^2} \frac{ecI\gamma^7}{R^2} \left(\frac{\lambda_c}{\lambda}\right)^3 \int_y^\infty K_{5/3}(\eta)\, d\eta. \qquad (2\text{-}22a)$$

The number of photon emitted into all vertical angles ψ per ring current I (amp), per θ (radian), per sec from λ to $\lambda+\Delta\lambda$ is

$$N_k(\lambda,t) = \frac{n}{2\pi} N_k'(\lambda,t)$$

$$= \frac{3^{1/2}}{10} \frac{keI\gamma}{h} \left(\frac{\lambda_c}{\lambda}\right) \int_y^\infty K_{5/3}(\eta)\, d\eta. \qquad (2\text{-}22b)$$

Polarization of SR and Angular Distribution. A plane harmonic wave propagated along the z-direction can be written as [2.27]

$$\mathbf{E} = \mathbf{E}_0 \exp[i(\omega t - kz)],$$

$$\mathbf{H} = \mathbf{H}_0 \exp[i(\omega t - kz)], \qquad (2\text{-}23)$$

where $\mathbf{E}_0$, $\mathbf{H}_0$ are constant vectors and k is a wave vector.

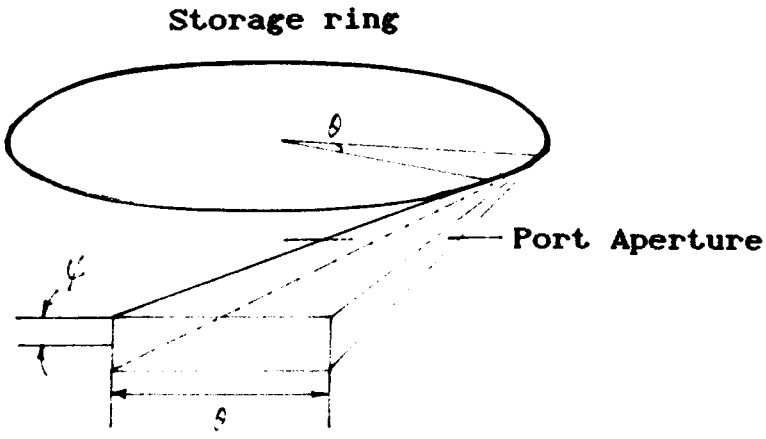

Fig.2-4
Diagram of vertical and horizontal divergence of SR for the beam line.

Putting eq.(2-23) into the Maxwell eq's, it may be shown that $\mathbf{E} \perp \mathbf{H}$, $\mathbf{E} \perp \hat{k}$, $\mathbf{H} \perp \hat{k}$, where $\hat{k}$ is along z-direction. The direction of $\mathbf{E}$ is defined as the polarization direction. Now consider the general harmonic wave propagated along the z-direction.

$$\mathbf{E} = E_x \hat{i} + E_y \hat{j},$$

$$E_x = A \exp [i (\omega t - kz + \delta_1)]$$

$$= A \exp (i\omega t'),$$

$$E_y = B \exp [i (\omega t - kz + \delta_2)]$$

$$= B \exp [i (\omega t' - \delta)],$$

$$\delta = \delta_1 - \delta_2, \qquad (2\text{-}24)$$

with δ the phase difference, and A, B the amplitudes of E_x, E_y respectively. We can obtain

$$\left(\frac{E_x}{A}\right)^2 + \left(\frac{E_y}{B}\right)^2 - 2\cos\delta \left(\frac{E_x E_y}{A B}\right) = \sin^2\delta. \qquad (2\text{-}25)$$

Table 2-2 from eq.(2-24) has been constructed to show all different polarized conditions. The definition of polarization $\mathcal{P}$ is

$$\mathcal{P} = \frac{I_{\parallel} - I_{\perp}}{I_{\parallel} + I_{\perp}} \qquad (2\text{-}26)$$

Table 2-2
Different polarization conditions for general harmonic wave.

	$\delta = 0$	$\delta = 2/\pi$	$\delta \neq 2/\pi$
$A = B$	$E_x = E_y$ Linearly	$E_x^2 + E_y^2 = A^2$ Circularly	(oblique) Elliptically
$A \neq B$	$BE_x = AE_y$ Linearly	$(E_x / A)^2 + (E_y / B)^2 = 1$ (normal) Elliptically	

where, $I_{\parallel}$, $I_{\perp}$ are intensity components of the electric vector parallel and perpendicular to the electron orbital plane respectively.

The general character of the polarization of SR is the predominance of the parallel component of the electric vector. Sokolov and Ternov have shown that the ratios of parallel and perpendicular components to the total intensity at relativistic energy are[2.24]

$$\frac{I_{\parallel}}{I_{\parallel} + I_{\perp}} = \frac{7}{8} ,$$

and

$$\frac{I_{\perp}}{I_{\parallel} + I_{\perp}} = \frac{1}{8} ,$$

over all angles and all wavelengths, so that polarization is

$$P = \frac{7}{8} - \frac{1}{8} = 75\%.$$

At the azimuth angle $\psi = 0$, i.e. in the electron orbital plane, the SR is 100% polarized with $P_{\perp}(\lambda, 0, t) = 0$, which will be proved below.

The explicit dependence of power radiated by traveling electrons in the ring depends on both azimuth angle ψ and the polarization. Green has defined the functions

$$F_{\parallel}\left(\frac{\lambda_c}{2\lambda}, \psi\right) = (1 + \gamma^2\psi^2)^2 \, K^2_{2/3}\left[\frac{\lambda_c}{2\lambda}(1 + \gamma^2\psi^2)^{3/2}\right], \quad (2\text{-}27a)$$

$$F_{\perp}(\frac{\lambda_c}{2\lambda},\ \psi\ ) = \gamma^2\psi^2(1 + \gamma^2\psi^2)\ K^2_{1/3}[\frac{\lambda_c}{2\lambda}(1 + \gamma^2\psi^2)^{3/2}], \quad (2\text{-}27b)$$

so that eqs (2-22a,2-22b) are changed into

$$P_{\perp,\parallel}(\lambda,\ \psi,\ t) = \frac{27}{320\pi^3}\ \frac{ecI\gamma^8}{R^2}\ (\frac{\lambda_c}{\lambda})^4\ F_{\perp,\parallel}, \qquad (2\text{-}28a)$$

$$N_{k\ \perp,\parallel}(\lambda,\ \psi,\ t) = \frac{3keI\gamma^2}{20\pi h}\ (\frac{\lambda_c}{\lambda})^2\ F_{\perp,\parallel}, \qquad (2\text{-}28b)$$

for radiated power and photons per sec, per amper, per θ and ψ (radian). The polarization is given by

$$\mathfrak{P}(\lambda,\ \psi) = \frac{P_{\parallel}(\lambda,\ \psi) - P_{\perp}(\lambda,\ \psi)}{P_{\parallel}(\lambda,\ \psi) + P_{\perp}(\lambda,\ \psi)} = \frac{F_{\parallel} - F_{\perp}}{F_{\parallel} + F_{\perp}}. \qquad (2\text{-}29)$$

From eqs. (2-27a,b), (2-28a,b) and table 2-2, we note that the parallel and perpendicular components are always out of phase; when $\psi = 0$, $P_{\perp}(\lambda,\ \psi,\ t) = 0$, $\mathfrak{P} = 100\%$, and the radiation is linearly polarized and parallel to the orbital plane. Out of the plane it is in general elliptically polarized, and the axes of ellipse are $\parallel$ and $\perp$ to the orbital plane.

Summary.[2.24] Substituting

$e = 4.803 \times 10^{-10}$ esu,

$c = 2.9979 \times 10^{10}$ cm/sec,

$h = 6.6256 \times 10^{-27}$ erg.sec,

$1eV = 1.6021 \times 10^{-12}$ erg,

$1A = 10^{-8}$ cm,

$k = \Delta\lambda / \lambda$, $y = \lambda_c / \lambda$,

into eqs.(2-17), (2-20), (2-21), (2-22b),and (2-28b), these equations become

$$\gamma = 1957\ E \qquad \text{(with E in GeV)}, \qquad (2\text{-}30)$$

$$\delta E = 88.47\ E^4/R \qquad \text{(keV per turn per } e^-), \qquad (2\text{-}31)$$

$$\lambda_c = 5.59\ R/E^3 \qquad (\text{Å with R in meters}), \qquad (2\text{-}32)$$

$$n = 1.308 \times 10^{11}\ RI \qquad \text{(number of electrons with I in amps)}. \qquad (2\text{-}33)$$

$$N_k(\lambda) = \frac{\text{photons}}{\text{sec}\cdot\text{mÅ}\cdot\theta\,(\text{mrad})}$$

$$= k\ \gamma\ F_1(\lambda_c/\lambda) \qquad \text{over all } \psi \text{ from } \lambda \text{ to } \lambda+\Delta\lambda. \qquad (2\text{-}34)$$

$$N_k(\lambda, 0) = \frac{\text{photons}}{\text{sec}\cdot\text{mÅ}\cdot\theta\,(\text{mrad})\cdot\psi(\text{mrad})}$$

$$= k\ \gamma\ F_4(\lambda_c/\lambda, 0) \qquad \text{at } \psi = 0 \text{ from } \lambda \text{ to } \lambda+\Delta\lambda. \qquad (2\text{-}35)$$

The radiation distribution can be calculated from

$$P(\lambda) = \frac{\text{ergs}}{\text{sec}\cdot\text{mÅ}\cdot\theta\,(\text{mrad})}$$

$$= \frac{hc}{\lambda} N_k(\lambda) \qquad \text{over all } \psi \text{ from } \lambda \text{ to } \lambda+\Delta\lambda. \tag{2-36}$$

$$P(\lambda, 0) = \frac{\text{ergs}}{\text{sec}\cdot\text{mA}\cdot\theta(\text{mrad})\cdot\psi(\text{mrad})}$$

$$= \frac{hc}{\lambda} N_k(\lambda, 0) \qquad \text{at } \psi = 0 \text{ from } \lambda \text{ to } \lambda+\Delta\lambda. \tag{2-37}$$

In beam line design when mirrors with different grazing angles and coating materials are introduced in beam line, it is desirable to have expressions for the flux (radiation) distribution along different polarization directions and summed over all ψ. Then the dependence of mirror reflectance on the polarization of incidence radiation can be considered in flux calculation. This can be accomplished by combining eq. (2-34) or (2-36) with the polarization equation and integrating over all ψ. Rewriting (2-29) and integrating each over ψ, we have

$$\mathcal{P} = \frac{\int_{-\infty}^{+\infty} [P_{\parallel}(\lambda, \psi) - P_{\perp}(\lambda, \psi)]\, d\psi}{\int_{-\infty}^{+\infty} [P_{\parallel}(\lambda, \psi) + P_{\perp}(\lambda, \psi)]\, d\psi}$$

$$= \frac{P_{\parallel}(\lambda) - P_{\perp}(\lambda)}{P_{\parallel}(\lambda) + P_{\perp}(\lambda)}$$

$$= \eta_{\parallel}(\lambda_c/\lambda) - \eta_{\perp}(\lambda_c/\lambda), \tag{2-38}$$

where $$\eta_{\parallel}(\lambda_c/\lambda) = \frac{P_{\parallel}(\lambda)}{P_{\parallel}(\lambda) + P_{\perp}(\lambda)},$$

$$\eta_{\perp}(\lambda_c/\lambda) = \frac{P_{\perp}(\lambda)}{P_{\parallel}(\lambda) + P_{\perp}(\lambda)}. \qquad (2\text{-}39)$$

The curves of $F_1(\lambda_c/\lambda)$, $F_4(\lambda_c/\lambda,0)$, $\eta_{\parallel}(\lambda_c/\lambda)$ and $\eta_{\perp}(\lambda_c/\lambda)$ are drawn in Figs. 2-5, 2-6, 2-7. For use in calculations, these curves are fitted by a series of polynomials to increase the speed of calculations.

C. Photon Flux Distribution through Optical Elements

In SXE spectroscopy excited by synchrotron radiation we are concerned primarily with the following quantities and distributions related to the ring parameters:

1) the flux distribution from the synchrotron source integrated over all ψ ;

2) the flux distribution over all ψ after light has passed through the mirrors and filters of the beam line system;

3) the change of polarization over all ψ before and after the beam line compounds;

4) the radiation distribution, over all ψ, incident on the

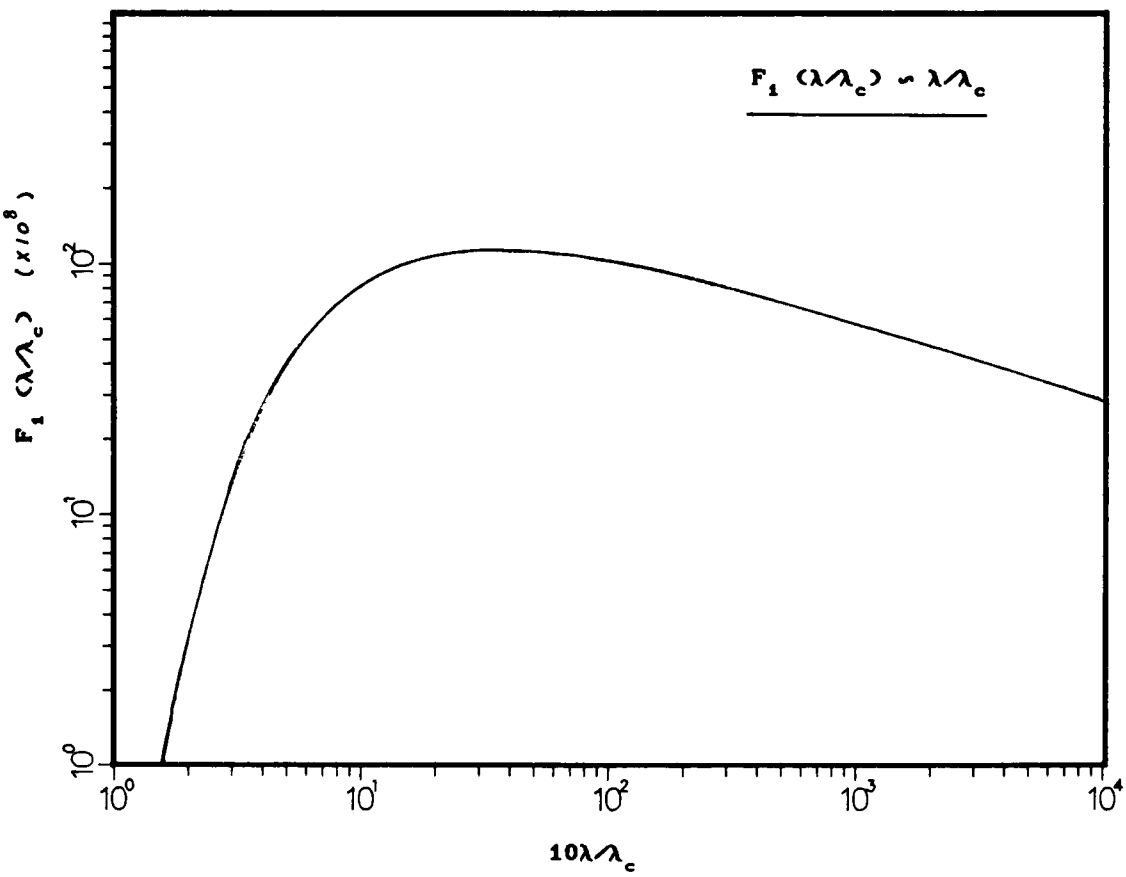

Fig.2-5
Flux distribution function $F_1(\lambda_c/\lambda)$ [2.24]. λ_c is the critical wavelength [see eq. (2-20)].

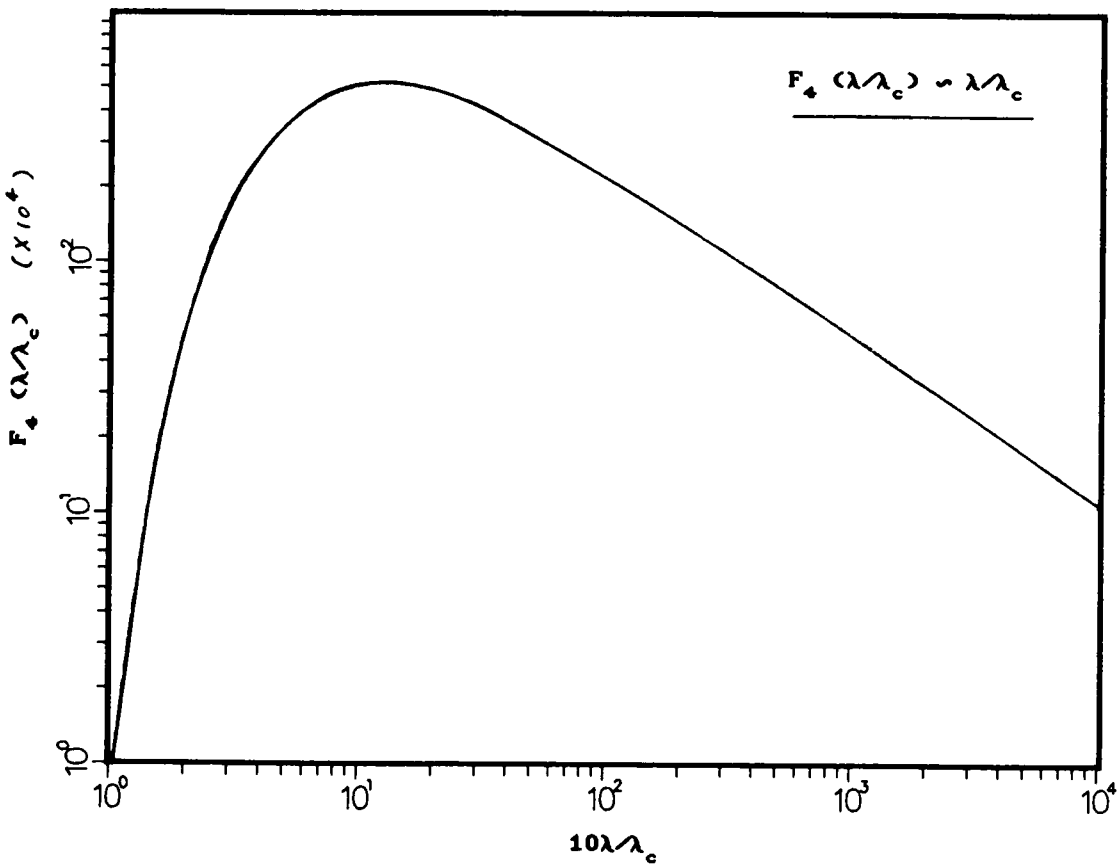

Fig.2-6
Flux distribution function $F_4(\lambda_c/\lambda)$ [2.24]. λ_c is the critical wavelength [see eq. (2-20)].

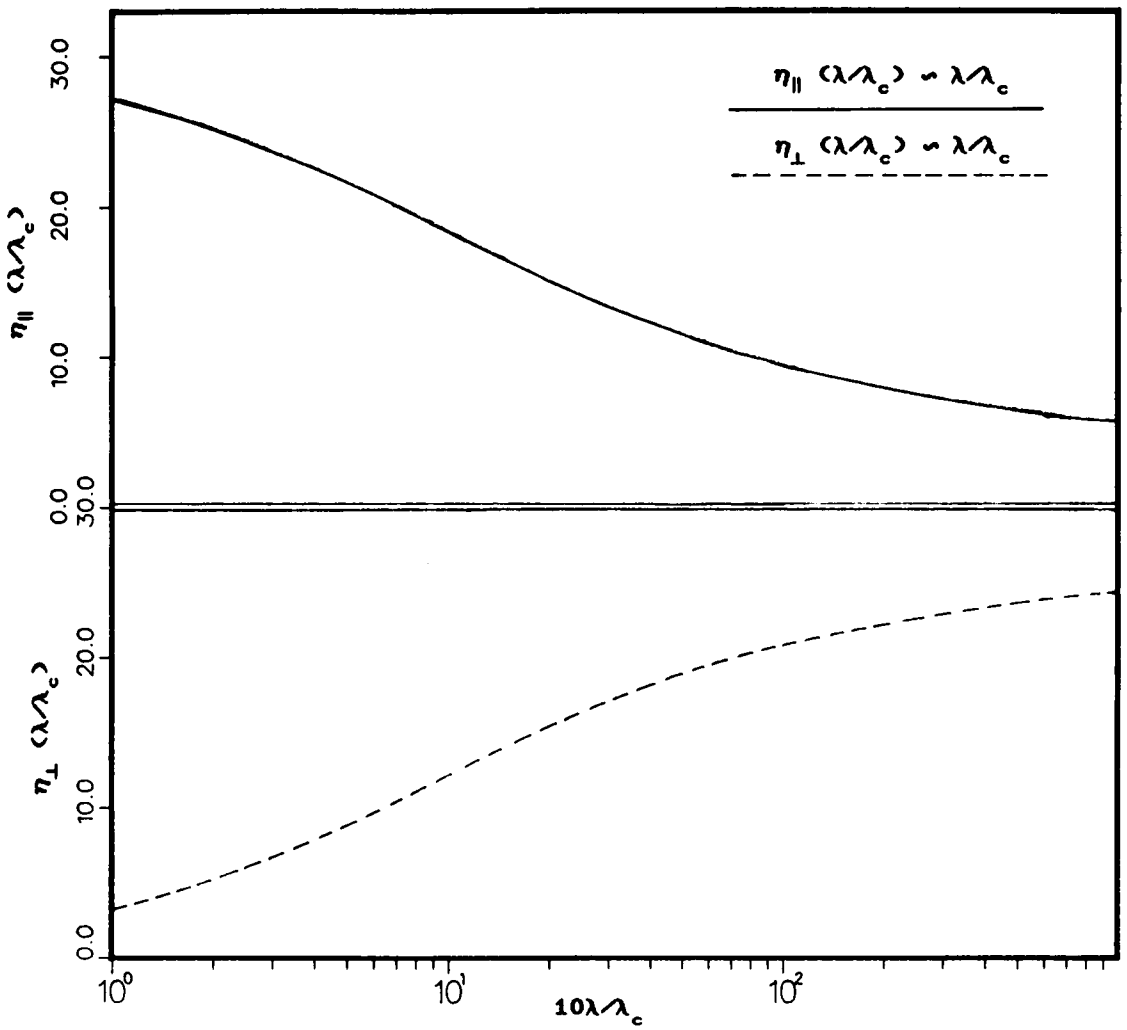

Fig.2-7
Ratio curves of parallel and perpendicular components to total radiation over all vertical divergence from the SR source [2.24].

optical elements and the sample;

5) the total power on the optical elements and the sample.

Consider a homogeneous metal thin film. Define a complex refractive index $\hat{n}$ such that

$$\hat{n} = (n + ik), \tag{2-40}$$

where n is the refractive index and k is the extinction coefficient. Notice that n and k are both dependent on wavelength λ. The absorption coefficient is defined as

$$\alpha = \frac{1}{I} \frac{dI}{dx}, \tag{2-41}$$

where I is the intensity,and x is the thickness of the film. Substituting the square of the wave amplitude of electrical vector as I into (2-41), it can be shown that[2.28]

$$\alpha = \frac{4\pi k}{\lambda}. \tag{2-42}$$

Then the radiation intensity and flux distribution, $P_f(\lambda)$, $N_f(\lambda)$, after a film are

$$P_f(\lambda) = P(\lambda) \exp\left(\frac{-4\pi kx}{\lambda} \right), \tag{2-43a}$$

$$N_f(\lambda) = N_k(\lambda) \exp\left(\frac{-4\pi kx}{\lambda} \right). \tag{2-43b}$$

The presence of a mirror in the radiation path has a different effect on the radiation which depends on whether the radiation is parallel or perpendicular to the incident plane. Define p- as the subscript designating a component parallel to the incident plane, and s- the subscript for the perpendicular component. The standard Fresnel equations are [2.29]

$$r_p(\beta) = \frac{\hat{n}^2 \sin\beta - \sqrt{\hat{n}^2 - \cos^2\beta}}{\hat{n}^2 \sin\beta + \sqrt{\hat{n}^2 - \cos^2\beta}}, \qquad (2\text{-}44a)$$

$$r_s(\beta) = \frac{\sin\beta - \sqrt{\hat{n}^2 - \cos^2\beta}}{\sin\beta + \sqrt{\hat{n}^2 - \cos^2\beta}}, \qquad (2\text{-}44b)$$

where β is the grazing angle, r_p, r_s are amplitude reflectances for parallel and perpendicular components respectively. Here light is incident from vacuum onto a medium with complex refractive index $\hat{n}$ as shown in Fig. 2-8. Define the intensity reflectances as Rs, Rp, then [2.30]

$$R_s = r_s^* r_s$$

$$= |r_s(0)|^2 + \beta \frac{d\,|r_s(0)|^2}{d\,\beta} + \cdots, \qquad (2\text{-}45a)$$

$$R_p = r_p^* r_p$$

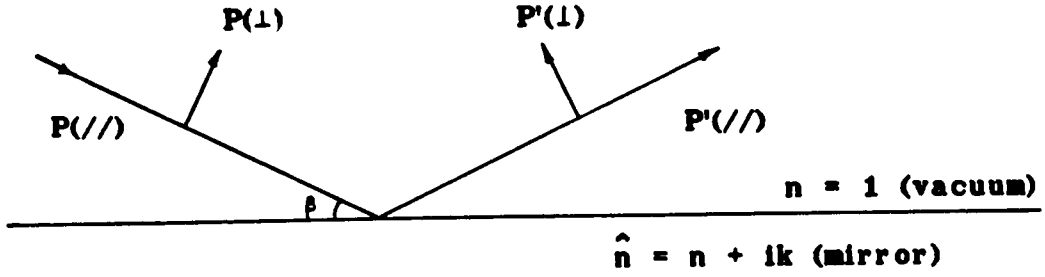

Fig.2-8
Diagram of polarization components at interface between vacuum and medium.

$$= |r_p(0)|^2 + \beta \frac{d\,|r_p(0)|^2}{d\,\beta} + \cdots \qquad (2\text{-}45b)$$

For small grazing angle β the reflectance eqs (2-45a,b) become

$$R_p \cong 1 - 4\,\beta\,\mathrm{Re}\left(\frac{\hat{n}^2}{\sqrt{\hat{n}^2 - 1}}\right), \qquad (2\text{-}46a)$$

$$R_s \cong 1 - 4\,\beta\,\mathrm{Re}\left(\frac{\hat{n}^2}{\sqrt{\hat{n}^2 - 1}}\right). \qquad (2\text{-}46b)$$

Notice here that R_p and R_s are functions of wavelength λ, because of the dependence of n and k on λ.

In most solid state experiments, which utilize SR as a light source, the incident planes of grazing incidence mirrors or gratings are perpendicular to the ring orbital plane. Since R_s is greater than R_p, this arrangement will provide the highest intensity since SR is strongly polarized in the direction parallel to the orbital plane [2.25]. In this case, using (2-36), (2-38) and (2-39), the reflected radiation and flux distributions, $P_m(\lambda)$ and $N_m(\lambda)$ after a mirror with grazing angle β become

$$P_m(\lambda) = P_{\parallel}\,R_s + P_{\perp}\,R_p$$

$$= P(\lambda)\,[\eta_{\parallel} R_s + \eta_{\perp} R_p], \qquad (2\text{-}47a)$$

$$N_m(\lambda) = N_k(\lambda)\,[\eta_{\parallel} R_s + \eta_{\perp} R_p]. \qquad (2\text{-}47b)$$

We can also obtain the polarization, $\mathfrak{p}_m(\lambda)$, after a mirror from (2-29), (2-38), (2-39), (2-47a)

$$\mathfrak{p}_m = \frac{\eta_{\parallel} R_s - \eta_{\perp} R_p}{\eta_{\parallel} R_s + \eta_{\perp} R_p}. \qquad (2\text{-}48)$$

The total power incident on a particular optical element or sample per unit of beam current (mA), per θ (mrad) over all ψ is just the integral of the radiation distribution over all wavelengths incident onto this element.

D. The Rowland Circle [2.31]

The Rowland circle geometry used in the design of off axis monochromators is illustrated by Fig. 2-9, where a concave grating with radius of curvature R is mounted tangent to a circle having diameter R, with the normal line to the grating center passing through the center of the circle, and the input slit S located on the circle. The dispersed

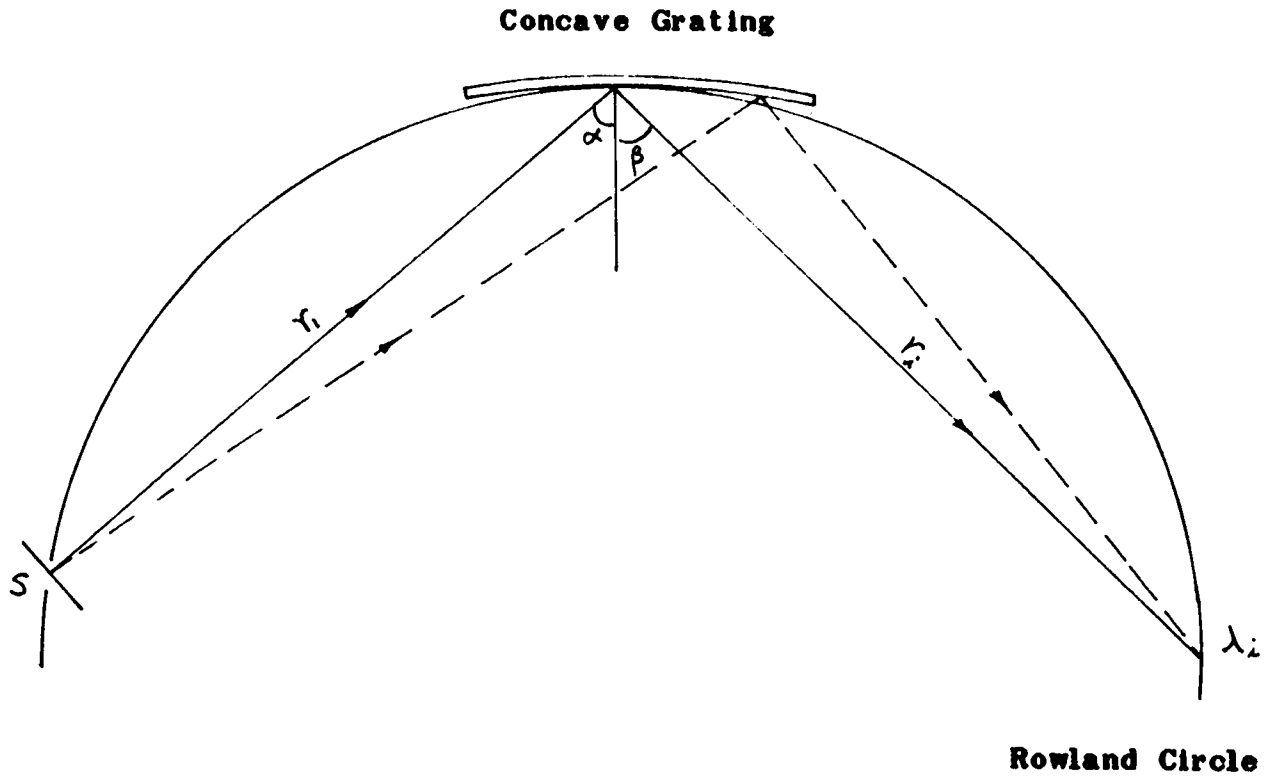

Fig.2-9
Diagram of the Rowland circle geometry.

image of S will form a spectrum that is in focus along this circle. The basic equations are

$$\cos \alpha = r_i / R, \qquad (2\text{-}49)$$

$$\cos \beta_i = r_i / R, \qquad (2\text{-}50)$$

$$m \lambda_i = d (\sin \alpha - \sin \beta_i), \qquad (2\text{-}51)$$

where m is the spectral order, α is the incident angle, β_i is the exit angle, and 1/d is the number of grating lines per unit length. We may rewite eq. (2-51) as

$$m \lambda_i N = 10^7 (\sin \alpha - \sin \beta_i), \qquad (2\text{-}52)$$

where λ_i is measured in Å, and N is the number of grating line per mm. Differentiating λ_i with respect to β_i in eq. (2-52) and noting that

$$d \ell = - R \, d\beta_i ,$$

where $d\ell$ is the dispersion along the circle due to the change of wavelength, one obtains the dispersion relation

$$\frac{d\lambda_i}{d\ell} = \frac{\cos\beta_i}{m R N} 10^4 \quad (\text{Å} / \text{mm}), \qquad (2\text{-}53)$$

where R is measured in meters.

For a diffraction grating, the resolving power is defined

as the ratio of the wavelength (λ) to the minimum wavelength interval ($\Delta\lambda$) which the spectrometer can resolve. For a plane grating illuminated by coherant light over its entire surface, the resolving power is given by

$$\lambda / \Delta\lambda = m N_T , \qquad (2\text{-}54)$$

Where N_T is the total number of lines in the grating. Since $\lambda = k / E$, $\Delta\lambda = -\Delta E / E$, eq. (2-54) becomes

$$E / \Delta E = m N_T , \qquad (2\text{-}55)$$

where E is photon energy and k is constant.

For grazing incidence design, in which the wavefronts do not maintain coherence over the grating surface, N_T may be replaced by an $N_{eff} << N_T$ that varies with the specific design. Generally coherence is maintained over a few millimeters so that $N_{eff} = n N$, where $n \cong 1$. Though this limits the resolution attainable with grazing incidence designs, it has the effect of allowing one to analyze the imaging properties of the spectrometer using ray tracing techniques.

In order to obtain the source limited resolution, differentiate λ in eq. (2-52) with respect to α and

substitute $\cos\alpha = r_1 / R$, to obtain

$$m N \frac{d \lambda_i}{d \alpha} = \left(\frac{r_1}{R}\right) 10^7 ,$$

or

$$\Delta\lambda_i = C_1 \frac{\Delta S}{mNR} \quad (\text{Å}), \qquad (2\text{-}56)$$

where $\Delta S = r_1 \Delta\alpha$ is the width of the entrance slit (μm), $C_1 = 10.989$ [2.32]. Substituting $\Delta\lambda/\lambda = \Delta E/E$ in eq. (2-56), we write eq. (2-56) as

$$\Delta E = C_2 \frac{E^2 \Delta S}{m N R} \quad (\text{eV}), \qquad (2\text{-}57)$$

with $C_2 = 8.87 \times 10^{-4}$, E photon energy (eV).

Our experiments were performed with slit width between 50 μm and 100 μm so that the slit width is the limiting factor in the resolution.

For grazing incidence optics, a spherical grating has very large astigmatism. This astigmatism can be partially corrected by the use of a toroidal grating with radius R in the plane of the Rowland circle and a smaller radius ρ in the direction perpendicular to this plane. The minor radius ρ may be chosen by the equation

$$\frac{1}{r_1} + \frac{1}{r_i} = \frac{1}{\rho} (\cos\alpha + \cos\beta_i) \qquad (2\text{-}58)$$

to obtain a first order correction. Here, r_i (r_i) is the distance between the center of the grating and the entrance (exit) slit of the spectrometer.

Eq. (2-58) has the form of a simple lens equaton with the focal length given by $f = 2\rho/(\cos \alpha + \cos \beta_i)$. Ray tracing study indicates that full refocusing in the perpendicular direction strongly degrades resolution. Ray tracing was used to choose a partial refocusing in the perpendicular direction that mantains resolution while reducing astigmatism. Some results of this ray tracing study are cited later.

III. SOFT X-RAY EMISSION SPECTROMETER

A. Introduction [3.1,3.2]

SXE spectrometer design faces the two major problems of low radiative yields, and low reflectivities of all materials in the soft x-ray region [3.3]. These two problems combined with the requirements imposed by the use of synchrotron source excitation generate a series of design constraints. Some of these are listed below.

1) All materials are absorbing so that windows and lenses can not be used and all experiments must be carried out in high vacuum. The high vacuum requirement is also imposed by the stringent vacuum and safety regulation necessary for operation at a synchrotron source, where the vacuum usually is kept below 10^{-9} torr. High vacuum has an additional benefit of reducing the degradation of optical reflectance caused by the deposition of hydrocarbons in the presence of the high energy synchrotron light.

2) Satisfactory reflectance can only be obtained at extreme grazing incidence, but images formed by spherical reflecting optics at grazing incidence have large aberrations. A

grazing incidence spectrometer with a large toroidal grating and slits located on the Rowland circle provides the instrument best suited to high resolution measurements over an extended spectral range in the far UV and soft x-ray regions. The toroidal gratings provide a first correction to the astigmatism associated with concave spherical gratings.

3) Grating spectrometers have fixed resolution in wavelength ($\Delta\lambda$) as has been shown in Sec.II D, so that energy resolution is rapidly degraded at small λ or high photon energy. In the spectrometer described here, four interchangeable gratings of 300, 600, 1200, and 2400 ℓ/mm are mounted in a vacuum chamber to provide a wide spectral range and meet resolution requirements.

4) The horizontal orientation of the storage ring beam, and narrow vertical angular dispersion of synchrotron light make it desirable to use vertical deflections in the beam line optics from synchrotron source to sample, and vertical dispersion in the SXE spectromenter. This characteristic is illustrated in Fig. 3-1, where the mirror in the bent mirror box and the gratings in grating chamber (refer to Fig. 3-3) are all mounted horizontally to provide vertical reflection of incident light.

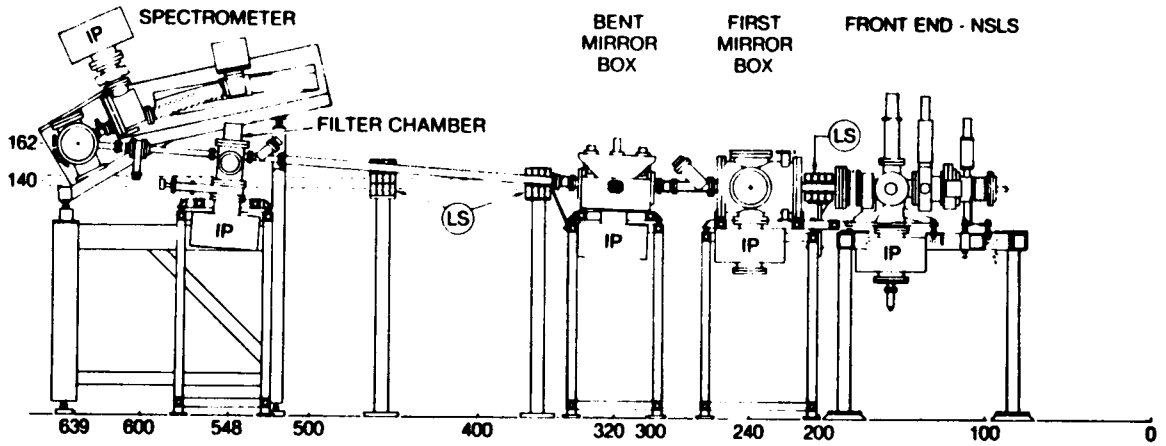

Fig.3-1
Diagram of synchrotron light beam line used for photon excitation of soft x rays and the SXE spectrometer.

5) Three special features contribute to the improved performance of the spectrometer. These are (a) the location of the input slit within a few millimeters of the sample surface to improve light collection efficiency; (b) the use of a large toroidal grating to reduce aberrational losses; and (c) replacement of the output slit with a two-dimensional (2D) detector system to improve both measuring efficiency and resolution.

In the next section, we will give detailed design parameters for the spectrometer. In the following section, we will focus attention on the detector system and its calibration. The overall performance of the spectrometer will be described in the last section.

B. Design Procedures [3.1,3.2]

The design goals for an optical spectrometer are to maximize detection efficiency of radiation while maintaining the energy resolution at a satisfactory level. The energy resolution for our spectrometer is set as < 0.3 eV below 300 eV, < 1.0 eV below 600 eV, and < 2.0 eV below 1000 eV. The Rowland circle design and angular parameters

are illustrated schemetically in Fig. 3-2.

A diagram showing construction details of the SXE spectrometer is shown in Fig. 3-3. It consists of three major chambers connected with each other by bellows: sample chamber, grating chamber, and detector chamber. The input slit, toroidal grating, and output spectrum lie on the Rowland circle. From Sec.II D, the radius of curvature of the grating in the optical plane must be equal to the Rowland circle diameter.

Entrance Slit Width. Since fluorescent emission is isotropic, maximum collection efficiency can be achieved by exciting fluorescence along a narrow line, which acts as the entrance slit of the spectrometer. From Sec.I D, the vertical height of light source at NSLS VUV ring is apporximately 120 μ. This source can be focused by a grazing incidence bent mirror to provide an equal or smaller image at the sample. So a minimum slit width of 50μ is assumed.

Rowland Circle Diameter. Refered to eqs. (2-55),(2-57), the resolving power can be limited either by the grating or by the spectrometer slit width. In our design, the resolution

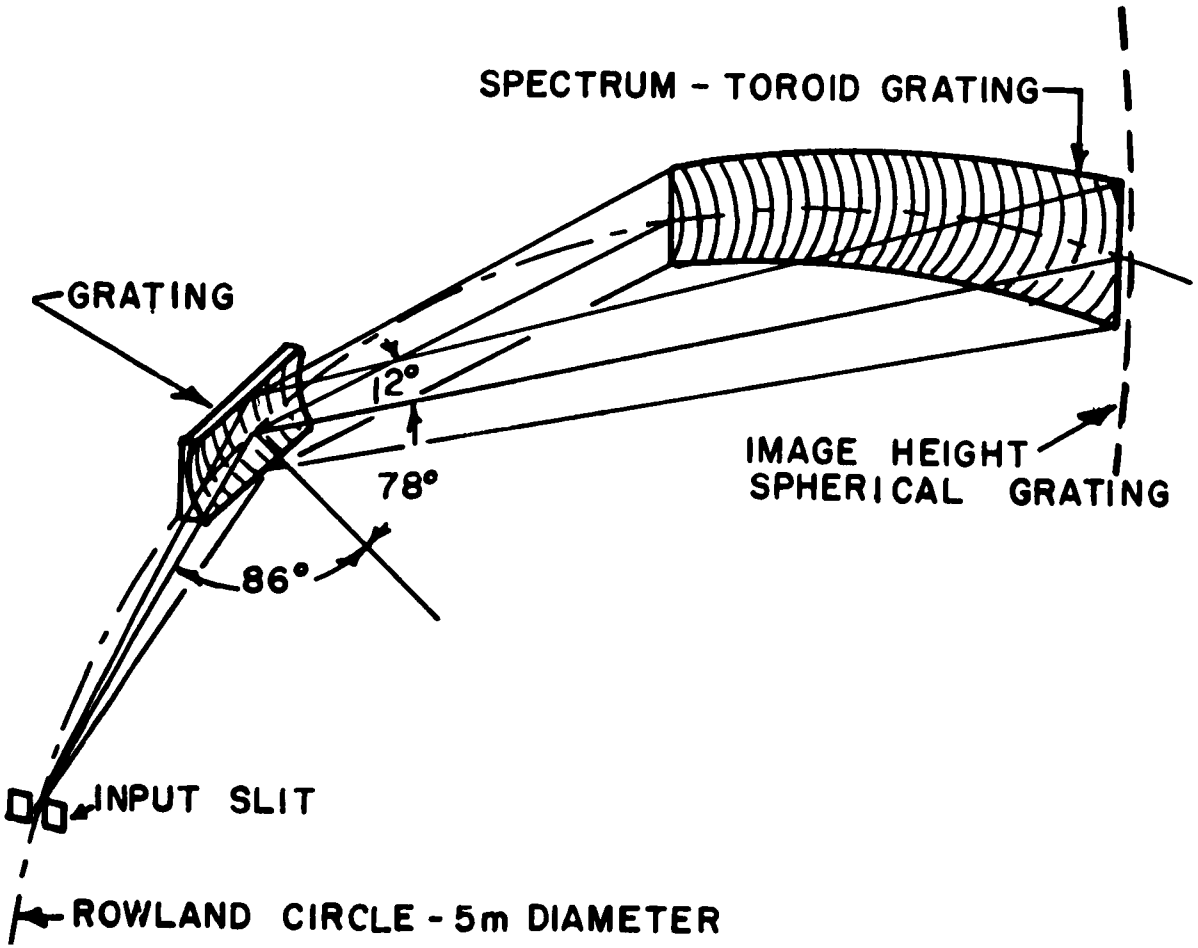

Fig.3-2
Rowland circle geometry. A point source at the input slit is dispersed and focussed in the dispersion direction by a curved grating of 5 m inplane radius of curvature. The astigmatism (height) of the image is reduced by a torodial grating with minor radius ρ = 50cm.

ORNL DWG. 86-8569

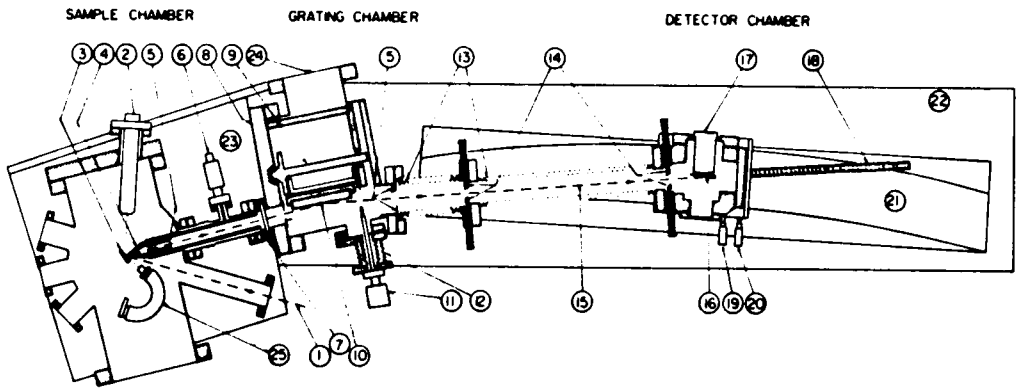

Fig.3-3
Diagram of soft x-ray spectrometer with cross section taken on the optic axis. Features designated by number are (1)light from SLS; (2)electron gun; (3)sample;(4)input slit; (5)light baffles; (6)Rowland circle adjust; (7)gate valve; (8) grating chamber support flange; (9) grating carousel; (10) toroidal grating; (11) grating adjust; (12) pressure compensation; (13) welded bellows; (14) light traps; (15) dispersed light; (16) microchannel plate; (17) fiber-optic bundle; (18) ball screw; (19) detector adjust rotation; (20) detector adjust translation; (21) Rowland circle track; (22) Diabase plate; (23) sample chamber support; (24) to ion pump; (25) electron spectrometer.

is determined by input slit width. Since an entrance slit width of $\geq 50\mu m$ has been determined, a Rowland circle diameter can be estimated by eq. (2-57). A 5m Rowland circle was chosen to meet the resolution requirement. The radius of curvature of the gratings is then also determined to be equal to 5m.

Incidence Angle. Incidence angle should be a compromise between good reflectance over most of the energy range of interest and high collection efficiency. 86° was adopted as the incidence angle. When the photon energy is in the 600 - 1000 eV range, an incidence angle of 88° can be used to enhance reflectance. The incidence angle is also used to determine the length of the grating. A 100 μm slit 5 mm from the sample surface subtends an angle at the sample that just fills the 10 cm long grating for a 86° angle of incidence. In practice, sample to slit spacings of 2~4 mm are used.

Mirror Radius for Gratings. In grazing incidence optics, concave spherical gratings have large astigmatism. A first order correction can be obtained by using gratings ruled on toroidal substrates. The determination of the minor

radius for a toroidal grating may be made from calculation and ray tracing studies. Substituting with R = 5m, $\alpha = 86^{\circ}$, $\beta_i = 86^{\circ} \sim 78^{\circ}$ in eq. (2-11), we find that 2.4cm $\leq \rho \leq$ 7.3 cm. For a minor radius ρ = 5 cm, a first-order focus will be at an exit angle of 81.5°.

The use of a toroidal grating surface reduces the elongation of the image, but not the depth of the curvature [3.5]. Ray-tracing studies show that a minor radius for the grating of ρ = R / 10 = 50 cm renders the rays leaving the grating approximately parallel over the scanning range of the spectrometer. They also show that it is not desirable to use stronger focusing to refocus the rays at one point on the output plane. Even at the "in-focus" point, residual aberrations give very poor resolution. In effect, the elongated curved image is collapsed onto the focal plane as a bullet-shaped image whose width equals the sagitta of the astigmatic image [see 81.5° image of fig. 3-4(a)].

The effects of partial and complete refocusing are illustrated in Fig. 3-4, taken from ray-tracing studies[3.6]. An input slit of dimensions 0.05 X 12 mm^2 is imaged at points on the output plane by partially refocusing (Fig. 3-4

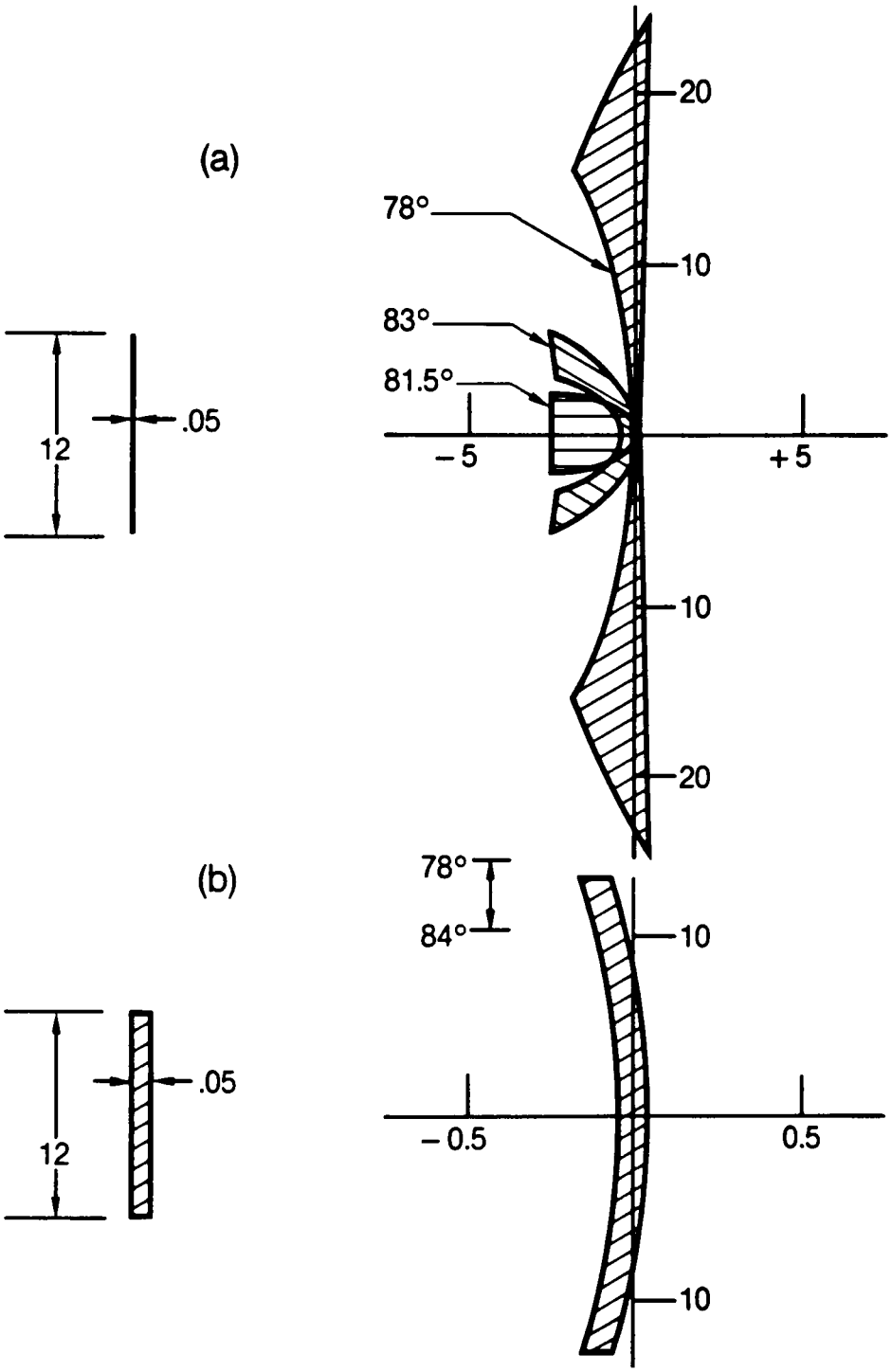

Fig.3-4
Focusing properties of toroidal gratings from ray-tracing studies. Input slit at left (12x0.05 mm^2) is imaged at right by 2x10 cm^2 gratings with R=5.0 m major radus and 86 angle of incidence. The minor radii for the two cases shown are (a) ρ=5 cm which provides a first-order focus at an exit angle of 81.5, and (b) ρ=50 cm, which is the minor radius of gratings installed. Note change in horizontal scale between (a) and (b). All dimensions are in mm.

(b)) and fully refocusing (Fig. 3-4(a)) toroidal gratings. It is clear from Fig. 3-4 that the best resolution and light collection can be obtained with a partially refocused image and a detector of modest size (25 mm diameter) that can compensate for image curvature.

A minor radius of ρ = 50 cm was chosen. This minor radius provides an image over the full scanning range whose height is compatible with a 2D detector having 25mm diameter.

Detector Choice. A gain of about 100 in measuring efficiency can be obtained by replacing the scanning output slit of the spectrometer with a position sensitive detector so that large regions of the spectrum can be measured simultaneously. A microchannel plate (MCP) with 25 mm diameter mounted tangent to the Rowland circle was choosen as the first stage for this photon detector-amplifier system. A detailed description of the detector system is given in the next section.

Arrangement of Gratings. In order to build a 5 m Rowland circle spectrometer of moderate size, with a wide scanning range (20-1000 eV),and with good energy resolution,

it is necessary to use multiple gratings. Since grating spectrometers have a fixed wavelength resolution for a given grating and slit width, lower dispersion gratings allow spectra to be scanned to longer wavelength (and lower energy) while retaining acceptacle energy resolution.

Our design uses four interchangeable graings of 300, 600, 1200, and 2400 ℓ/mm. The gratings are originals ruled in gold on fused silica substrates with toroidal surface figures of major radius R = 500 cm and minor radius ρ = 50 cm[3.7]. The mechanical drive allows the detector to be scanned between output angles of 86° and 78° on a curved track about 1 m long.

Energy Resolution. Figure 3-5 plots energy resolution versus scanning range for the four grating, assuming an incidence angle of 86° and output diffraction angles between 86° and 78°. The 2400 ℓ/mm grating provides 0.5 eV resolution to a maximum energy of 390 eV. Other gratings provide lower resolution but wider scanning ranges.

C. MCP-CCD Detector System

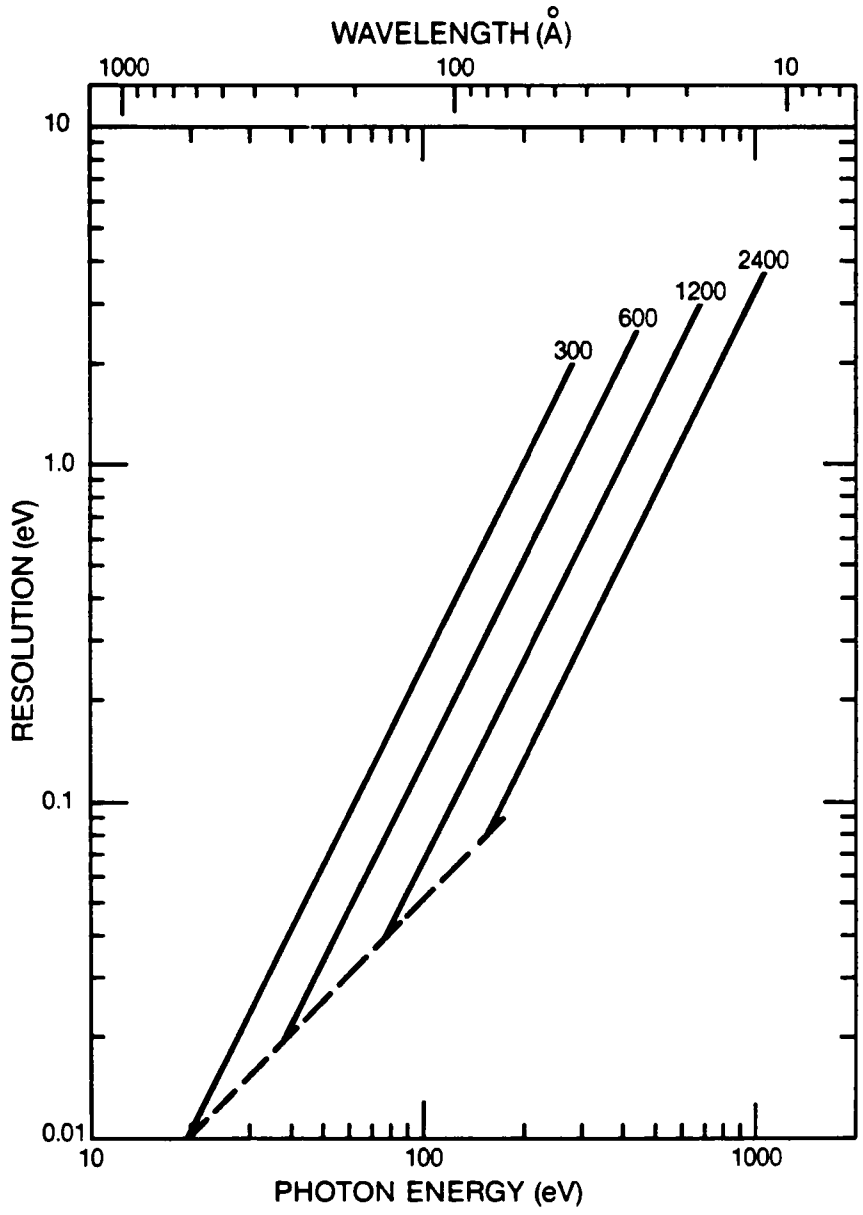

Fig.3-5
Resolution of four gratings installed in spectrometer using 50 μm input slit width. The curves are labeled with the ruling density of the gratings in lines/mm. The dashed line is the long wavelength scanning limit of the spectrometer.

General Features. The detector system is a MCP image intensifier/converter[3.8] which is coupled by fiber-optic bundles (FOB's) to a two-dimensional charge-coupled-device (CCD) Si diode detector[3.9]. A schematic of the detector system is shown in Fig. 3-6. A soft x-ray photon is converted to a photoelectron and amplified by the MCP. The exiting electrons are proximity focused and accelerated to impinge on a P-20 phosphor, which converts the electrons to visible light. The phosphor is coated on the input face of a FOB which is optically coupled with the CCD. One segment is a FOB taper which reduces the image by a factor of 2:1 [3.10]. The high sensitivity, the low noise level, and the integrative nature of the CCD make this a very powerful tool for detecting extremely weak signals such as the SX fluorescence from solids.

The MCP has a 25-mm-diam active area and 12-μm-diam pores with 15 μm center-to-center spacing. The channels are biased 10° from the MCP surface normal. To enhance the quantum efficiency of the MCP, its front surface is coated with 1000 Å of MgF_2 [3.11]. The MCP is funneled to increase the open area from 55% to 73% and also to improve operation in the grazing incidence configuration. The funneled MCP

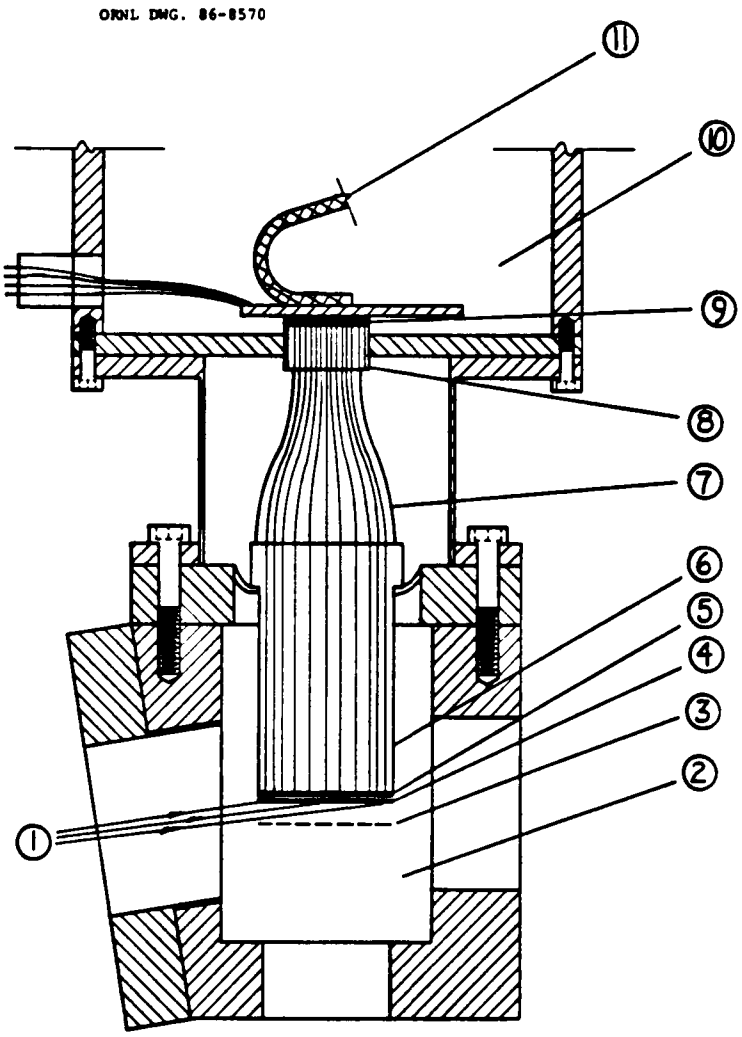

Fig.3-6
Diagram of detector system. Features designated by numbers are (1) SX radiation from grating; (2) UHV detector chamber; (3) retarding screen; (4) microchannel plate; (5) P-20 phosphor; (6) fiber-optic bundle (FOB); (7) FOB taper; (8) FOB; (9) CCD Si-diode detector; (10) liquid nitrogen cryostat; (11) cooling strap.

coated with MgF_2 has a quantum efficiency of about 10% when it is operated in the SX region (< 500 Å) and at grazing incidence angle (10°~20°) [3.12]. The MCP operating voltage is varied from 600 to 1000 V depending on the application. Over this range the electron gain varies from 2×10^2 to 2×10^4. In addition to converting the electron energy to visible radiation, the phosphor layer provides a gain of the order of 1~100 visible photons/incident electron for 1~5 keV electrons [3.13]. A retarding screen is mounted in front of the MCP to ensure collection of back emitted electrons. It has been found that the retarding screen not only increases the sensitivity of the MCP but also improves the resolution [3.14]. In our recent experiments, the bias conditions are: back of MCP, 0V; surface of MCP, -0.85 kV; retarding screen, -1.2 kV; and phosphor layer, 3.0 kV.

The CCD is a buried channel type and has 576 X 384 pixels [3.9]. Each pixel has a dimension of 22 X 22 μm^2. The CCD has a FOB window and is cooled under vacuum in a liquid nitrogen cryostat. When cooled to -100 °C or below the CCD has very small dark current and has less than 50 electrons/pixel readout noise. It has a maximum quantum efficiency of 85% at a wavelength of 550 nm.

The CCD is read by a slow-scan camera with a 14-bit digitizer [3.15]. The entire 576 X 384 pixels can be read or selected portions thereof. The charge collected on adjacent pixels can be added together (binned) before readout to reduce the readout noise. The number of pixels to be binned together in the dispersion direction is determined by the resolution required, and ultimately by the parameters of the spectrometer. Appendix A gives the equations used to select the pixel binning which meets the resolution requirement. For the present experiments, four adjacent pixels in the dispersion direction and 20 pixels in the perpendicular direction are binned together as one data point. From the Appendix A eq.(A-6) and table A-1, it can be estimated that the 4 X 20 pixels binning assures at least one data point per resolution element even under conditions requiring the highest resolution. For the work reported here, 128 X 16 data points binning the central 512 X 320 pixels are read for each spectrum. The final spectrum is obtained by appropriately shifting and summing the 16 slices of the spectrum.

A block diagram of the data acquisition electronics is shown in Fig. 3-7 . The parallel data output from the CCD

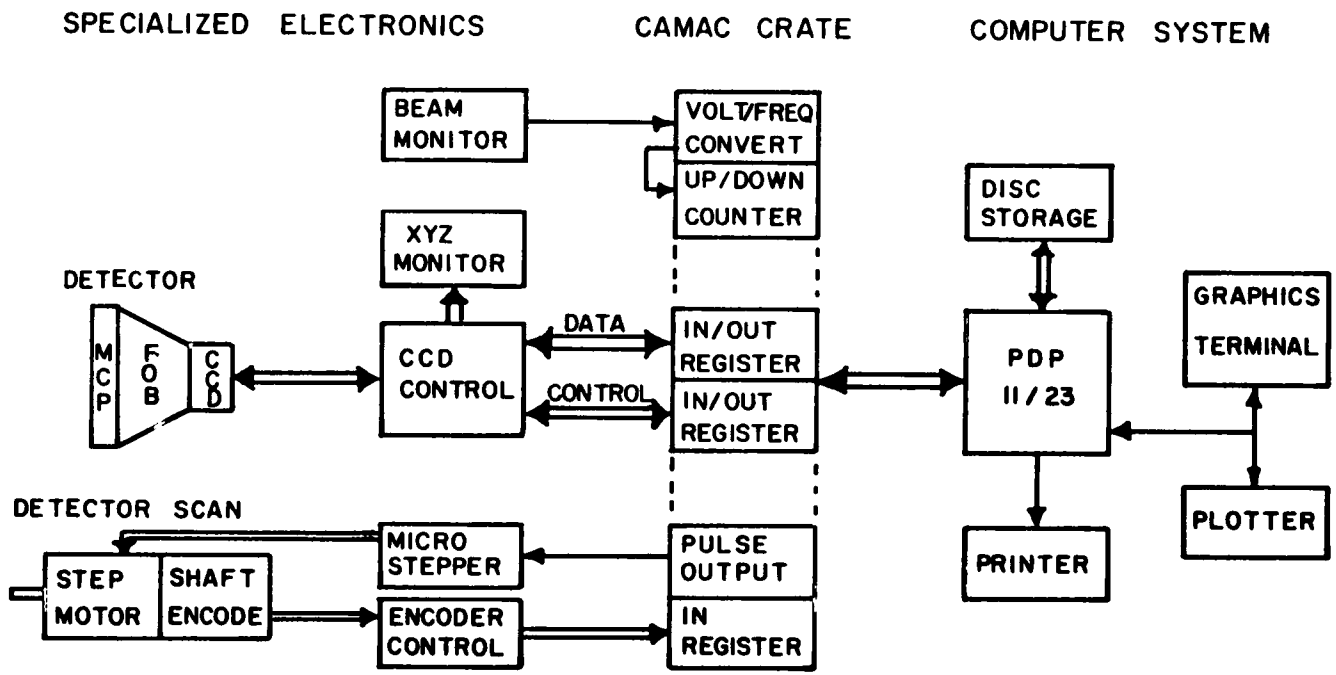

Fig.3-7
Diagram of data-acquisiton electronics.

controller is interfaced directly to a CAMAC 16 bit input register (I/R). The data temporarily stored in the I/R is immediately fetched by the PDP 11/23 computer and then stored in the storage volume. Other circuits in the data acquisition electronics position the detector and integrate the flux of exciting photons or electrons.

Calibration of MCP-CCD System. This complex detector system has performed very well for the acquisition of very weak spectra. A complete characterization of the system's quantum efficiency and imaging performance is a complex problem that has only been partially solved. In the following paragraphs, we describe our calibration procedures and present measures of performance that we have determined to date.

To obtain meaningful data in a display type instrument, it is essential that the detector be calibrated to compensate for nonuniform response across the 2D detector. A routine method for carrying out this calibration has been worked out and is described below.

Nonuniformities in the quantum efficiency of the MCP, in the gain of the MCP, in the phosphor response, in the FOB

optical transmission, and in the response of the CCD may all produce nonuniform lateral response of the system. In addition, thermally induced dark currents may be generated in the MCP and CCD, and readout noise is generated when the analog signal from the CCD is read out and digitized. The overall strategy is to subtract the background of dark current and readout noise, and to determine a transmission coefficient which includes all factors which affect the intensity of the desired signal. In processing emission spectra, the background is subtracted from the CCD readout, and the difference is divided by the transmission coefficient to compensate for the nonuniform lateral response.

It is possible to determine a transmission coefficient for each pixel of the CCD. To reduce the time necessary to obtain adequate statistics for the calibration, it is our usual practice to calibrate transmission coefficients for each bin of (4 X 20) pixels that is digitized as a unit when the CCD is read out.

Two calibration methods have been tried. An attemped calibration using the uniform output of the synchrotron light source (SLS) was not satisfactory because of

excessive light scattered by the spectrometer bellows. New light traps and baffles may make this type of calibration practical in the future.

The present calibration procedure is to move the detector in small steps so that a strong spectral feature, which should be maintained at a constant intensity until the total procedure is finished, is scanned across the detector. The transmission coefficient is calculated from the response of the detector. The general procedure has been implemented with the methods described in detail in Appendix B. Using method B in Appendix B, the two curves shown in Fig. 3-8, were obtained which show the overall response of the detector system in the dispersion direction. The curves were obtained at peaks in the aluminum $L_{2,3}$ spectrum (171 Å) and in the silicon $L_{2,3}$ emission spectrum (134.7 Å) using 40 μA of 2-kV electrons for excitation and the 600 ℓ/mm grating. Fig. 3-9 displays the same 171 Å curve as shown in Fig. 3-8, but using an improved method (method C in Appendix B). We notice the tremendous reduction of random noise made possible by the later method, which fully utilizes the data available from numerous exposures.

From the figure 3-9 it is clear that the transmission

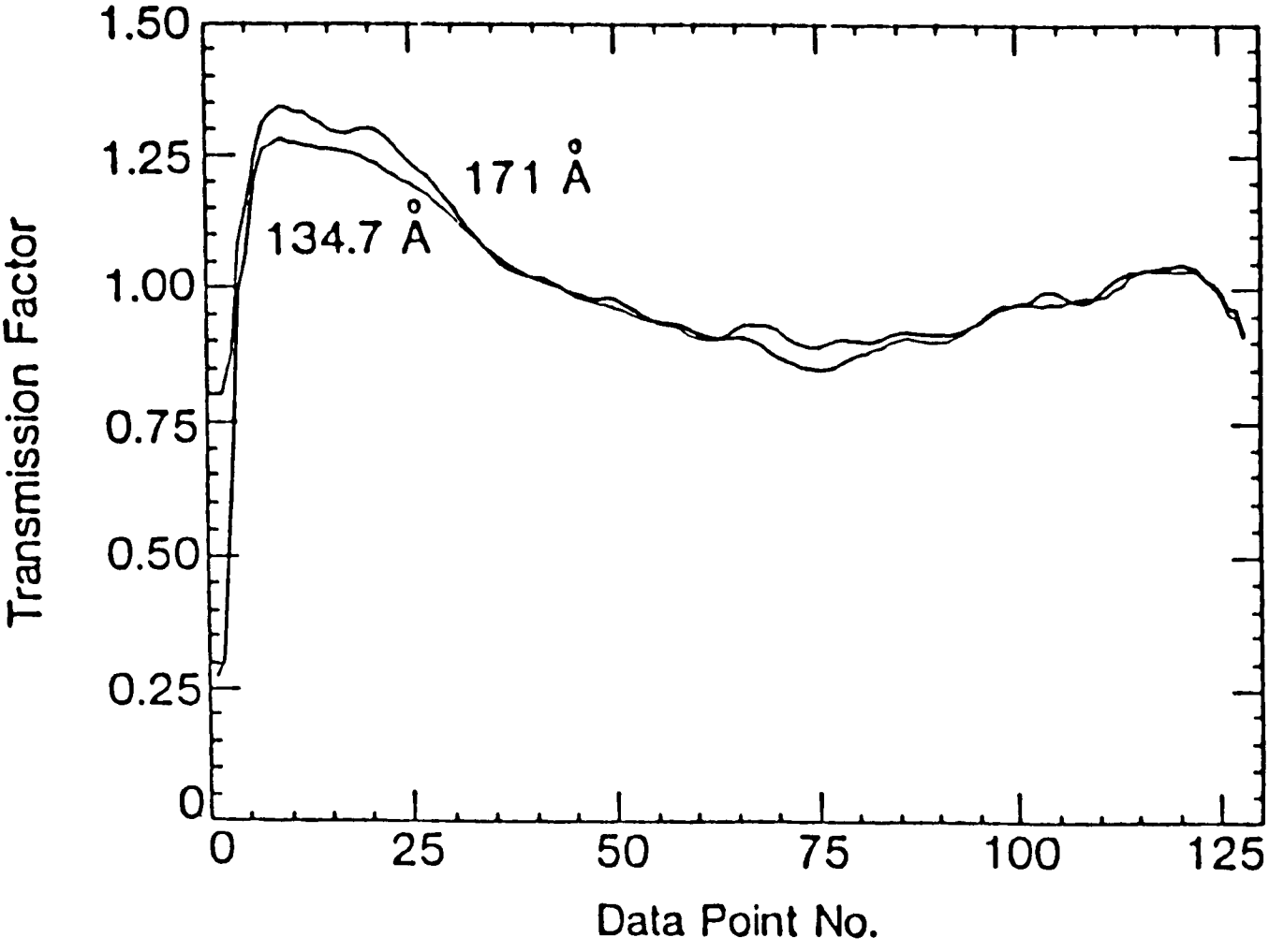

Fig.3-8
Average lateral response of the 2D detector in the dispersion direction, obtained by averaging over the orthogonal direction using Method B in Appendix B. In processing experimental data, separate response curves of this type are generated for each of 16 strips along the CCD. Curves are labeled with wavelength of emission peak used to perform the calibration.

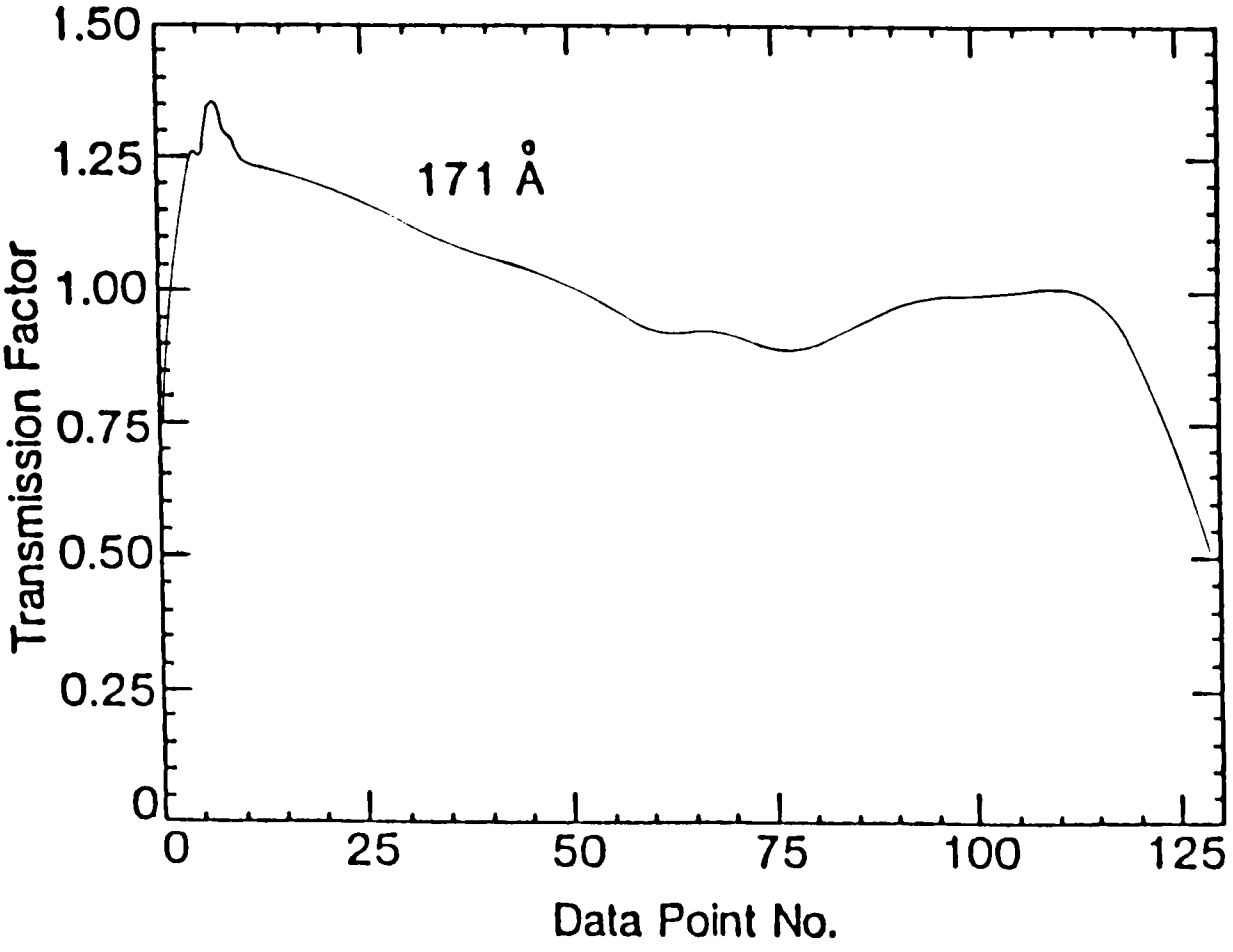

Fig.3-9
Same response curve using Method C in Appendix B. Note the great reduction of random noise along all data points.

coefficients are rather uniform at the center and increase toward the edges. The sharp decrease at the extreme edge is caused by a mismatch between the FOB image and the CCD. Both the gain of the MCP and nonuniformities of the FOB taper response may contribute to the increase in transmission near the edges of the detector. It is also observed that the transmission coefficient calibration changes slightly as the detector is moved along the Rowland circle. This occurs because the incidence angle of the light changes as the detector is scanned. The changing transmission factor imposes an additional requirement that a calibration should be made with the detector near the position on the Rowland circle where data are to be taken.

The accuracy of the lateral calibration is illustrated in Fig. 3-10, which shows an e-beam excited Al spectrum. Using the 600 ℓ/mm grating, the width of this spectrum exceeds the width of the detector so that the emission spectrum must be assembled from three separate segments. The excellent matches where the spectra overlap confirm the accuracy of the calibration procedures.

Absolute Response of MCP-CCD System. An estimate of

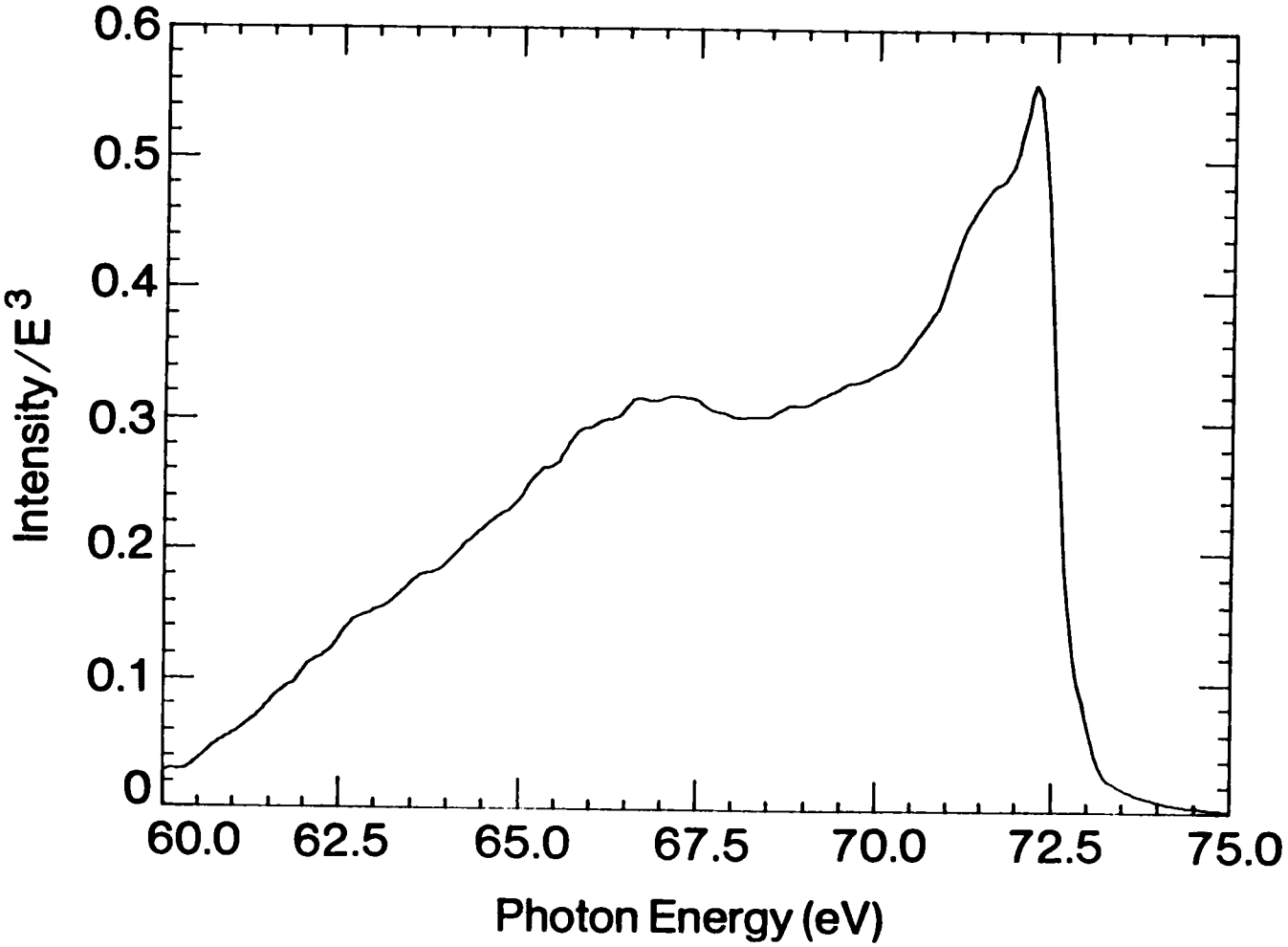

Fig.3-10
Aluminum $L_{2,3}$ spectra assembled from data obtained in three adjacent spectral regions. Note good fit in regions of overlap. Exposure conditions are 100 μm input slit, 600 ℓ/mm grating, 20μA of 2 kV e-beam exciation. Exposure time is 30 sec per section.

the absolute response of the detector system can be made by determining the gain of each component of the detector system and multiplying them to obtain an overall response. It should be noted that the gains of the MCP and of the phosphor are both strong functions of applied voltage and that the quantum efficiency of the MCP surface depends on the angle of incidence and the voltage on the retarding screen. Thus the estimates are illustrative rather than definitive in nature.

In a calibration run, we found that 20 μA of 2 kV electrons produced a digital reading of 650 counts per second from the CCD near the maximum of the Al $L_{2,3}$ spectrum. These counts are summed for the central ten slices of the spectral image and thus represent the output of ten 80 pixel bins or a slice four pixels wide in the dispersion direction by 200 pixels long in the direction perpendicular to the plane of the Rowland circle. Each count represents 20 electrons so that 20 X 650 = 13000 electrons/s are collected. The gain factors of the detector system components are taken to be: quantum efficiency of CCD = 0.85 ; transmission of FOB optics = 0.50 [3.7,3.8,3.9]; gain of phosphor with 2 kV bias = 1.0 [3.13]; gain of MCP

with 850 V bias = 3000 [3.7,3.8]; quantum efficiency of the MCP surface with MgF_2 overcoat, 10° incidence angle, and 500 V retarding screen potential = 0.10 [3.15]. Dividing the number of electrons by these factors, we estimate the photon flux to be 13000/(0.85X0.5X1X3000X0.1)=100 photons/s/800 pixels. Thus we produce about 130 electrons and 6.5 counts per incident photon so that the detector easily resolves single photon events. Since this count rate represents the output of 800 CCD pixels, it represents about 0.125 photons/s/pixel when the incident photon flux is projected through the detector system onto the CCD.

The number of photons incident on the detector may also be estimated from the source intensity and properties of the spectrometer. For electron excitation, the source strength may be estimated from a knowledge of electron energy, electron current, electron scattering lengths for core excitation, and fluorescent efficiency. Beam size, collection solid angle, and grating efficiency affect the transmission of emitted SX radiation to the detector. From these factors, we calculate that approximately 60 photons/s/800 pixel spectral slice will arrive at the detector. Given the uncertainties in many of the factors

ment to

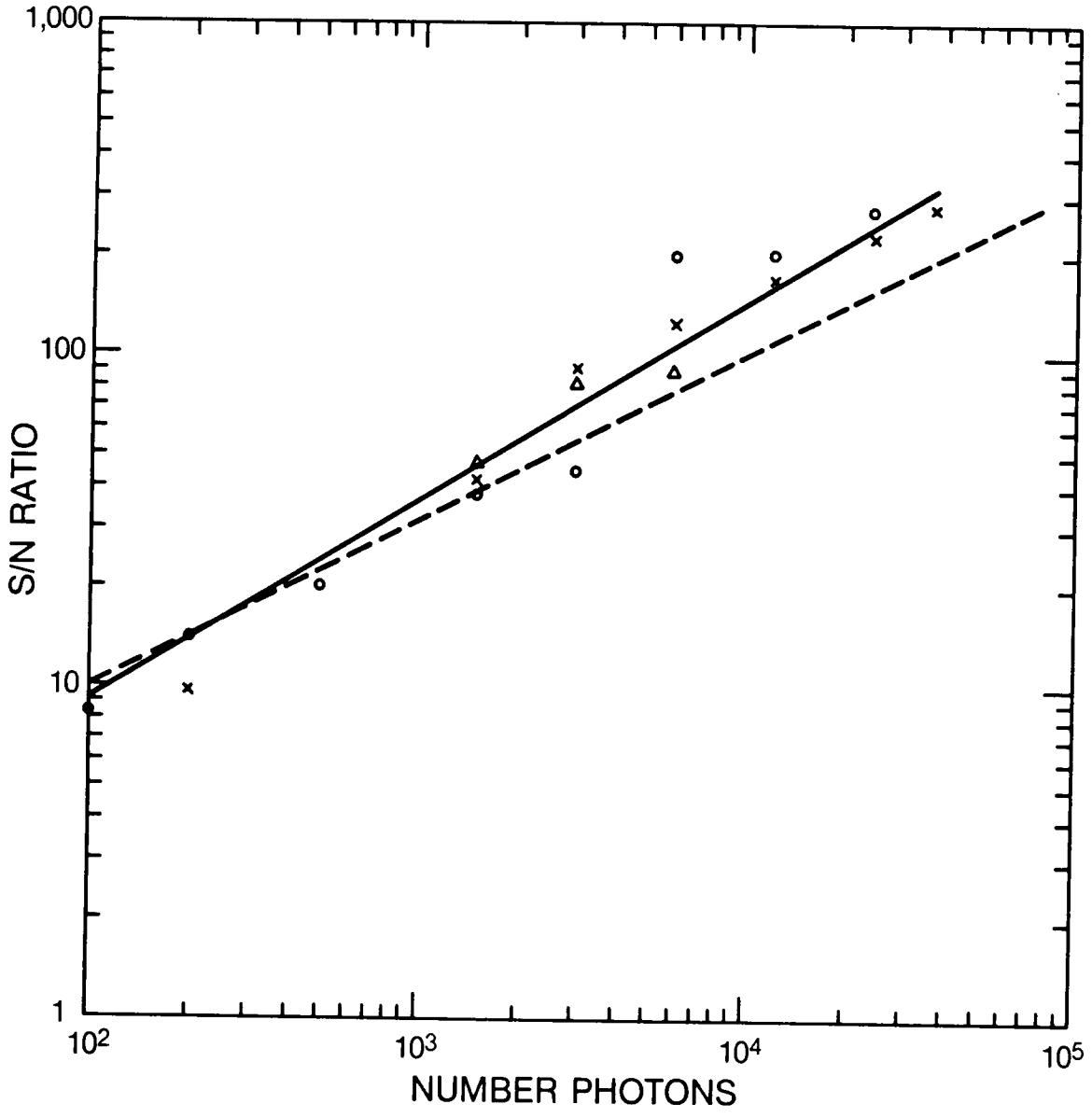

Fig.3-11

Signal-to-noise ratio for the detector system. Solid line obtained as described in section C. Dashed lines is $N^{1/2}$, where N is number of photons counted.

steeper slope but is in reasonable agreement with this curve. It shows no evidence of saturation at the highest signal levels measured.

D. Performance of Spectrometer.

The overall capability of the spectrometer with e beam excitation is illiustrated by the results shown in Fig. 3-10 for the aluminum $L_{2,3}$ spectrum and in Fig. 3-12 for the Si spectrum. The silicon spectrum was excited with 43 μA of 2 kV electrons. It was recorded in two segments with a 15 s integration time for each segment. A third 15 s integration was performed to record a background for subtraction so that a total time of 45 s was required to obtain this spectrum. The satellite shown in the insert was obtained with a 5 min integration time.

It is very difficult to compare spectra obtained with different spectrometers due to differences in resolution, source geometry, brightness, and many other factors. It is, nevertheless, instructive to make some rough comparisons of measuring efficiency. We define measuring efficiency as follows: for a display type spectrometer, the measuring

ORNL DWG. 86-8565

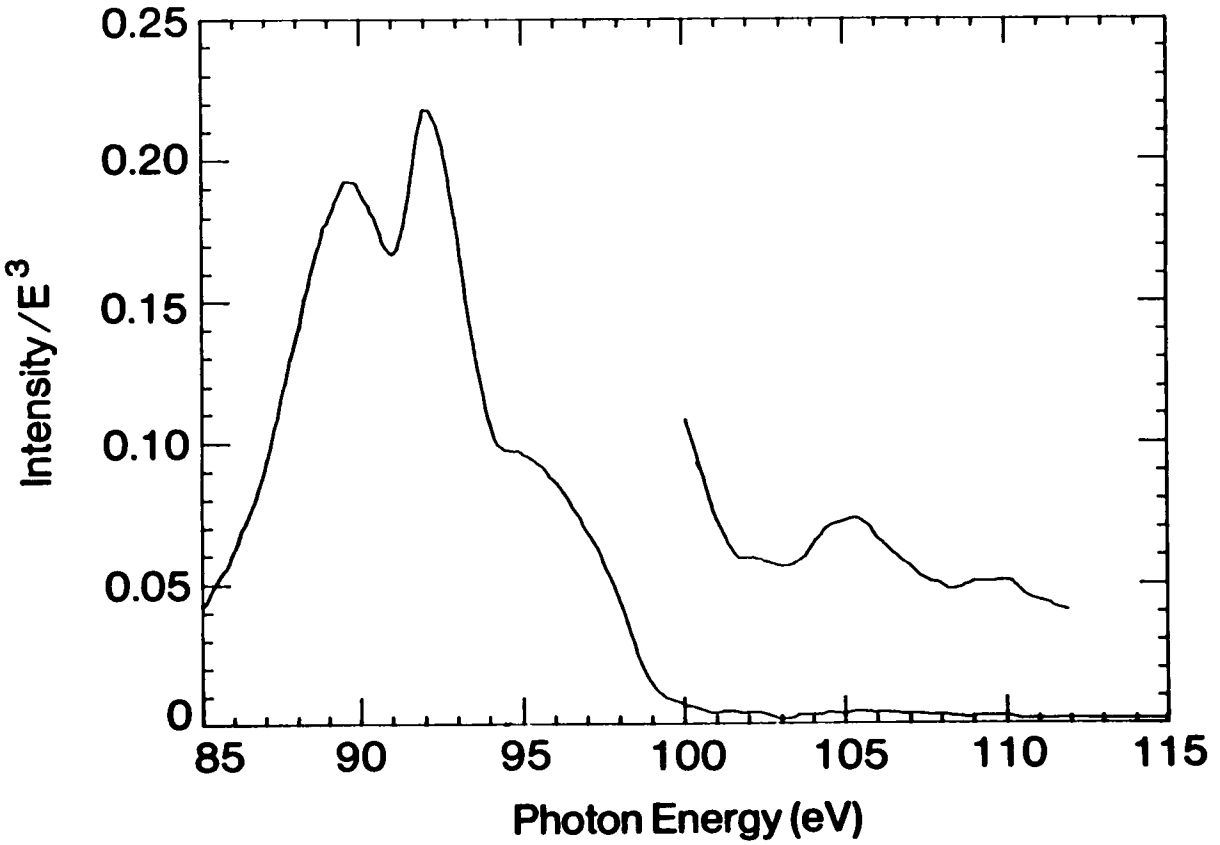

Fig.3-12
Silicon $L_{2,3}$ spectra showing primary spectrum and satellite with approximately 1.0% the intensity of the primary spectrum. Exposure conditions are 100 μm input slit width, 600 ℓ/mm grating, 43μA of 2 kV e-beam excitation,exposure time per section is 15 s for primary peak, 300 s for the satellite.

efficiency is the product of the sensitivity per resolution element times the number of resolution elements contained in the detector array; for a conventional spectrometer, the measuring efficiency is just equal to the sensitivity per resolution element, since it has only a single detector.

Before comparing our results to those obtained with other instruments, we note several things that affect those comparisons. In a display type instrument, the spectral intensity is inversely proportional to resolution so that an n-fold improvement in resolution requires an n-fold increase in integration time or source strength to maintain the same S/N ratio. In a single channel instrument, an n-fold improvement in resolution requires an (n^2) increase in integration time or source strength to maintain the same S/N ratio. Similarly, since S/N is proportional to the square root of the number of counts, an n-fold increase in S/N requires an (n^2) increase in integration time or source strength for either type of spectrometer.

Aluminum $L_{2,3}$ spectra similar to that displayed in Fig. 3-10 have been measured by workers at Oak Ridge National Laboratory (ORNL) [3.16] and at the University of Virginia [3.17]. The ORNL data were taken using 10 mA of 2 kV electron

excitation in about 10 min with resolution 4 times poorer than our data and with slightly poorer S/N ratio. The data in Fig. 3-10 were taken in about 1 min with 40 μA of 2 kV electron excitation. Ignoring differences in S/N ratio, the measuring efficiency of the spectrometer described here exceeds that of the ORNL instrument by a factor of 250 in excitation current, an additional factor of 4 in resolution, and another factor of 10 in measuring time to give an overall improvement in measuring efficiency exceeding 10^4.

Carson et al. published a spectrum taken with the University of Virginia display type spectrometer [3.17]. The spectrum was obtained in a 300 min integration time using 1.0 mA of 3 kV electron excitation. We estimate its S/N ratio to be ∿60 as compared with our S/N ratio of ∿30, and the resolution to be better than that of Fig. 3-10 by a factor of about 2. Ignoring differences in excitation energy, we would need to extend our measuring time by a factor of X 2 to obtain equal resolution and X $(2)^2 = 4$ to obtain an equal S/N ratio, or by a factor of about 8 to reproduce the University of Virginia data. Our data would still be obtained with less than 1/35 the measuring time and

with 1/23 the excitation current to give a net difference of measuring efficiency of about a factor of 900. we suspect that much of this difference results from the excellent light collection efficiency and the relatively high grating efficiencies of our instrument.

IV. BEAM LINE

A. Beam Line Design.

The beam line used to excite emission with radiation from a SLS is shown in Fig. 3-1 in the configuration that has been used at the National Symchrotron Light Source (NSLS) at Brookhaven National Laboratory (BNL). The beam line used at the Synchrotron Ultraviolet Radiation Facility II (SURF II) at the National Bureau of Standards (NBS) was identical except for the front end and first mirror box which are unique to NSLS. At SURF II, a plane gold mirror producing 14° of horizontal deflection was located in the beam line up-stream of the mirror box containing the bent mirror focusing toroid.

The major components of the beam line are identified in Fig. 3-1. The NSLS front end [4.1] contains a UHV gate valve to isolate the port in normal operation, a second fast acting gate valve to isolate the port in case of catastrophic vacuum breakdown or other emergencies, a 15 cm thick tungsten alloy radiation shutter, ion and titanium sublimation pumping, and various safety interlocks

and vacuum monitoring devices.

The first mirror box divides the 90 mrad of horizontally diverging light available at the port into two beam lines on either side of the port center line. Our beam line, designed U10A, utilizes 15 mrad centered about a line 30 mrad from the port center line. As presently configured, this chamber contains no deflection optics, but does contain tungsten alloy radiation shutters and UHV isolation valves on its down-stream ports that allow independent operation of the two beam lines sharing the port.

Focusing is provided by a toroidal mirror with 88° angle of incidence, a major radius of 92 m, and minor radius of 5.0 cm which provides one-to-one focusing of the SLS electron beam on the sample. The toroid is formed by bending a 33.0 X 7.5 X 2.0 cm^3 cylindrical silica mirror supported on 30 cm centers using compression points separated by 20.3 cm along the mirror [4.2]. The region of the mirror between the compression points has a parabolic figure closely approximating the circular figure of a true toroid [4.3]. The maximum effective area of the mirror is 20 X 5 cm^2 which provides a maximum angular

acceptance of SLS radiation of 16 horizontal mrad and 2.2 vertical mrad. The mirror (uncoated at SURF and gold coated at NSLS) has a specified surface finish of < 50 Å rms surface roughness. Ray-tracing studies indicate that the toroidal figure provides good image quality at magnifications near 1 but degrades rapidly at other magnifications. With the full effective mirror area illuminated we observe that a 0.3 mm diam beam in the SURF storage ring is imaged to a width of less than 0.5 mm on the sample. An alternative beam line has been designed which employs two ellipsoidal mirrors in a common axis of rotational symmetry (CARS) design [4.4]. It would provide excellent image quality at a demagnification of 1/4 and may be installed at some future time.

The filter chamber provides a means of introducing absorption filters into the beam line to limit the wavelengths used for excitation. Appropriate filters can be used to reduce or eliminate light in the spectral region in which emission is being measured. By reversing the spectrometer so that SLS radiation illuminates the spectrometer entrance slit directly, the filter chamber can also be used as a sample chamber for absorption studies.

An essential modification required to prepare the spectrometer for use with photon excitation is the introduction of light traps and baffles (5 and 6 in Fig. 3-2) to reduce scattered light. Light traps are constructed from stacks of razor blades. Fixed traps are placed to intercept incident light which just misses the grating and to collect the zero-order spectrum from the grating. Adjustable traps are located on both ends of the main bellows between grating and detector chamber, and are used to reduce the amount of first order light scattered off the bellows onto the detector. For best results, the adjustable traps must be reset for each spectral region of interest. Consequently, they are designed to allow adjustment from outside the vacuum.

B. Flux Distribution and Power Load

The photon spectrum available for excitation when the SURF II storage ring is operated at 280 MeV is illustrated in Fig. 4-1. Curve N_0 shows the photon flux available from the light source [4.5]. Curve N_1 shows the flux available after the light has been horizontally deflected through 14°

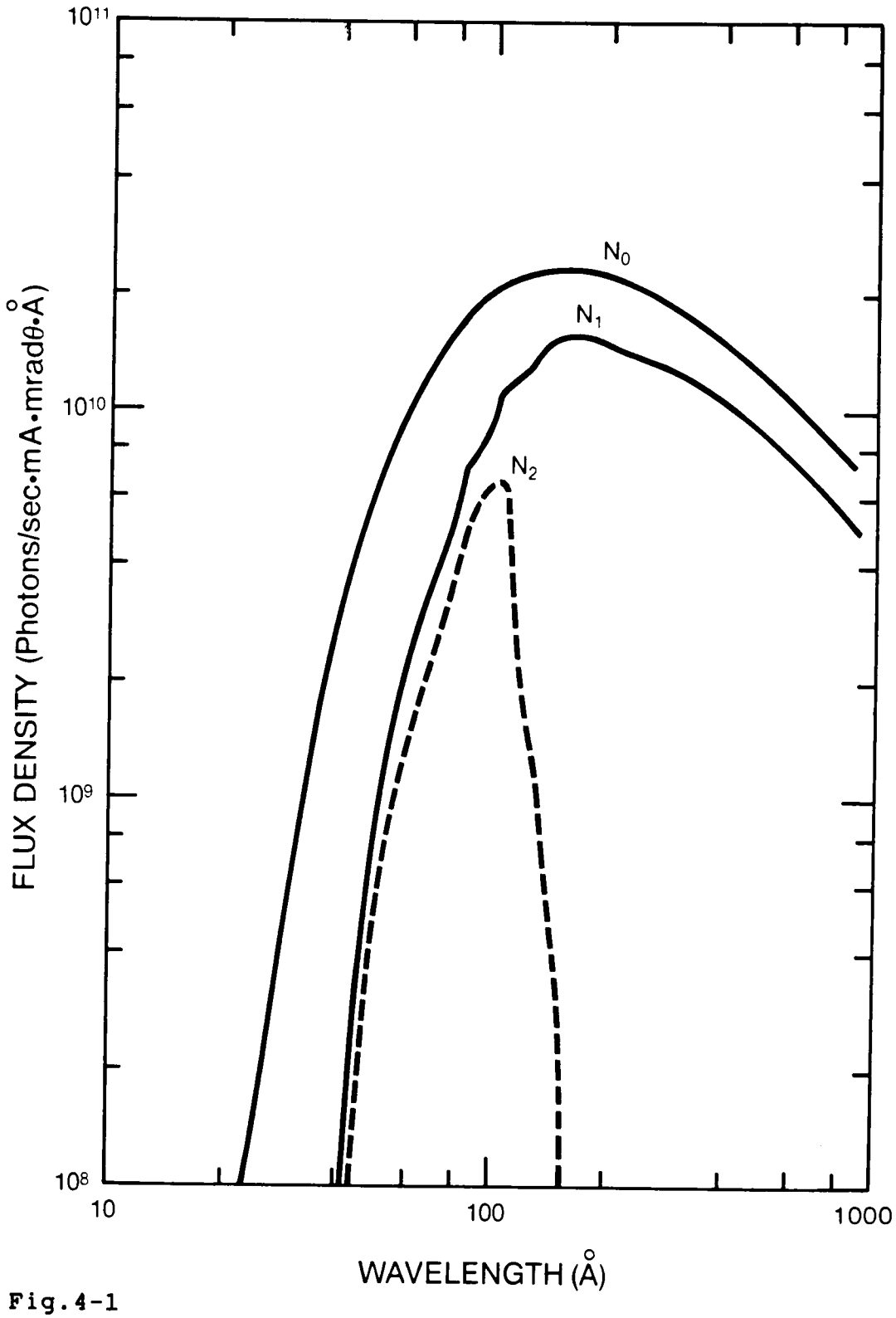

Fig.4-1
Fluxes available for excitation of samples at the NBS SURF II synchrotron light facitlity. N_0 designates spectrum available with 280-MeV electrons in storage ring. N_1 designates light available after reflection from Au and SiO_2 mirrors. N_2 is spectrum passing a 500 A silver absorption filter.

by the gold mirror and vertically deflected through 4° by the fused silica toroidal mirror [4.6,4.7]. The most severe losses occur at short wavelengths where the large angle of grazing incidence on the gold mirror (7°) limits the reflectivity [4.6]. Curve N_2 shows the spectum after a 500 Å thick silver absorption filter is introduced into the beam [4.6]. The N_2 spectrum is particularly suitable for the excitation of emission spectra below 100 eV because it effectively eliminates the scattered light from the illumination spectra in this spectral region. Design studies are currently underway for the use of transmission gratings as passband filters for the exciting light [4.8]. These should provide much better selectivity of excitation wavelengths in the future.

Fig. 4-2 and Fig. 4-3 are photon spectra of our beam line when connected to the 750 MeV VUV storage ring at the BNL NSLS. In both cases, the VUV ring is operated at 750 MeV. In Fig. 4-2, a vertically reflecting mirror with 2° grazing angle is used to form the image on the sample with a magnification of 1. The photon flux distribution following this quartz mirror shows that the high energy part of flux is sharply attenuated. Two silver filters have been used in this

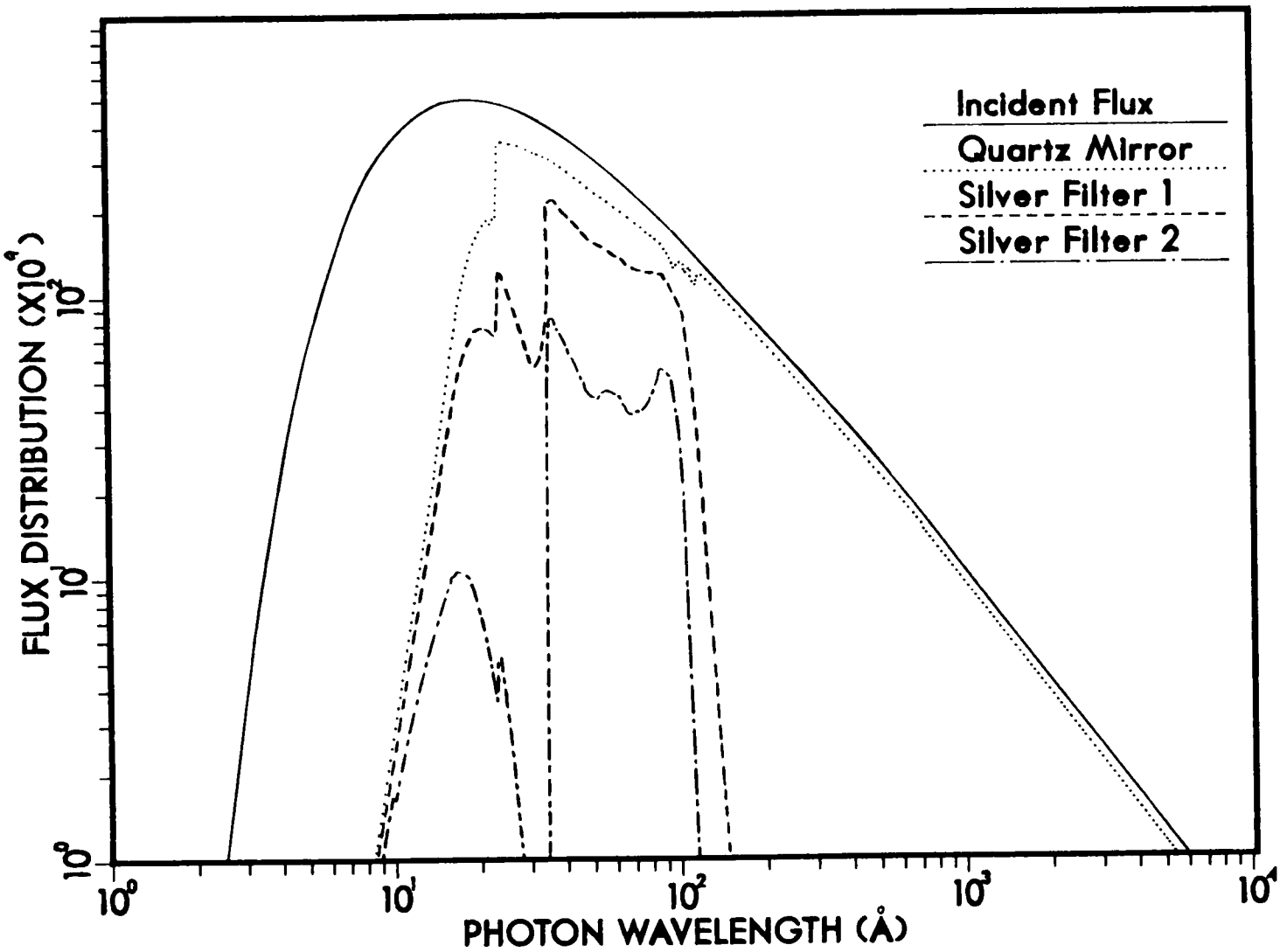

Fig.4-2
Flux distributions 1 at the BNL NSLS VUV ring. The light through a SiO_2 mirror with 2 grazing angle passes a silver filter (1 for 500 A, 2 for 2000 A).

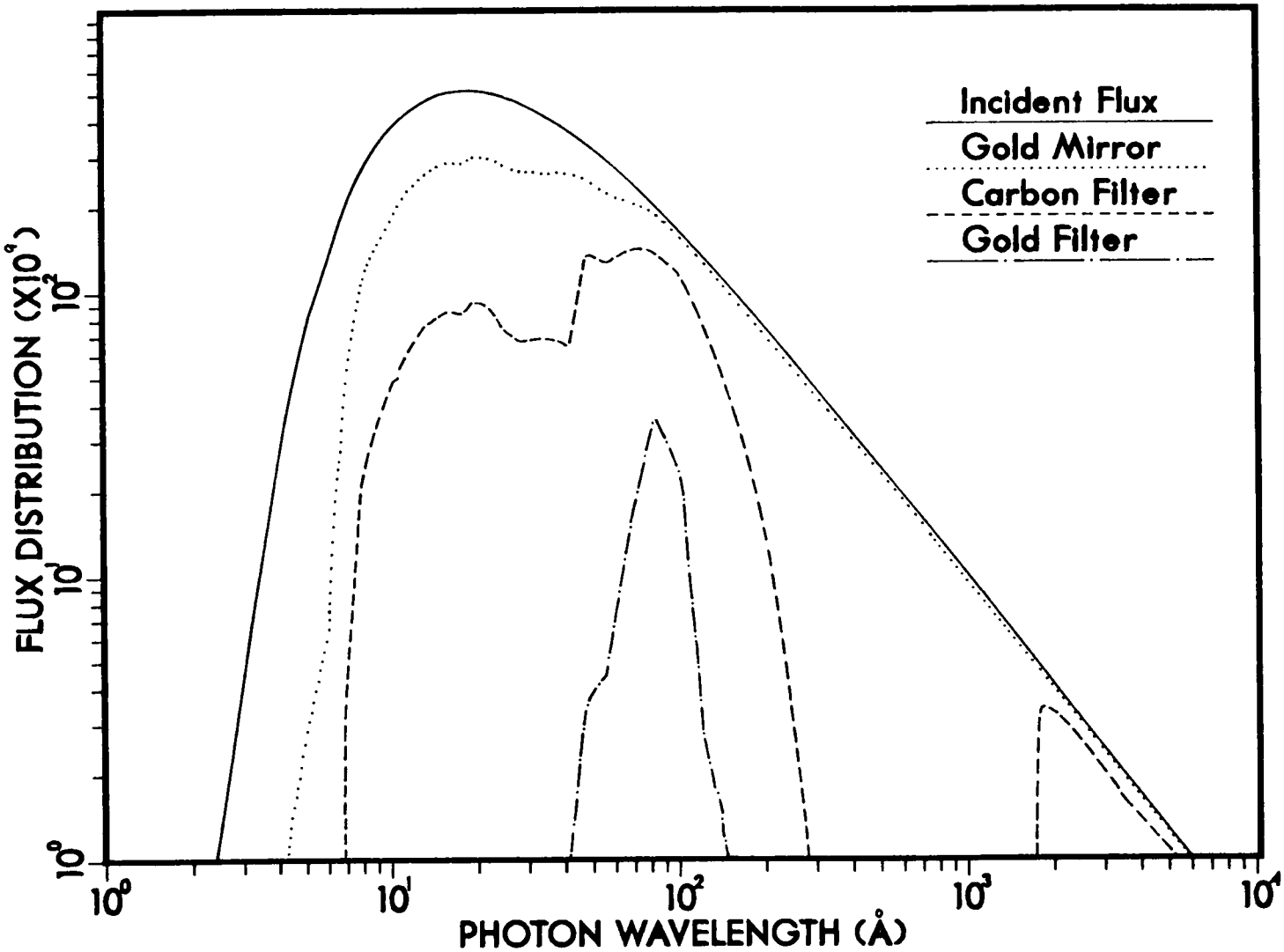

Fig.4-3
Flux distributions 2 at the BNL NSLS VUV ring. The light through a gold mirror with grazing angle of (1) 2 for carbon filter; (2) 7 for gold filter passes a filter of (1) 650 A carbon; (2) 650 A gold plus 650 A carbon.

configuration before the bending mirror was coated. The silver filter 1 is a mono-layer filter with a thickness of 500 Å; the silver filter 2 is 2000 Å thickness. From the curve of silver filter 2 we note the high energy segment is reduced by a factor of ten. In Fig. 4-3, the high energy end of the spectrum is extended by a factor of two when a gold coated mirror is used. The dashed curve is the flux following carbon filter of 650 Å thickness. An alternative way to obtain desirable band pass is to increase the grazing angle of the bending mirror. The curve labeled gold filter is the flux distribution after a multi-layer filter consisting of 650 Å carbon and 650 Å gold mounted behind mirror of 7° grazing angle. In this configulation a narrow band pass can be achieved.

The absolute flux incident on the sample can be calculated from the curves of Fig. 4-1 by multiplying the fluxes shown by the beam current and the number of mrad accepted by the beam line. The power load on the optical elements was calculated when beam line was calibrated at NBS SURF II, where the typical values for the spectra reported here would be 40 mA and 10 mrad, respectively. The total power received by the spectrometer was 1.15×10^{-5} watts per

milliamper of beam current in the SURF II ring. The incident power on the filter was 4.6×10^{-4} w/ma. The incident power on the sample with a silver filter having a thickness of 400 Å was 7.0×10^{-5} w/ma. With a beam current equal to 100 mA, a typical value for the SURF II, the power load on sample is equivalent to a 7 μA excitation current by a electron gun under 1 kV of acceleration voltage. Photon excitation thus allows a greatly reduced power load, which is important when probing fragile materials by photon excitation.

C. Photon Excitation

Examples of the different spectra that can be obtained with electron beam and photon excitation are provided in Fig. 4-4 which shows SXE spectra obtained from a cleaved surface of LiF. Curve (a) shows a spectrum excited by 600 eV electrons. The major peak at 54 eV is the K emission spectrum of metallic Li which accumulates on the surface as it is degraded by the electron beam. Other small peaks at 46.5 and 61 eV are valence band and exciton emission peaks associated with LiF [4.9]. They are

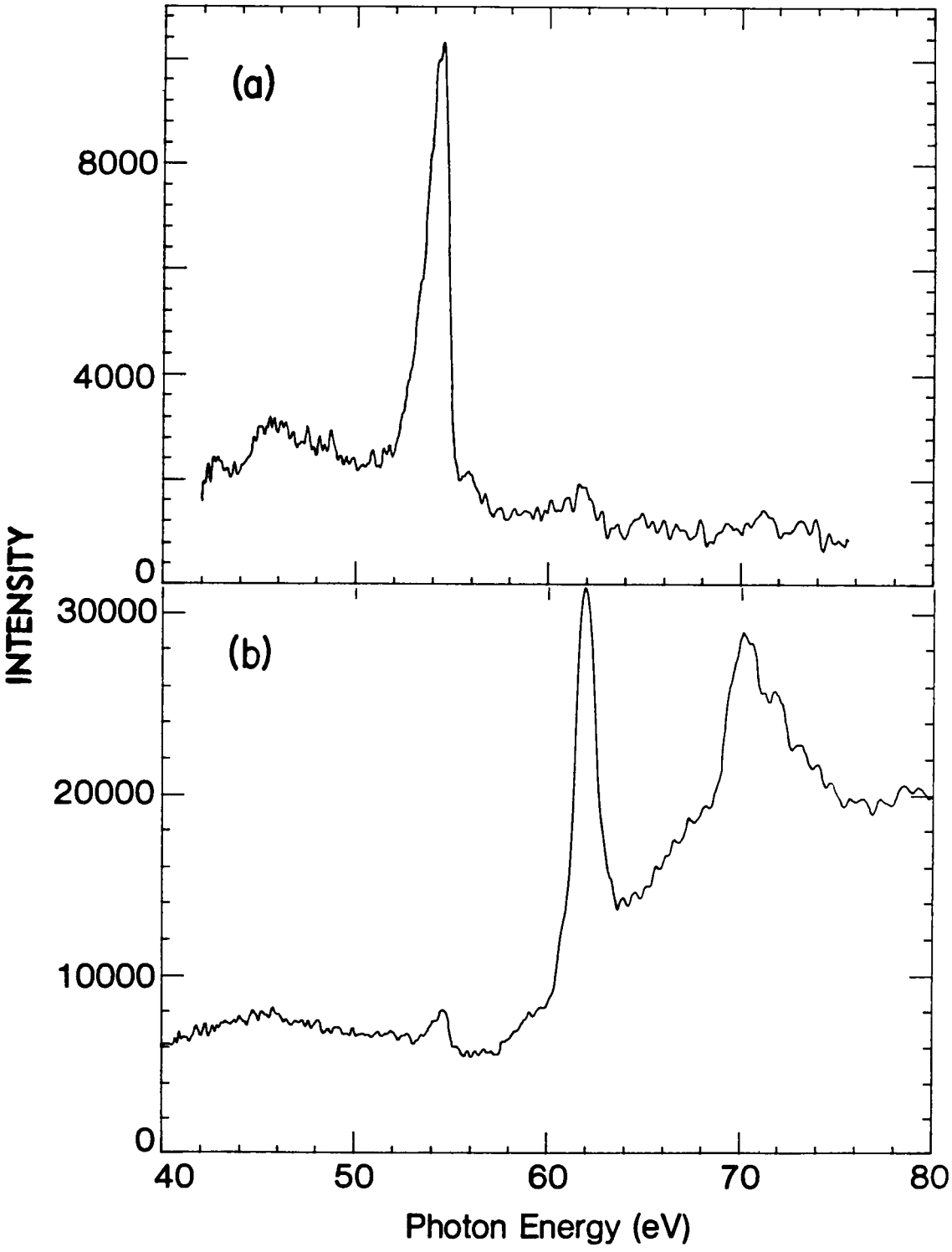

Fig.4-4
LiF spectrum obtained with (a) 600-eV e-beam excitation, and (b) photon excitation.

observed initially but disappear after brief exposure to the electron beam.

Curve (b) shows a spectrum excited by broadband photon excitation (curve N_1 of Fig. 4-4). The prominent peak at 61 eV is a peak associated with the core hole exciton, while peaks at higher energy result from core hole to conduction band transitions. A small Li metal emission peak is visible at 54 eV. Other workers have interpreted the peaks at 61 eV and above as true emission spectra [4.10]. We believe that part of the exciton peak intensity and the higher energy peaks result from scattered light and the modulation of reflectance by absorption, and that true emission occurs only in the exciton peak and at lower energies [4.11].

V. SXE SPECTRA OF DILUTE AL IN MG AND LIAL ALLOYS

A. Introduction

SXE spectra provide a measure of the partial density of states (PDOS) in a region localized near a selected constituent of the alloy. In these studies of Al-Mg alloys, the Al(Mg) $L_{2,3}$ spectrum results from transitions to the 2p core states so that the spectrum provides a measure of the (s+d)-PDOS in a region near the Al(Mg) atoms. Here K,L,M,... designate shells associated with the n=1,2,3,... principle quantum numbers, the subscripts indicate core levels of increasing binding energy, and the s,p,d,...designate the ℓ=0,1,2,... angular momentum quantum numbers. In LiAl, the Li K spectrum results from transitions to the 1s core states so that the spectrum reflects the p-PDOS in a region near the Li atoms. The Al $L_{2,3}$ spectrum provides a measure of the (s+d)-PDOS near the Al ions (see Sec. II A).

Two types of electron spectroscopy also provide information about the filled band states of the alloy. Photoemission spectroscopy (PES) provides a measure of the total DOS, without chemical, spatial, or angular momentum selectivity,

but with greater sensitivity to surface states, and with the possibility of obtaining additional band structure information from angular resolved measurements. Auger electron spectroscopy (AES), in which both electrons originate in the valence band (KVV or LVV spectra), is used for the chemical analysis of alloys, but DOS information is difficult to extract from the spectrum which is produced by a convolution over the initial states of both electrons[5.1].

Auger spectra in which one electron makes an L to K intercore transition and a second is excited from the valence band (KLV spectra) give information similar to SXE spectra in that they provide DOS information for electron states localized on one chemical species and some PDOS selectivity[5.2]. Our SXE spectra from dilute Al in Mg alloys will be compared to previous SXE spectra on richer alloys [5.3,5.4], and to KL_1V and $KL_{2,3}V$ Auger spectra[5.5,5.6].

Theories of the electronic states of alloys are intractable because of the mathematical difficulties imposed by disorder, though substantial progress has been made in recent years through the use of band structure calculations employing the coherent potential approximation[5.7-9]. The study of dilute alloys is of particular interest because it

permits comparison of experimental data on the dilute component with calculations made for single impurities in a host lattice. For metals, this problem has been discussed extensively using many body theory[5.2], static screening within the one electron approximation[5.9-11], and in terms of localized excitations[5.12,5.13]. Al in Mg has additional interest because it is an example of the Z+1 problem in which an impurity (Al) with one excess core charge is placed in a host lattice (Mg) with Z=2 charges per ion. Several authors have previously published SXE studies on another Z+1 system, Mg in Li[5.14,5.15]. In this paper we extend earlier studies of the Al-Mg system to the impurity limit, presenting data on 0.5%, 1.0% and 2.0% alloys.

As we have noted earlier, an important assumption, usually called the final state rule (FSR), is confirmed by both theory and experiment, and greatly simplifies the interpretation of SXE spectra. The FSR is derived from many body theory and indicates that the transition matrix elements may be accurately calculated using one electron band states if the one electron states used are calculated for the final state configuration of the system [5.2,5.16-18]. For SXE spectra, the final state of the transition is just the ground

state of the system so that ordinary ground state band structure wave functions may be used. A large body of experimental SXE data from metals also supports this assumption.

Another assumption, the equivalent core approximation (ECA), has sometimes been made in the interpretation of core spectra from various spectroscopies [5.2]. The ECA asserts that impurity ions carrying the same core charge should produce similar spectra. This idea is important in the present context because a high energy satellite of the Mg $L_{2,3}$ spectrum results from a radiative transition in an atom with a doubly ionized 2p core. Thus the final state of the SXE transition carries an excess core charge, so that this system is equivalent to an Al impurity within the ECA. A similar situation applies to the KLV Auger transitions, which leave an excess core charge in the final state and thus are equivalent to the Al impurity within the ECA. In this paper, we present new results for the dilute Al in Mg spectrum and for the Mg satellite spectrum and compare both to the KLV Auger spectra published by others [5.6]. The ECA is shown to have some value in identifying the added screening charge, but does not apply to the full spectra.

Experiment[5.4-6,5.14,5.15] and theory[5.10,5.11,5.19] have confirmed that when a Z+1 impurity is placed in a nearly free electron metal, the band width will be that of the host metal, but that there is a greatly enhanced s-PDOS near the bottom of the band associated with the static screening of the extra charge. We confirm this general characteristic for both the Al spectrum and the Mg satellite spectrum but find substantial differences in the detailed form of the spectra.

These concepts effectively resolve conflicting interpretations given in early studies of the K [5.4] and L [5.3,5.4] emission spectra of the Al-Mg Alloy system. The K spectra of Al and Mg were observed to be similar in width and shape and this was cited as evidence for a "rigid band" model, while the L spectra were substantially different in shape and were cited as support for a "two band" model. These differences are now resolved as follows. A common band is present to the extent that the bandwidths are nearly the same for Al and Mg, but the spectra sample local densities of states for each constituent that differ. The added charge of the Al ion is screened primarily by electrons of s-character, which add low energy structure to

the s-PDOS and to the Al L spectra. The screening charge does not contribute significantly to the p-PDOS, however, so that the K spectra are found to be very similar.

Several other characteristic features of SXE spectroscopy are relevant. Radiative yields are low so that emission spectra are weak, especially for the minor component of dilute alloys [5.20]. The data here were taken with a new spectrometer whose greatly improved measuring efficiency makes the measurement of 1.0% alloys and of satellite spectra routine [5.21]. The SXE spectra of metals have a low energy tailing, resulting from the presence of Auger assisted radiative transitions [5.22], which make it difficult to determine precisely the position of the lower edge of the DOS. Additional tailing may result from plasmon satellites and clustering effects in alloys [5.23,5.24]. Finally, the hole excitation and escape depths for SXE spectroscopy are usually such that it is primarily a bulk rather than a surface probe.

Though our new spectrometer efficiently acquires data for very weak spectra, great care is still required to extract accurate data on very dilute systems. Long integrations of weak spectra integrate not only the wanted

signal but also the background consisting of Bremstrahlung and scattered light, which must be subtracted from the spectra. Small errors in the calibration of the detector system, which have negligible effect on strong spectra, may appear as spurious structure in weak spectra. Self absorption effects must be carefully considered. In the present case, the SXE spectrum of Al lies in the absorption band of the host metal Mg. In the present system also, there is some overlap in the Al impurity spectra and the Mg satellite spectra, so that careful consideration has been given to separation of the two. Consequently, these subtraction procedures are described in the following section.

The phase diagram for concentrated alloys often shows two-phase regions which make comparison with theory difficult. For LiAl, consisting of equal proportions of Al and Li, only the β-phase exists and it forms an intermetallic compound [5.36]. This alloy has the Zintl-structure (B32 structure) [5.37]. For simplicity, it can be thought of in terms of superstructures on the bcc lattice. For an atom at the center of the cube, there are four like nearest neighbors located on four corners of the cube in a diamond-

type sublattice, and four unlike atoms occupying the remaining corners in another sublattice. The resulting tetrahedral bonding is very unusual in a metal alloy system, and gives the system special theoretical interest.

In this work, we report the measurement of the Li K emission and Al $L_{2,3}$ emission spectra for LiAl samples provided by I.Curelaru of the University of Utah. We found extreme sensitivity of the spectral features for both Al $L_{2,3}$ and Li K emission to the presence of excess Li on the surfaces. The major problem is that Li diffuses rather rapidly to the surface and is partially oxidized there. Fortunately, this surface layer can be removed or reduced to an acceptable level by the exciting e beam.

Theoretical calculations on LiAl with equal proportions of Al and Li have been published by Asada et al. using the linear muffin-tin-orbital (LMTO) method[5.39]; by Zunger [5.40] and by Hafner et al [5.38] using the linear-combination-of-atomic-orbitals (LCAO) method; and by Ellis et al. using a molecular cluster method with nine atoms[5.41]. Our measurements of Al $L_{2,3}$ and Li K emission spectra for LiAl will be compared with calculated (s+d)-DOS of Al and p-DOS of Li by Asada et al.[5.39]

B. Experimental Procedures

The SXE spectrometer used in these studies is a 5 m Rowland circle design with large toroidal gratings and a microchannel-plate (MCP) enhanced CCD Si-diode array readout. Using a 600 ℓ/mm grating and 100 μm slits, the theoretical resolution is better than 0.2 eV to photon energies of 90 eV. The instrument is used as a display type instrument with about 10 Å of the spectrum being immaged by the CCD readout at each position of the detector. Very wide spectra such as those reported here are assembled from spectral slices taken at 10 Å intervals. A detailed description of the instrument has been given in Sec. III. Measurements were made in an ion pumped UHV chamber at a pressure of about 1×10^{-8} torr. Spectra were excited with a 0.2 mA beam of 2 kV electrons imaged in a 1 mm spot on a sample placed 3 or 4 mm away from the entrance slit of the spectrometer.

For the measurements of dilute Al in Mg alloys, five samples (Al, Mg, 0.5%, 1.0%, 2.0% Al in Mg) were mounted and measured at the same time under identical conditions. Excitation and emission angles were 48° and 30° from the sample normal

respectively. The use of identical excitation conditions greatly facilitated the subtraction of background effects and the separation of the weak Al and Mg satellite spectra as described below.

In the experiments reported below, the total spectrum from 155 Å to 325 Å was taken in 17 minutes in 17 segments. The partial spectrum in the impurity region from 165 Å to 195 Å was then recorded in 3 segments with six 5 min exposures of each segment (30 min per segment, 90 minutes total exposure). For each spectrum, a background consisting of detector and readout noise was subtracted before the raw data was multiplied by a transmission factor to account for non-linearities in the detector system. For these measurements, no correction has been made for the grating efficiency as a function of wavelength. As a result, quantitative comparisons of spectral intensities at widely separated wavelengths cannot be accurately made.

Spectra are recorded on a detector surface oriented tangent (or within a few degrees of the tangent) to the Rowland circle [5.21]. When corrected for a "plate factor" similar to that required in the photographic recording of data[5.25], the recorded spectra provide a direct measure of

the wavelength dependent spectral intensity $I(\lambda)$, since grating instruments have constant wavelength resolution. These spectra may be converted to energy dependent intensity spectra I(E) by dividing the spectra by E^2. All spectra in this chapter are presented as a function of photon energy and have been divided by E^2. Since the dipole matrix elements governing optical transitions contain a factor of frequency cubed, it is sometimes useful to devide the spectral intensities by an additional factor of E^3 before comparisons are made to calculated densities of states.

In Figure 5-1, the spectrum of a 1.0% Al in Mg alloy is plotted. The $L_{2,3}$ spectrum from the Mg host is visible below 50 eV. The inset spectrum shows $L_{2,3}$ spectrum from 1.0% Al and the Mg satellite spectrum after a thirty times longer integration of signal on the detector. The satellite spectrum extends to 64 eV and the Al impurity spectrum to about 72 eV. As we shall see below, there is some overlap between the Al spectrum and the Mg satellite spectrum that must be separated in order to get an accurate measurement of either spectrum.

For intense spectra which greatly exceed the background, backgrounds may often be subtracted using a

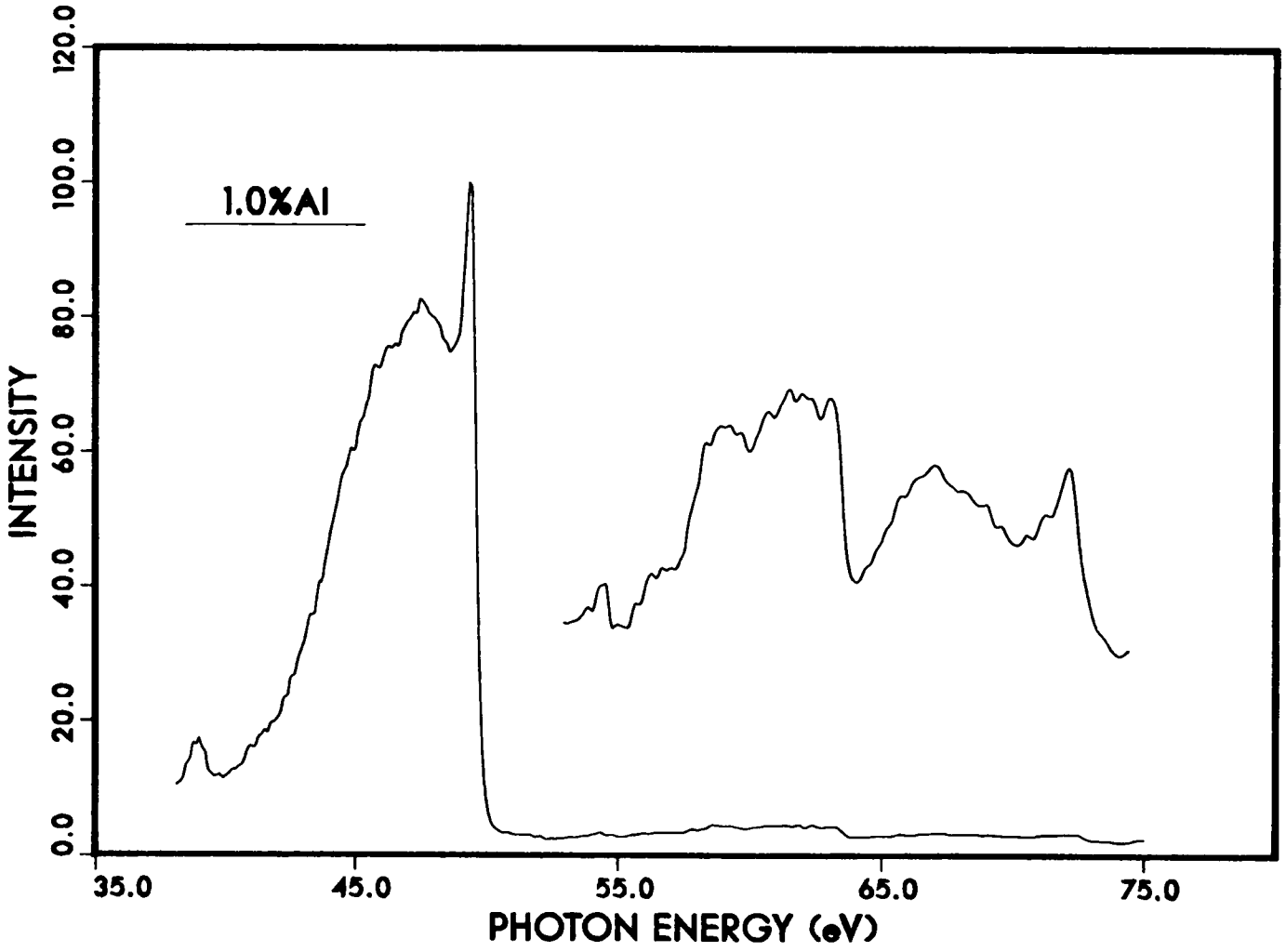

Fig.5-1
The SXE spectrum of 1.0% Al in Mg alloy. Major features are the Mg $L_{2,3}$ spectrum (42-50 eV), the Mg L double ionization satellite (56-64 eV), and the Al $L_{2,3}$ impurity spectrum (64-73 eV).

straight line fit to the baseline on either side of the spectrum. More careful procedures must be used in the present case where structures comparable in magnitude to the background signal must be analysed. Figure 5-2 shows the Al impurity spectra and the Mg L-satellite for pure Mg and the three alloy samples with Al content of 0.5%, 1.0% and 2.0%. The spectra were taken under conditions of excitation and orientation that were as nearly identical as possible. The spectra are normalized to the peak height of the primary Mg spectrum to account for minor differences in sample position and excitation current. Assuming that the background contributions from the Mg in the dilute alloys was the same as for the pure Mg, the background and satellite spectrum of the pure Mg was subtracted from the alloy samples after appropriate normalization of the satellite to the primary spectra.

After subtraction, the spectra of 0.5%, 1.0%, and 2.0% Al in Mg were obtained as shown in Figure 5-3. The intensity increases linearly with impurity concentration as expected. A low energy tail that extends below the Mg satellite spectrum is observed that we believe to be real. It is discussed further below. An increase in residual

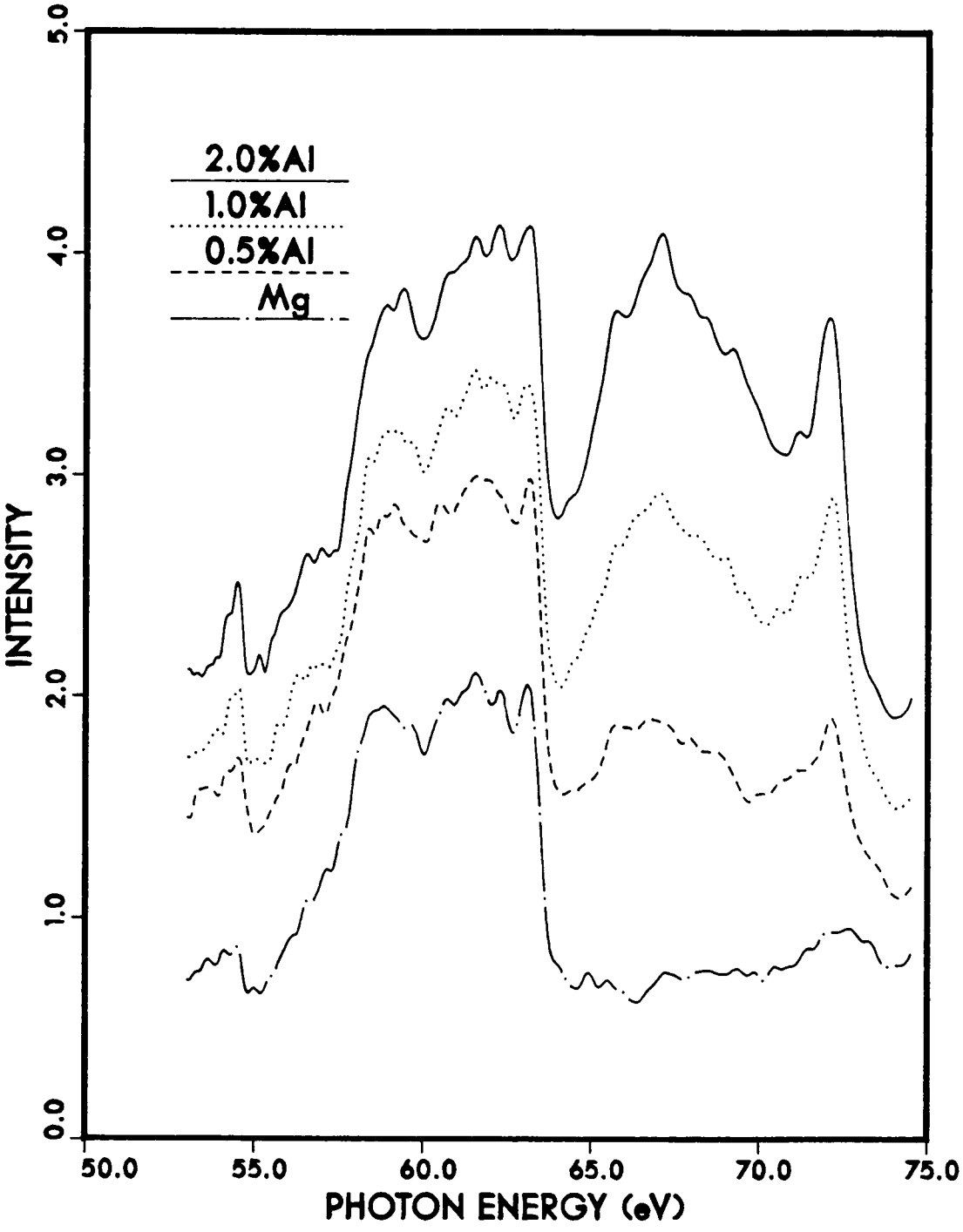

Fig.5-2
The Mg L-satellite and Al $L_{2,3}$ spectra for Mg and 0.5%,1.0% and 2.0% Al in Mg alloys.

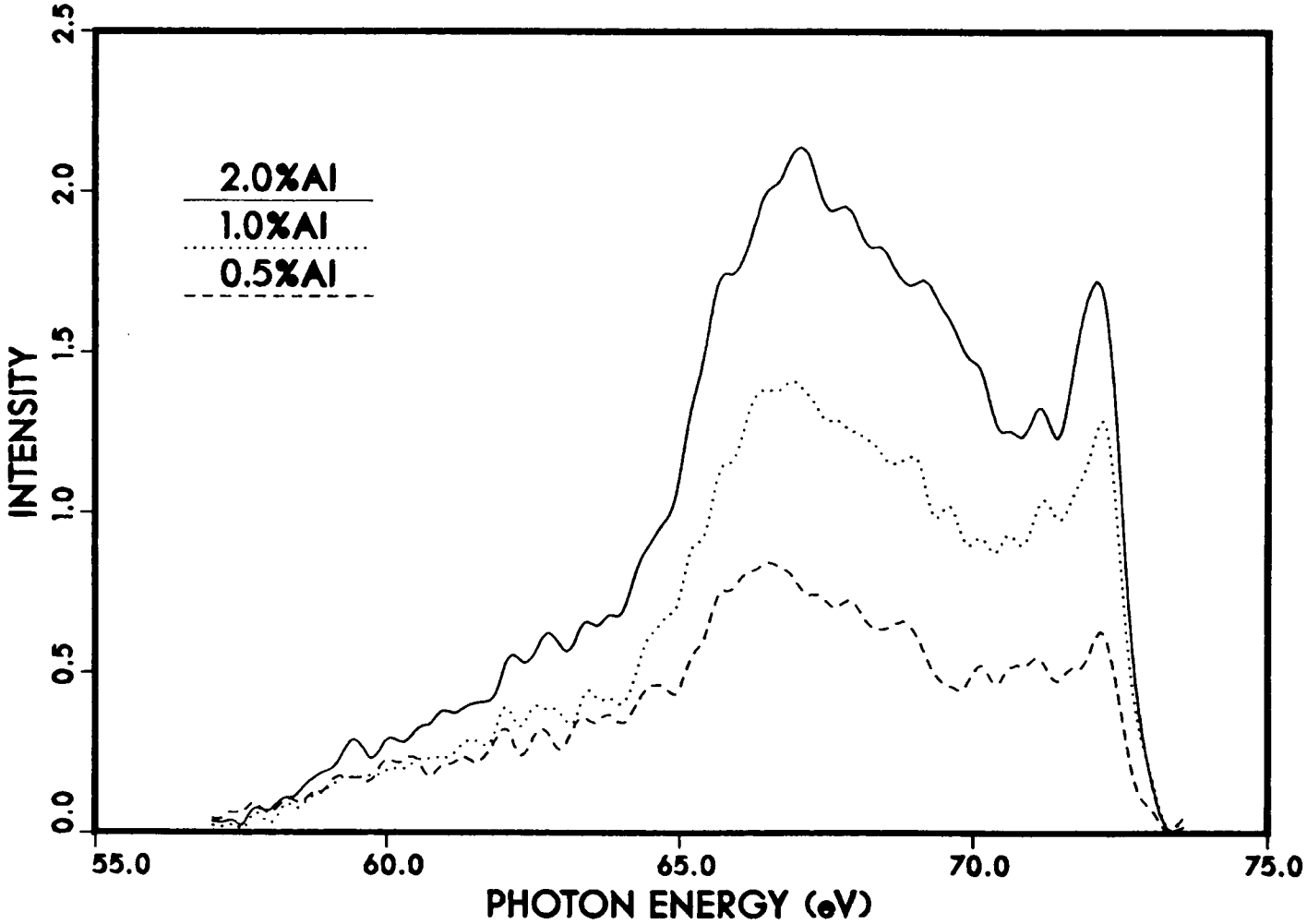

Fig.5-3
The Al $L_{2,3}$ impurity spectra for Al in Mg alloys after subraction of the Mg satellite spectrum.

background with Al content, in excess of that obtained with pure Mg, is also observed that may be attributed to the Al component of the alloy.

Since both the Mg satellite and the Al spectrum lie in the Mg $L_{2,3}$ absorption band, the spectral intensity should be corrected for self absorption by Mg. A simple one dimensional model may be used for this correction in which the external measured intensity spectrum I is related to the internal excited intensity spectrum I_0 by the expression

$$I(\lambda) \propto \int_0^\infty I_0(\lambda) \exp[-\mu(\lambda)\, x/\cos\theta_0]\, F_{exc}(x/\cos\theta_i, E)\, dx$$

where $F_{exc}(x/\cos\theta_i, E)$ is the probability of excitation of an atom at a depth x below the surface by an electron incident with energy E and angle θ_i, and $\mu(\lambda)$ is the absorption coefficient for x-rays exiting at an angle θ_i. $x/\cos\theta_i$ and $x/\cos\theta_0$ are just the path lengths of the exciting electrons and exiting x-rays for a depth x below the surface. In the present case where the Mg satellite and Al spectra lie in a spectral region of strong Mg absorption, the escape depth for soft x-rays, which may be calculated from the absorption coefficient for Mg[5.26] is substantially smaller than the excitation depth for 2 kV incident electrons, which

may be calculated from the stopping power of electrons in Mg and the inverse mean free path for the excitation of 2p core holes[5.27,5.28]. The excitation probability with depth is approximately constant until the incident electron's energy is reduced to a few hundred eV at a depth of about 900 Å. Under these conditions, which do not apply to the primary Mg spectrum for which the absorption is small, the internal excitation spectrum may be determined from the external measured spectrum using the very simple relation $I_0(\lambda) \propto \mu I(\lambda)$. This correction has been made to the impurity spectra in Figure 5-3 using absorption coefficients μ for Mg taken from the literature [5.26].

In order to obtain reproducible emission spectra of K for Li and $L_{2,3}$ for Al we have measured serveral samples with a variety of preparation conditions. Experimental evidence shows exposure of the sample in air for three hours results in visible peaks of metallic Li and metallic Al. A sample that was exposed to air for several minutes before mounting in the chamber can be processed to show a LiAl spectrum in two stages using the excitation e beam. For these experiments, 2 KeV electrons were used in a 1 mm spot at beam currents between 50 μA and 200 μA.

C. Results and Discussion

Dilute Al in Mg Alloy. The $L_{2,3}$ spectra of a 1.0% alloy is shown in Figure 5-1. The primary and satellite Mg spectra of the other samples studied (0.5% and 2.0% alloys) are not measurably different than those shown here. The primary Mg spectrum has been discussed by several earlier authors[5.29]. The threshold peak is a mixture of band structure effects and the threshold anomaly of the Mahan, Nozieres, deDominicis (MND) many body theory characterised by a threshold exponent (see Sec. II A and Refs. 5.30, 5.31).

The lower peak in the primary spectrum centered at 47.5 eV is a feature of the s-PDOS of Mg. Below 45 eV, the intensity of the primary spectrum rapidly decreases consistent with the theoretical bandwith of 7.1 eV for Mg [5.32].

The spectra of the Mg satellite for pure Mg and for the alloy samples are shown in Figure 5-2. The edge threshold is located at 63.5 ± 0.1 eV and lies 14.0 ± 0.1 eV above the parent band edge at 49.5 eV. This may be compared to the previous separation of 13.6 eV cited by Hanson and Arakawa using data with much poorer resolution [5.33]. The

apparent small differences in shape for the satellite spectra as a function of Al impurity content are believed to be produced by the tails of the Al spectra which extend below the satellites. These tails are clearly seen in Fig. 5-3 after the satellite spectrum is subtracted away. Three peaks are resolved in the satellite spectrum: a threshold peak at 63.2 eV; a broad central hump at 61.6 eV; and a low energy hump at 58.8 eV. The central hump in this spectrum was not resolved in earlier studies [5.33]. In Figure 5-4, the Mg satellite and primary peaks are compared by aligning their thresholds. The spectra were shifted by 13.99 eV to bring their edges into coincidence. Clearly the threshold peak and central hump of the satellite coincide with the threshold peak and secondary maximum visible in the parent spectrum. The low energy peak of the satellite has no counterpart in the parent spectrum and is a structure that can be unambiguously identified with the presence of a hole in the final state of the system. We interpret this to be simply the screening enhancement expected for an additional core hole.

It is also clear from Figure 5-4 (see also Fig. 5-6) that the threshold peak of the satellite spectrum is not as

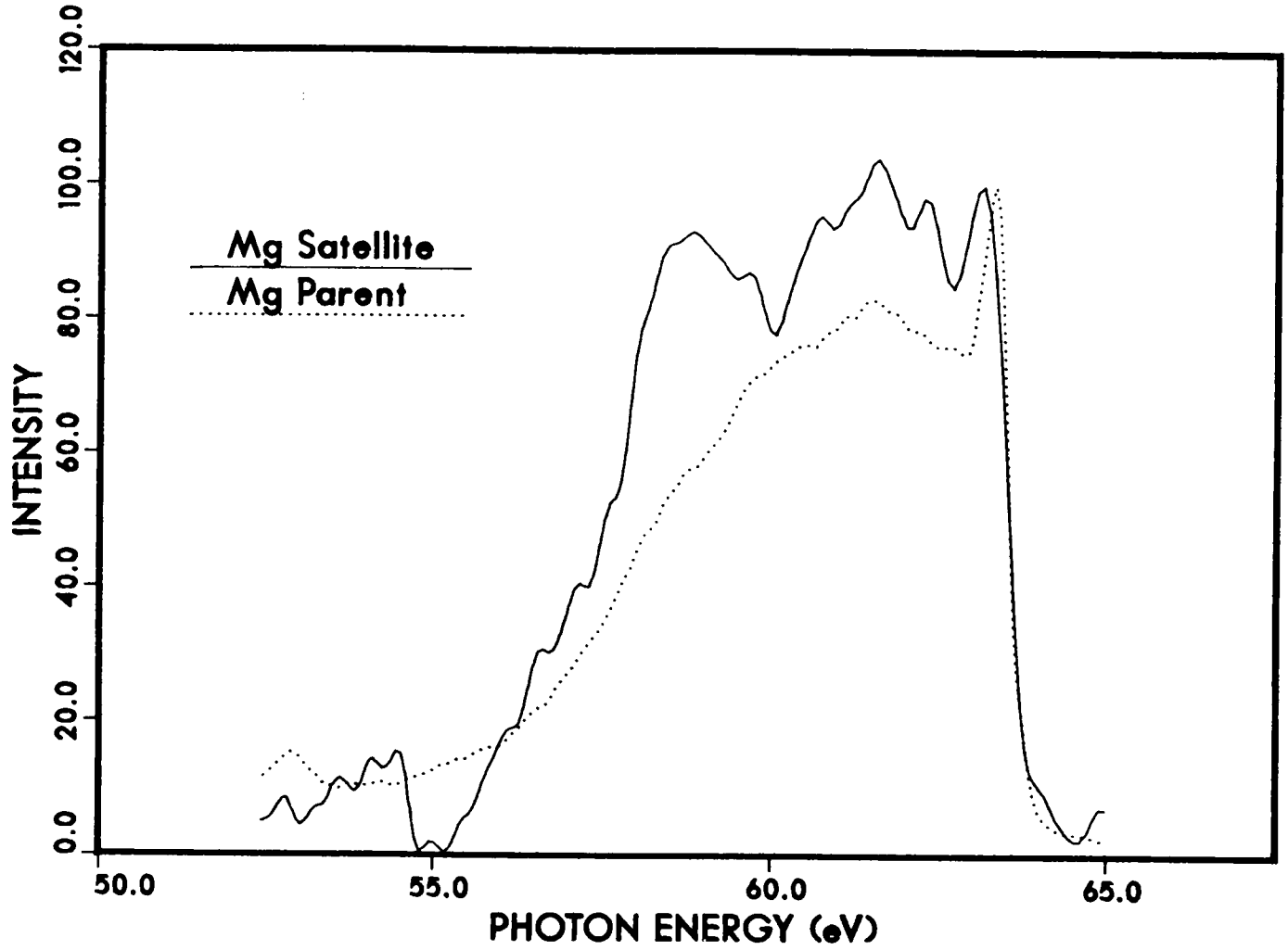

Fig.5-4
The Mg satellite spectrum compared to the primary Mg $L_{2,3}$ spectrum. The spectra have been shifted by 13.99 eV to bring the edges into coincidence.

sharp as that of the primary spectrum. This may constitute support for the calculations of Almbladh and von Barth which suggest that the exponent for the MND threshold anomaly should be smaller in the satellite than in the primary spectrum [5.2]. The determination of the threshold anomaly exponent is difficult because of the presence of the bandstructure peak at the threshold. Neddermeyer, from data virtually identical to ours, determined a value for the primary peak of 0.3 ± 0.07 [5.29]. We estimate the threshold anomaly for the satellite to be 0.16 ± 0.08 assuming a similar contribution of the DOS to both the primary and satellite spectrum.

A very weak structure is seen in the position of the Al impurity spectrum even in the pure Mg sample. Its intensity is about 10% of that of the Mg satellite. The satellite is believed to represent decay from a state with two holes in the core ($2p^2$). This configuration contains three LS coupling configuration terms, $^3P_{2,1,0}$, $^1D_2$, and $^1S_0$. Even though quantum weighting arguments would suggest that the ^1D state is produced with 5/9 the probability of the ^3P states in the excitation process, this state is believed to decay non-radiatively to the ^3P state prior to radiative

decay. Thus the major satellite is believed to result from decay of the ^3P state[5.34]. The weaker high energy structure that we observe may result from the radiative decay of the previously unobserved $^1S_0$ state. Its energy separation from the $^3P_2$ satellite is consistent with calculations of the separation of these states in free ions[5.35], and its relative magnitude is consistent with the relative degeneracies of the ^3P and ^1S states (Sec.II A and Table 2-1).

We report for the first time observation of the L_3-L_1 intercore transition for the satellite spectrum at 54.5 ± 0.1 eV. A careful comparison of the shape of this peak to the L_1-L_3 intercore transition of the primary spectrum at 39 eV shows some apparent differences in shape, but noise in the data makes further analysis difficult. There is a clear difference in the energy separation between the Fermi edge of the primary spectrum and its associated intercore transition (10.7 eV) from the energy separation of the Fermi edge of the satellite and its intercore transition (9.0 eV). This difference may be of value for testing calculations of chemical shifts of electronic core states in alloys.

The impurity spectra for Al are shown in Figure 5-3. The spectra increase linearly in intensity with the Al content,

as do the sloping low energy tails of the spectra and the scattering background. The scattering background has been subtracted in Figure 5-3. In Figure 5-5, the Al impurity spectrum is compared to the spectra of pure Al and Mg metals, with the spectra being aligned at their fermi thresholds. It can be seen from Figure 5-5 that the sloping tails of the alloy spectra extend to the full width of the pure Al spectrum. In addition to the processes producing tailing in all metal spectra, the effects of clustering may enhance the tails for these alloy spectra. Except for the tails, the Al impurity spectra are narrowed to nearly the width of the Mg $L_{2,3}$ spectrum. The observed width of about 8.0 eV remains about one volt wider than either the primary or satellite Mg L spectra (See also Fig. 5-7).

A threshold peak is visible in the Al impurity spectra. In Figure 5-6, the impurity spectrum in the threshold region is compared with the threshold region of both pure Al and pure Mg. The Al spectra are plotted on a true photon energy scale and the Mg spectrum has been shifted by 23.02 eV so that its threshold is aligned with those of the Al alloy spectra. Both the edge width and threshold peak are slightly broader in the impurity spectrum than in the pure Al spectrum

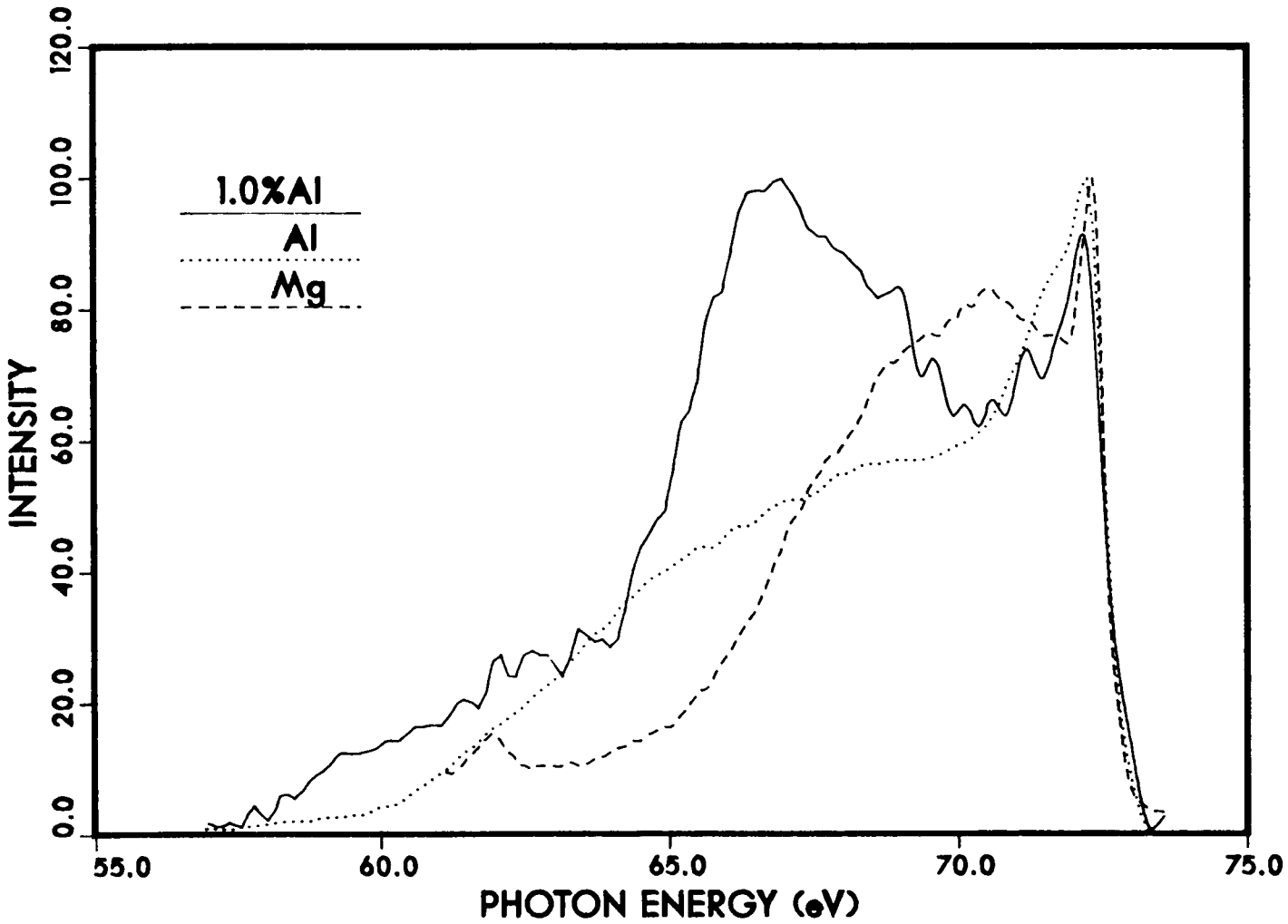

Fig.5-5
The Al impurity spectrum for the 1.0% alloy compared to the $L_{2,3}$ spectra of pure Al and Mg. The Mg spectrum has been shifted by 23.02 eV and the prue Al spectrum by -0.18 eV to bring them into coincidence with the edge of the impurity spectrum.

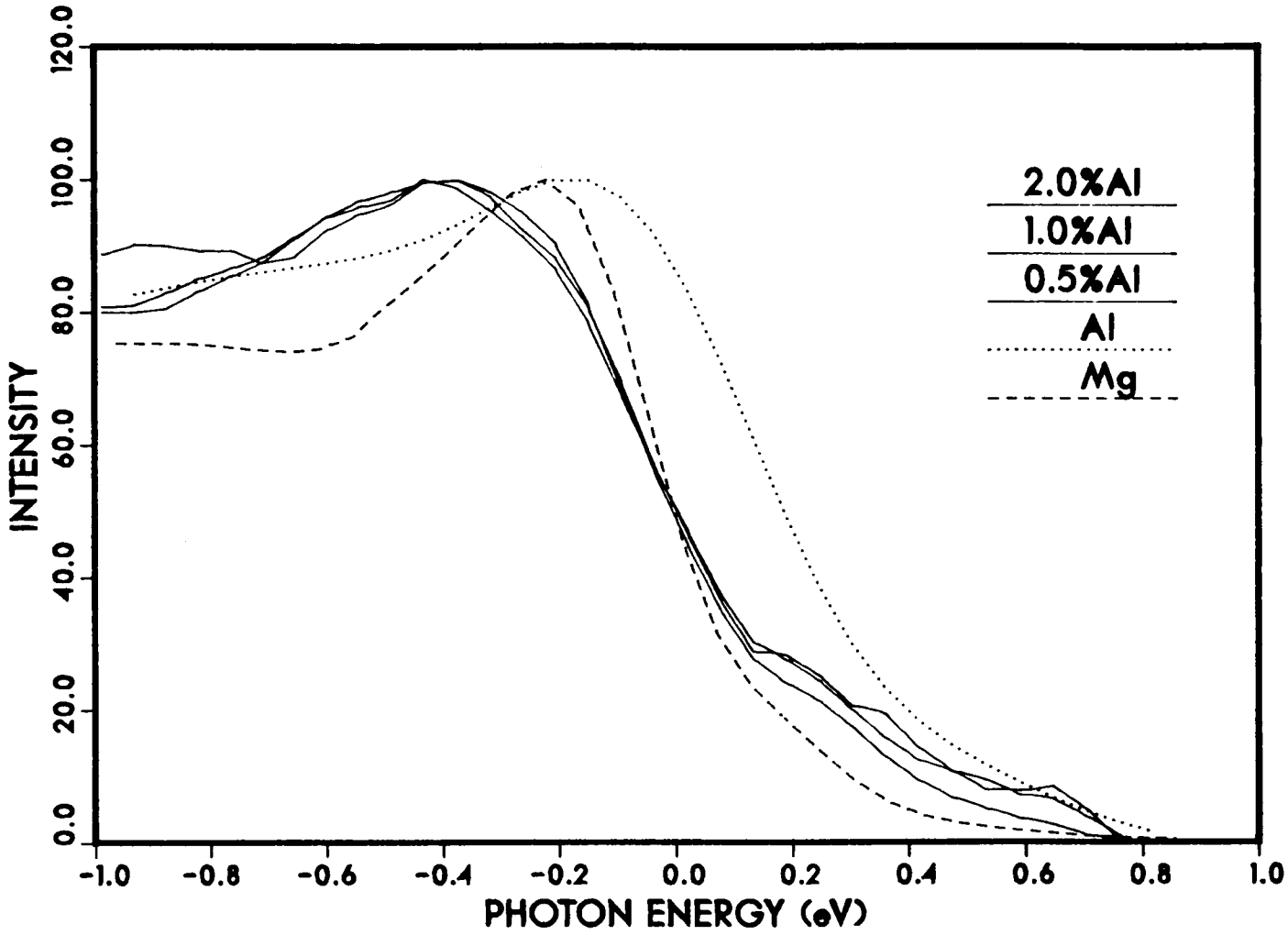

Fig.5-6
The threshold region of the Al impurity spectrum compared to pure Al and Mg. The zero of the energy scale is at 72.57 eV. The Mg spectrum has been shifted by 23.02 eV.

and much broader than in the Mg spectrum. The added width may be the result of added disorder near the Al site. The edge shape, though slightly broader, is clearly a better match to the Al than to the Mg edge. Below the threshold peak, the Al impurity spectrum clearly does not match the Mg spectrum, and in particular does not show any evidence of the maximum in the Mg PDOS located about 2 eV below the spectral threshold.

Figure 5-6 also shows a 0.18 eV shift of the fermi edge of the Al spectrum from pure Al to the alloy. This shift may be attributed to a "chemical" shift of the core level due to the change of the charge environment at the Al ion core.

In Figure 5-7, the Al impurity spectrum, the Mg satellite spectrum, and the Auger KLV spectrum from Lasser and Fuggle[5.2] are compared. Each of these spectra are believed to be derived primarily from the s-PDOS of an ion core in Mg with an excess positive charge in the final state. Within the equivalent core approximation, they would each be expected to have approximately the same shape. Each is observed to have a prominant low energy peak associated with the screening charge. Otherwise, the spectra show substantial differences. The Al impurity spectrum and the

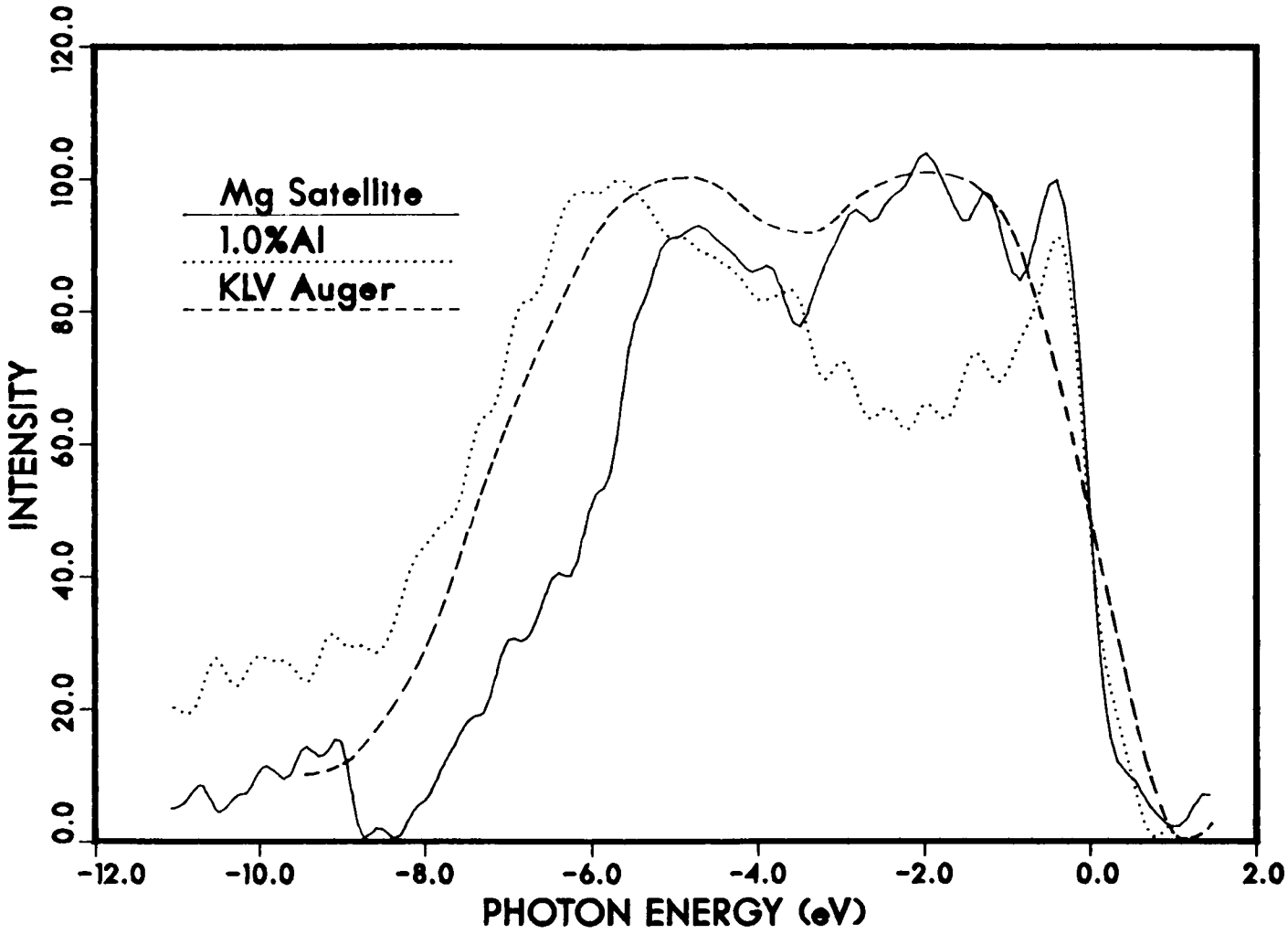

Fig.5-7
The Mg L satellite, the 1.0% Al $L_{2,3}$, and the KLV Auger spectra compared. Auger spectrum taken from [5.2].

Auger spectrum are about 1 eV wider than the satellite spectrum, though in the case of the Auger spectrum this may be partly due to lower resolution in the measurement and to the measurement of richer alloys. The central peak in the Mg satellite spectrum coincides with structure in the Auger spectrum, but has no counterpart in the Al impurity spectrum. We have previously shown in Fig. 5-4 that it corresponds to a band structure feature in the primary Mg L spectrum. Clearly, a more sophisticated approach than the ECA is required for the interpretation of SXE and other core level spectra.

We may summarize the major conclusions of dilute Al in Mg as follows:

1) The Mg L satellite spectrum and the $L_{2,3}$ spectrum of dilute Al in Mg have been observed with unprecedented resolution.

2) Both the satellite and Al impurity spectra exhibit a low energy peak in the s-PDOS that is associated with the screening of an extra charge in the ion core.

3) Except for the low energy "screening" peak, the spectra of the satellite and of dilute Al in Mg show dissimilar structures associated with local densities of states specific to each. Hence the ECA does not give an adequate

description of the data.

4) The threshold peak in the Al impurity spectrum resembles that of the pure Al spectrum rather than that of the Mg host, though both the edge and peak show some additional broadening. Other features of the Mg $L_{2,3}$ spectrum are also not observed in the Al impurity spectrum.

5) The threshold peak in the Mg satellite spectrum is not as sharp as in the primary Mg spectrum, a result of possible interest to MND theory.

6) A "chemical" shift of the core levels can be seen in the displacement of the Al fermi threshold by 0.18 eV between pure Al and dilute Al in Mg.

7) The L_3-L_1 intercore transition associated with double ionized Mg 2p levels has been observed for the first time. Its 9.0 eV separation from the Fermi edge of the Mg satellite spectrum is observed to be substantially smaller than the 10.7 eV separation observed for the primary Mg spectrum.

8) A very weak, second satellite peak has been observed that may result from radiative transitions from a $^1S_0$ state of the doubly ionized core.

LiAl Alloy. In Fig. 5.8, we display the emission spectrum from LiAl sample. In Fig. 5-9, the Li K spectrum for LiAl versus photon energy and the calculated p-PDOS by Asada et al.[5.39] are plotted. The Fermi level position is 54.7 eV ± 0.1 eV, taken at the half maximum of the upper edge of the spectum. Fig. 5-10 shows the Al $L_{2,3}$ spectrum for LiAl alloy together with (s+d)-PDOS calculated by the same authors.

The 10%∽90% broadening on the upper edge of Li K emission spectrum in Fig. 5-9 is about 0.8 eV which combines the effects of instrumental broadening, core-hole lifetime broadening, and thermal broadening of both the fermi edge and the core level. (For gaussian broadening of a square edge, the FWHM of the broadening function is given by the 12%∽88% width, and the gaussian factor α in $\exp(-\alpha E^2)$ is given by α = 1/2(8%-92% width) so that the 10%∽90% value is a good rule of thumb to quote.) Thermal broadening of the core level is the dominant physical effect in light metals, but it would not be greater than 0.2 or 0.3 eV [5.42]. Our instrumental resolution is about 0.1 eV. This excess broadening in the data might provide added evidence for disorder in the samples since it would be evidence for

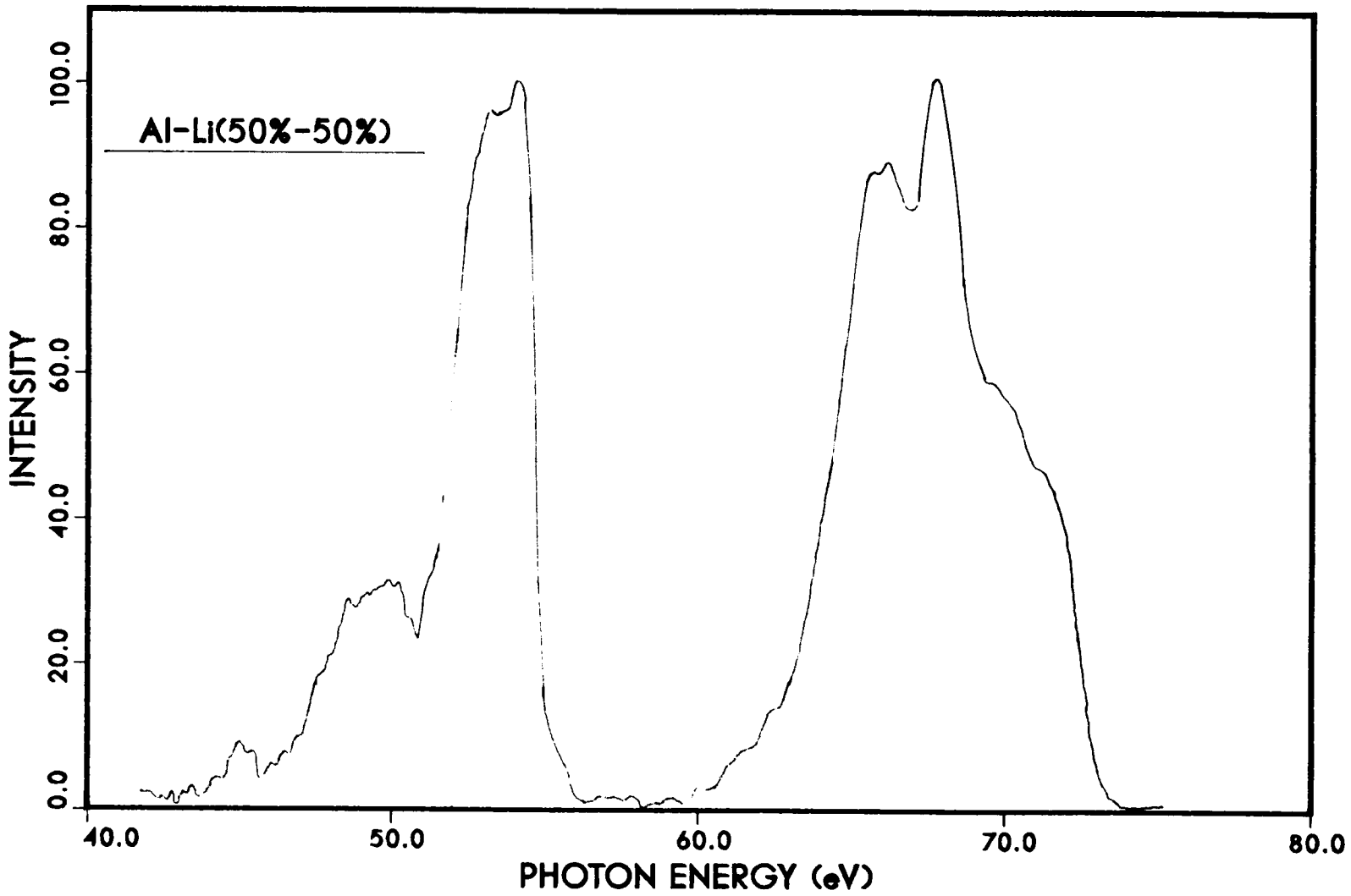

Fig.5-8
The total SXE spectrum from LiAl (50%-50%). Peaks at 67.6 ev for Al $L_{2,3}$, 54.1 eV for Li K spectra.

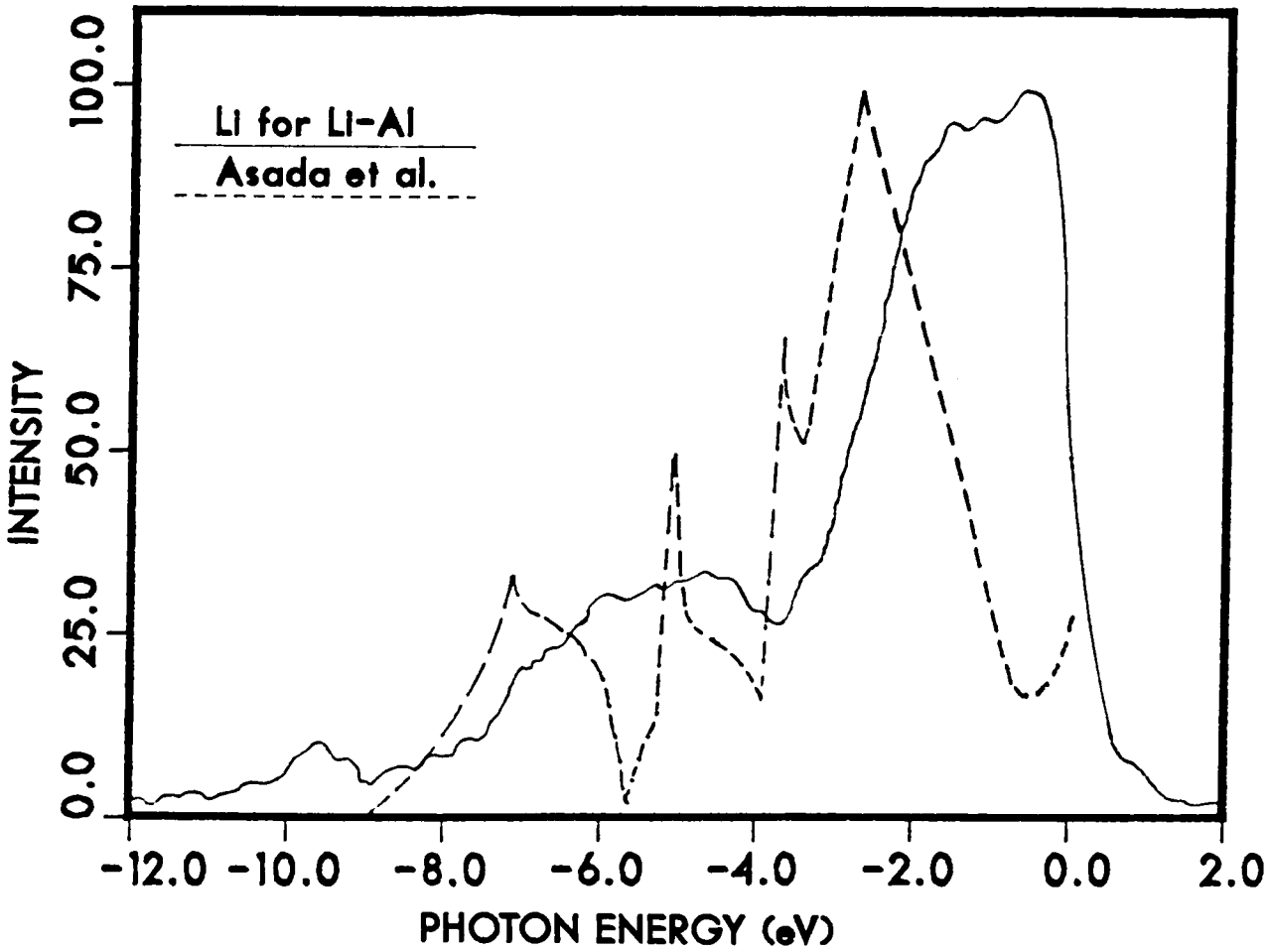

Fig.5-9
The Li K spectrum for LiAl (50%-50%) and the calculated p-PDOS of Li in LiAl taken from [5.39].

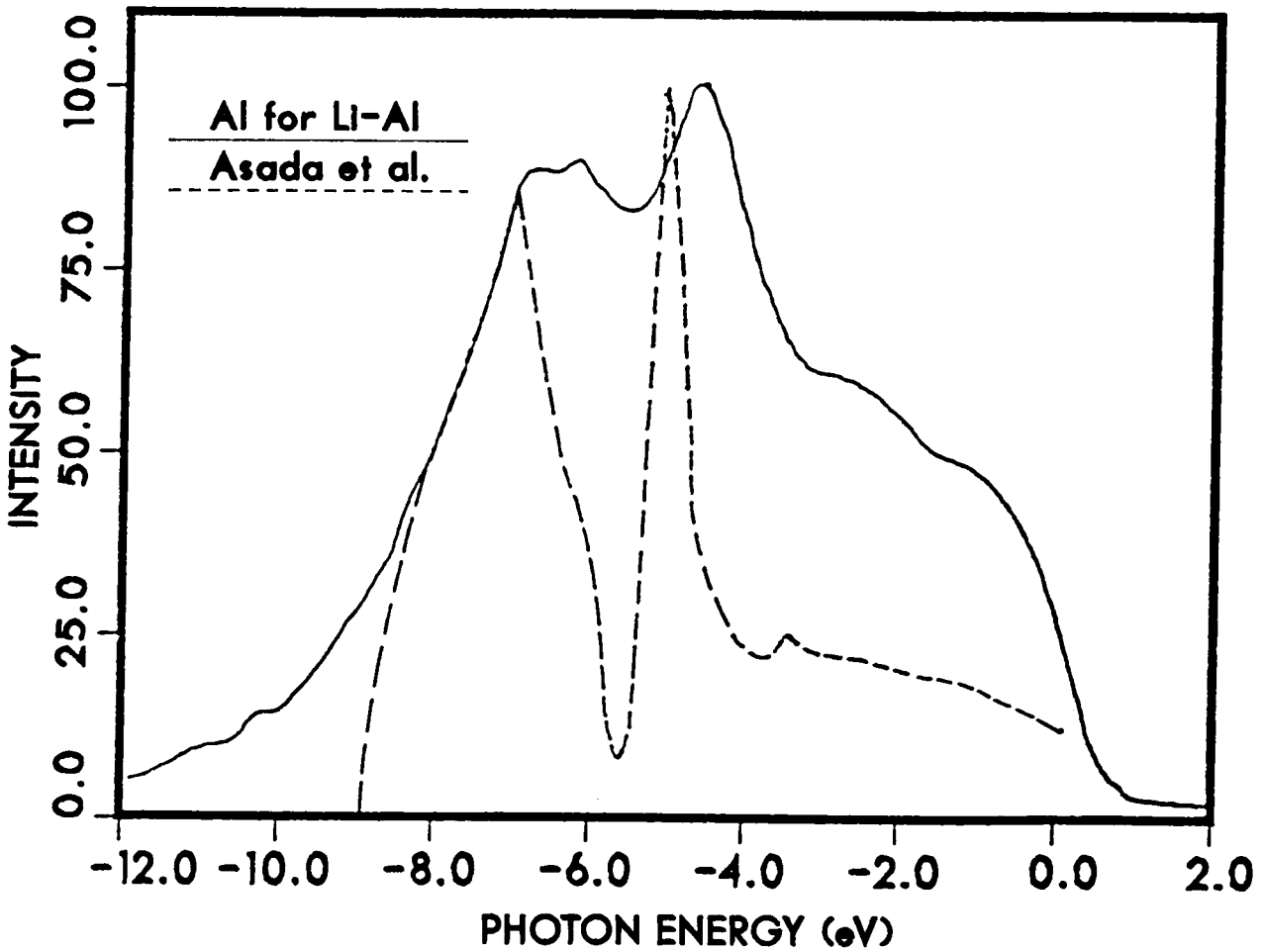

Fig.5-10
The Al $L_{2,3}$ spectrum for LiAl (50%-50%) and the calculated (s+d)-PDOS of Al in LiAl taken from [5.39].

smearing of the core level energy by chemical shifts resutling from different local environments of the atoms.

The Al spectrum of Fig. 5-10 may be compared with the s+d partial density of states (PDOS) of Al in LiAl calculated by Asada et al. [5.39]. The match is good but not perfect. The two major peaks in the calculated PDOS are centered at -5.0 eV and -7.0 Ev, while the experimental peaks are centered at 4.8 eV and -6.7 eV. Thus the calculated values lie some 4% to 5% deeper than the experimental values. We do not believe that the doubling in the lowest peak in the experimental spectrum is real, because it was not reproduced in other spectra taken. The broad hump centered at -2.5 eV does seem to be real but does not match any feature in the (s+d)-PDOS. It does coincide with a prominent peak in the p-PDOS,however. Its presence may suggest a breakdown of the selection rules, which would not be too surprising in a system with considerable disorder.

The overall width of the spectrum cannot be determined with any accuracy due to the usual low energy tailing that is typical of SXE spectra. By fitting a function of form $(E-E_0)^{1/2}$ to the spectrum in the region below the -6.7 eV peak. It would be estimated that the spectral width is

about 9 eV.

From Fig. 5-9 we notice the fit between the PDOS of Li in LiAl and the experimental spectrum is poorer than for the Al spectrum. The broad low energy peak has upper and lower shoulders at about -4.6 eV and -6.4 eV that may be compared to the theoretical peaks at -5.0 eV and -7.0 eV respectively. Again the theoretical features lie lower than their experimental counterparts. The difference between the energy location of these peaks in the Li and Al spectra may be attributable to incorrect positioning of the fermi edge on one or both spectra, but no reasonable positioning puts the structures as low as the theoretical calculations. The experimental result suggest that the calculated band widths are too large by about 5 or 6%. The prominant high energy peak has a prominant shoulder at about -1.8 eV and a weaker structure on its trailing edge at about -3.0 eV. The latter small structure may coincide with the maximum in the p-spectrum, but no feature of the p-PDOS conincides with the shoulder at -1.8 eV. Some of the signal at the upper edge of the Li spectrum may come from free Li on the surface since the relative magnitude of the upper edge was variable from sample to sample.

The shoulder at -1.8 eV may result simply from a transition matrix element effect that is not properly accounted for in a PDOS calculation. The p electrons are involved in the valence bonding and thus are located primarily in the region between the atoms. Since the SXE spectra sample valence states that overlap onto the core wavefunctions, strong matrix element effects may be present.

Our major conclusions on LiAl are as follows:

1) We have found extreme sensitivity of the spectral features for both Al $L_{2,3}$ and Li K emission to the presence of excess Li on the surfaces.

2) The comparison of Al $L_{2,3}$ emission spectrum with calculated (s+d)-PDOS shows a good match except a broad hump appeared in experimental curve, which is centered at -2.5 eV from Fermi edge. It has the features of p-PDOS calculated by same author and may implies a breakdown of the selection rules for a disordered alloy system.

3) The fit between Li K spectrum and p-DOS is poorer than for Al $L_{2,3}$ spectrum. We attribute this effect to strong transition matrix element effect on a PDOS calculation.

LIST OF REFERENCES

LIST OF REFERENCES

[1.1] N. F. Mott, in Band Structure Spectroscopy of Metals and Alloys, D. J. Fabian, L. M. Watson eds. (Academic, Lodon, 1973).

[1.2] D. H. Tomboulian, in J. Quant. Spectrosc. Radoat. Transfer. (Pergamon, 1963). Vol.2, pp.649.

[1.3] H. W. B. Skinner, Phil. Trans., Roy. Soc. Lond. A239, 95 (1940).

[1.4] P. E. Best, in x-ray Spectroscopy, L. V. Azaroff ed. (McGraw-Hill, New York, 1974), p.3.

[1.5] P. Longe, in Adv. in x-ray Spectrosc., C. Bonnelle, C. Mande eds. (Pergamon, Oxford, 1982), p254.

[1.6] G. A. Rooke, in x-ray Spectroscopy, L. V. Azaroff ed. (McGraw-Hill, New York, 1974), p.173.

[1.7] G. D. Mahan, in Solid State Physics, H. Ehrenreich, F. Seitz, D. Turnbull eds. (Academic, New York, 1974), Vol.29, p.75; also G. D. Mahan, Phys. Rev. 163, 612 (1967).

[1.8] P. Nozieres, C. T. DeDominicis, Phys. Rev. 178, 1097 (1969).

[1.9] T. A. Callcott, D. L. Ederer, E. T. Arakawa, Phys. Rev. B18, 6622 (1978); also T. A. Callcott, E. T. Arakawa, Phys. Rev. B16, 5185 (1977).

[1.10] C. O. Almbladh, Solid State Commun. 22, 339 (1977); also Phys. Rev. B16, 4343 (1977).

[1.11] G. D. Mahan, Phys. Rev. B15, 4587 (1977).

[1.12] G. D. Mahan, Phys. Rev. B21, 1421 (1980).

[1.13] U. von Barth, G, Grossmann, Solid State Commun. 32,

645, (1979).

[1.14] R. Lasser, J. C. Fuggle, Phys. Rev. B22, 2637 (1980); also P. H. Hannah, P. Weightman, P. T. Andrews, Phys. Rev. B31, 6238 (1985).

[1.15] D. J. Sellmyer, in Solid State Physics, H. Ehrenreich, F. Seitz, D. Turnbull eds. (academic, New York, 1978), Vol.33, pp.83.

[1.16] B. L. Gyorffy, G. M. Stocks, in Electrons in Disordered Metals and on Metallic Surfaces, P. Phariseau, B. L. Gyorffy, L. Sheire, eds. (Plenum, New York,1979),pp.89-192.

[1.17] A. Bansil, H. Ehrenreich, L. Schwartz, R. E. Watson, Phys. Rev. B9, 445 (1974).

[1.18] H. Ehrenreich, L. Schwartz, in Solid State Physics, H. Ehrenreich, F. Sritz, D. Turnbull, eds. (Academic, New York, 1976), Vol.31, pp. 150-283.

[1.19] J. A. R. Samson, Techniques of Vacuum Ultraviolet Spectroscopy (John Wiley & Sons, New York, 1967).

[1.20] T. A. Callcott, K. L. Tsang, C. H. Zhang, D. L. Ederer, E. T. Arakawa, Rev. Sci. Instrum. 57, 2680 (1986).

[1.21] R. D. Carson, C. P. Frank, S. Schnatterly, F. Zutavern, Rev. Sci. Instrum. 55, 1973 (1984).

[1.22] J. A. Bearden, Rev. Mod. Phys. 39, 86 (1967).

[1.23] J. C. Ashley, C. J. Tung, R. H. Ritchie, Sur. Sci. 81, 409 (1979).

[1.24] H. J. Hagemann, W. Gudat, c. Kunz, J. Opt. Soc. Am. 465, 742 (1975).

[1.25] M. O. Krause, J. Phys. Chem. Ref. Data 48, 307 (1979).

[1.26] See the review article: J. R. Cuthill, in x-ray Spectroscopy, L. V. Azaroff ed. (McGraw-Hill, New York, 1974), p.3.

[1.27] J. H. Weaver, C. Krafka, D. W. Lynch, E. E. Koch, Opt. Prop. of Metals (Physics Data, Energie-Physik-Math. GMBH Gimbtt., Karlsurhe, FRG 1981)Vol.2, p.65.

[1.28] H. Winick, in Synchrotron Radiation Research, H. Winick, S. Doniach eds. (Plenum, New York, 1980), p.11.

[1.29] G. K. Green, BNL Reprot 50595, Vol.I, p.1-3, 1977.

[1.30] L. Golub, E. Spiller, R. J. Bartlett, M. P.Hockaday, E. R. Kania, W. J. Trela, R. Tatchyn, Appl. Opt. Vol.23, 3529 (1984).

[1.31] T. A. Callcott, D. L. Ederer, E. T. Arakawa, SPIE, Vol.447, 61 (1984).

[1.32] E. T. Arakawa, P. J. Caldwell, M. W. Williams, Opt. Engi. Vol.20, 753 (1981).

[1.33] P. J. Caldwell, E. T. Arakawa, T. A. Callcott, Appl. Opt. Vol.20, 3047 (1981).

[1.34] NSLS Parameters, Compiled by A. von Steenbergen, NSLS, 1986.

[2.1] L. Hedin, in Electrons in Crystalline Solids (Int. Atomic Energy Agency, Vienna, 1973), p.665.

[2.2] G. A. Rooke, in x-ray Spectroscopy, L. V. Azaroff ed. (McGraw-Hill, New York, 1974), p.173.

[2.3] L. M. Watson, R. K. Dimond, D. J. Fabian, in Soft x-ray Band Spectra, D. J. Fabian ed. (Academic, London, 1968), p.45.

[2.4] C. Kittel, Introduction to Solid State Physics, 5th ed. (John Wiley & Sons, New York, 1976), p.162.

[2.5] J. M. Ziman, Principles of the Theory of Solids (Cambridge Univ., 1964), p.116.

[2.6] G. Wiech, in Soft X-ray Band Spectra, D. J. Fabian ed. (Academic, London, 1968), p.59.

[2.7] G. D. Mahan, Phys. Rev. B21, 1421 (1980).

[2.8] U. von Barth, G, Grossmann, Solid State Commun. 32, 645 (1979).

[2.9] U. von Barth, G. Grossmann, Phys. Scr. Vol.28, 107 (1983).

[2.10] G. D. Mahan, in Solid State Physics, H. Ehrenreich, F. Seitz, D. Turnbull eds. (Academic, New York, 1974), Vol.29, p.75.

[2.11] P. H. Citrin, G. K. Wertheim, M. Schluter, Phys. Rev. B20, 3067 (1979).

[2.12] G. D. Mahan, Phys. Rev. 163, 612 (1967).

[2.13] P. Nozieres, C. T. de Dominicis, Phys. Rev. 178, 1097 (1969).

[2.14] R. P. Gupta, A. J. Freeman, Phys. Rev. Letters 36, 1194 (1976).

[2.15] T. A. Callcott, E. T. Arakawa, Phys. Rev. B16, 5185 (1977).

[2.16] J. A. Catterall, J. Trotter, Phil. Mag. 8, 1424 (1958).

[2.17] C-O. Almbladh, U. von Barth, J. Phys. C: Sol. State Phys. 8, 4117 (1975).

[2.18] W. F. Hanson, E. T. Arakawa, Z. Phys. 251, 271 (1972).

[2.19] E. H. Kennard, E. Ramberg, Phys. Rev. 46, 1040 (1934).

[2.20] J. Pirenne, P. Longe, Physica, 30, 277 (1964).

[2.21] P. Longe, A. J. Glick, Phys. Rev. 177, 526 (1969).

[2.22] G. A. Rooke, Phys. Lett. Vol.3, 234 (1963).

[2.23] same as Ref. [1.5].

[2.24] G. K. Green, BNL Reprot 50595, Vol.I,II, 1977.

[2.25] R. P. Madden, in X-ray Spectroscopy, L. V. Azaroff ed. (McGraw-Hill, New York, 1974), p.338.

[2.26] H. Winick, in Synchrotron Radiation Research, H. Winick, S. Doniach eds. (Plenum, New York, 1980), Ch.2,.3, p.11-60.

[2.27] R. D. Present, Notes of Classical Electrodynamics, The University of Tennessee, Knoxville, 1981.

[2.28] F. Wooden, Optical Properties of Solids (Academic, New York, 1972), p.28.

[2.29] M. Born, E. Wolf, Principles of Optics, 4th ed. (Pergamon, Oxford, 1970), p.40.

[2.30] D. E. Aspnes, S. M. Kelso, Nucl. Instrum. Methods, 95, 175 (1982).

[2.31] same as Ref. [1.19].

[2.32] J. R. Cuthill, in X-ray Spectroscopy, L. V. Azaroff ed. (McGraw-Hill, New York, 1974), p.145.

[3.1] T. A. Callcott, K. L. Tsang, C. H. Zhang, D. L. Ederer, E. T. Arakawa, Rev. Sci. Instrum. 57, 2680 (1986).

[3.2] T. A. Callcott, D. L. Ederer, E. T. Arakawa, Proposal submitted by the Univ. Tenn. to the NSF, March 1981.

[3.3] T. A. Callcott, D. L. Ederer, E. T. Arakawa, SPIE

Vol.447, 61 (1984).

[3.4] J. R. Cuthill, in X-ray Spectroscopy, L. V. Azaroff ed. (McGraw-Hill, New York, 1974), p.133.

[3.5] H. Haber, J. Opt. Soc. Am. 40, 153 (1950).

[3.6] The ray-tracing program, originally written by D. K. Prinz and W. R. Hunter of the Naval Research Laboratory, was modified by K. L. Tsang of the University of tennessee to accommodate toroidal and ellipsoidal mirrors and gratings and a variety of input geometries.

[3.7] Toroidal grating blanks and grating rulings were provided by Hyperfine, Inc., Boulder, CO.

[3.8] The image intesifier/converter consisting of MCP and FOB output optics mounted on a UHV flange was manufactured by Galileo Electro-Optics Corp., Sturbridge, MA.

[3.9] The CCD Si-diode array is a model TH 7861 manufactured by Thompson-SCF, Electron Tube Division, France.

[3.10] The FOB taper was manufactured by Galileo Electro-Optics, Sturbridge, MA.

[3.11] L. B. Lapson, J. G. Timothy, Appl. Opt. 15,1218 (1976); also J. A. R. Sampson, Nucl. Instrum. Methods, 222, 215 (1984).

[3.12] W. L. Hodge, B. C. Stratton, H. W. Moos, Rev. Sci. Instrum. 55,16 (1984); also R. F. Malina, Ph.D. thesis, Univ. Of California, Berkeley, CA, 1979.

[3.13] R. J. Fonck, A. T. Ramsey, R. V. Yelle, Appl. Opt. 21, 2117 (1982); also L. D. Owen, Bendix Technical Memo EOTM 108, May 1971.

[3.14] C. H. Zhang, T. A. Callcott, the Univ. of Tennessee, Knoxville, TN 37996 (unpublished data).

[3.15] The cooled CCD camera system, model 835 with cryogenic camera head CH 83-B, was manufactured by Photometries, Ltd., Tucson, AZ.

[3.16] J. A. Tagle, E. T. Arakawa, T. A. Callcott, Phys. Rev. B22, 2716 (1980).

[3.17] R. D. Carson, C. P. Frank, S. Schnatterly, F. Zutavern, Rev. Sci. Instrum. 55, 1973 (1984).

[4.1] J. B. Godel, J. C. Schuckman, Requirements and Guidelines for NSLS Experimental Beamline Vacuum Systems, BNL Report No.28073, July 1980.

[4.2] S. M. Heald, Nucl. Instrum. Methods 195,59 (1982).

[4.3] Standard Handbook for Civil Engineers, 3rd ed., F. S. Merritt ed. (McGraw Hill, New York, 1983), Ch.6.

[4.4] D. E. Aspnes, S. M. Kelso, J. Opt. Soc. Am. 8,997 (1981); also Nucl. Instrum. Methods 195, 175 (1982); also Proc. SPIE 315, 30 (1981).

[4.5] A. C. Parr, S. C. Ebner, SURF II Users Manual, 2nd ed. (NBS, Gaithersburg, MD 1986).

[4.6] J. H. Weaver, C. Krafka, D. W. Lynch, E. E. Koch, Opt. Prop. of Metals (Physics Data, Energie-Physik-Math. GMBH Gimbtt., Karlsurhe, FRG 1981) Vol.2.

[4.7] A. P. Lukirskii, E. P. Savinov, O. A. Ershov, Yu. F. Shepelev, Opt. Spektrosk. 16,310 (1964) [Opt. Spectrosc. 16,168 (1964)].

[4.8] P. J. Caldwell, E. T. Arakawa, T. A. Callcott, Appl. Opt. Vol.20, 3047 (1981).

[4.9] E. T. Arakawa, M. W. Williams, Phys. Rev. Lett. 36, 333 (1976).

[4.10] O. Aita, K. Tsutsumi, K. Ichikawa, M. Kamada, M. Okusawa, H. Nakamura, T. Watanabe, Phys. rev. B23, 5676 (1981).

[4.11] K. L. Tsang, C. H. Zhang, T. A. Callcott, D. L. Ederer, E. T. Arakawa (submitted to Phys. Rev.B).

[5.1] R. G. Osward, T. A. Callcott, Phys. Rev. B12,4122 (1971).

[5.2] U. von Barth, G. Grossmann, Phys. Scr. 28, 107 (1983).

[5.3] R. S. Crisp, S. E. Williams, Phil. Mag. 5, 1205 (1960).

[5.4] H. Neddermeyer, in Band Spectroscopy of Metals and Alloys, D. J. Fabian, L. M. Watson, eds. (Academic, London, 1973), p. 125.

[5.5] R. Lasser, J. C. Fuggle, Phys. Rev. B22, 2637 (1980)

[5.6] P. H. Hannah, P. Weightman, P. T. Andrews, Phys. Rev. B31, 6238 (1985); also M. Davies, P. Weightman, Phys. Rev. B30. 4183 (1984).

[5.7] same as ref. [1.16].

[5.8] A. Bansil, H. Ehrenreich, L. Schwartz, R. E. Watson, Phys. Rev. B9, 445 (1974); also Phys. Rev. B12, 2893 (1975).

[5.9] G. M. Stocks, J. A. Tagle, T. A. Callcott, E. T. Arakawa, Proc. Int. Conf. on X-ray Processes and Inner-shell Ionization (X-80), Stirling, Scotland, 25-29 Aug. 1980.

[5.10] C. Koenig, N. Stefanou, J. M. Koch, Phys. Rev. B33, 5307 (1986).

[5.11] J. E. Inglesfield, J. Phys. F: Metal Phys. Vol.2, 878 (1972); also J. Phys. F: Met. Phys. 9. 1551 (1979).

[5.12] J. C. Boisvert, P. W. Goalwin, A. B. Kunz, M. H. Bakshi, C. P. Flynn, Phys. Rev. B31, 4984 (1985).

[5.13] M. A. Ball, Md. M. Islam, J. Phys. F: Metal Phys. 14, 347 (1984).

[5.14] T. A. Callcott, J. A. Tagle, E. T. Arakawa, G. M. Stocks, Proc. of VUV-VI, Charlottesville, Va., 2-6 June, 1980. in App. Opt. 19, 4035 (1980); also J. A. Tagle, E. T. Arakawa, T. A. Callcott, Phys. Rev. B22, 2716 (1980).

[5.15] R. S. Crisp, J. Phys. F Met. Phys. 11, 1705 (1981).

[5.16] G. D. Mahan, Phys. Rev. B21, 1421 (1980).

[5.17] U. von Barth, G. Grossmann, Solid State Commun. Vol. 32, pp. 645 (1979); also Phys. Rev. B25, 5150(1980).

[5.18] L. C. Davis, L. A. Feldcomp, Phys. Rev. B23, 4269 (1981).

[5.19] L. Heden, in Electrons in Crystalline Solids (Int. Atm. Energy Agency, Vienna, 1973). p.665.

[5.20] M. O. Krause, J. Phys. Chem. Ref. Data 8, 307 (1979).

[5.21] T. A. Callcott, K. L. Tsang, C. H. Zhang, D. L. Ederer, E. T. Arakawa, Rev. Sci. Instrum. 57, 2680 (1986).

[5.22] H. S. Gotts, A. J. Glick, Phys. Rev. B23, 4337 (1981).

[5.23] G. A. Rooke, Phys. Lett. 3, 234 (1963).

[5.24] P. Longe, A. J. Glick, Phys. Rev. 177, 526 (1969).

[5.25] J. A. R. Samson, Techniques of Vacuum Ultraviolet Spectroscopy (John Wiley & Sons, New York, 1967), p.10.

[5.26] H. J. Hagemann, W. Gudat, C. Kunz, J. Opt. Soc. Am. 65, 742 (1975).

[5.27] J. C. Ashley, C. J. Tung, R. H. Ritchie, Surf. Sci. 81, 409 (1979). (Method of calculation are

illustrated for Al in this reference.)

[5.28] IMFP for core level excitation and SP for Mg may be calculated from data in E. J. McGuire, Phys. Rev. A16, 73 (1977).

[5.29] H. Neddermeyer, Phys. Rev. B13, 2411 (1976).

[5.30] G. D. Mahan, Phys. Rev. 163, 612 (1969).

[5.31] P. Nozieres, C. T. DeDominicis, Phys. Rev. 178, 1097 (1969).

[5.32] R. P. Gupta, A. J. Freeman, Phys. Rev. Letters, 36, 1194 (1976).

[5.33] W. F. Hanson, E. T. arakawa, Z. Phys. 251, 271 (1972).

[5.34] C-O. Almbladh, U. von Barth, J. Pys. C. 8, 4117 (1975).

[5.35] E. H. Kennard, E. Ramberg, Phys. Rev. 46, 1040 (1934).

[5.36] A. J. McAlister, Bull. of Alloy Phase Diagrams, Vol.3, 177 (1982).

[5.37] E. Zintl, G. Brauer, Z. Phys. Chem. B20, 245 (1933).

[5.38] J. Hafner, W. Weber, Phys. Rev. B33, 747 (1986).

[5.39] T. Asada, T. Jarlberg, A. J. Freeman, Phys. Rev. B24, 510 (1981).

[5.40] A. Zunger, Phys. Rev. B17, 2582 (1978).

[5.41] D. E. Ellis, G. A. Benesh, E. Byrom, Phys. Rev. B16, 3308 (1977).

[5.42] T. A. Callcott, E. T. Arakawa, D. L. Ederer, Phys. Rev. B16, 5185 (1977).

APPENDIXES

APPENDIX A

In Fig. A-1, a CCD-MCP detector M-M' is located nearly tangent to Rowland circle with diameter R (meters). δ is an added tilt angle between M-M' and tangent segment $\Delta\ell$ (mm). $\Delta\ell$ is determined by the source limited resolution $\Delta\lambda$(Å), which is the dominant factor limiting the spectrometer resolution, as may be determined by comparing eq. (2-54) with eq. (2-56). β is angle of exit light. Δx(mm) is the projection of $\Delta\ell$ on M-M'. Substituting eq. (2-56) in eq. (2-53), we obtain

$$\Delta\ell = \frac{\Delta S}{\cos\beta}\ 10^{-3}\ (\text{mm}). \qquad \text{(A-1)}$$

Since

$$\frac{\Delta\ell/2}{\sin(\pi/2 - \delta + \beta)} \cong \frac{\Delta x/2}{\sin(\pi/2 - \beta)}, \qquad \text{(A-2)}$$

we have

$$\Delta x = \frac{\Delta S}{\cos(\beta - \delta)}\ 10^{-3}\ (\text{mm}). \qquad \text{(A-3)}$$

Table A-1 lists calculated results from eq. (A-3), where, δ = 4.58, ΔS = 50μm, β_1 and β_2 are extreme angles limited by mechanical structure in our spectrometer. Suppose we need p

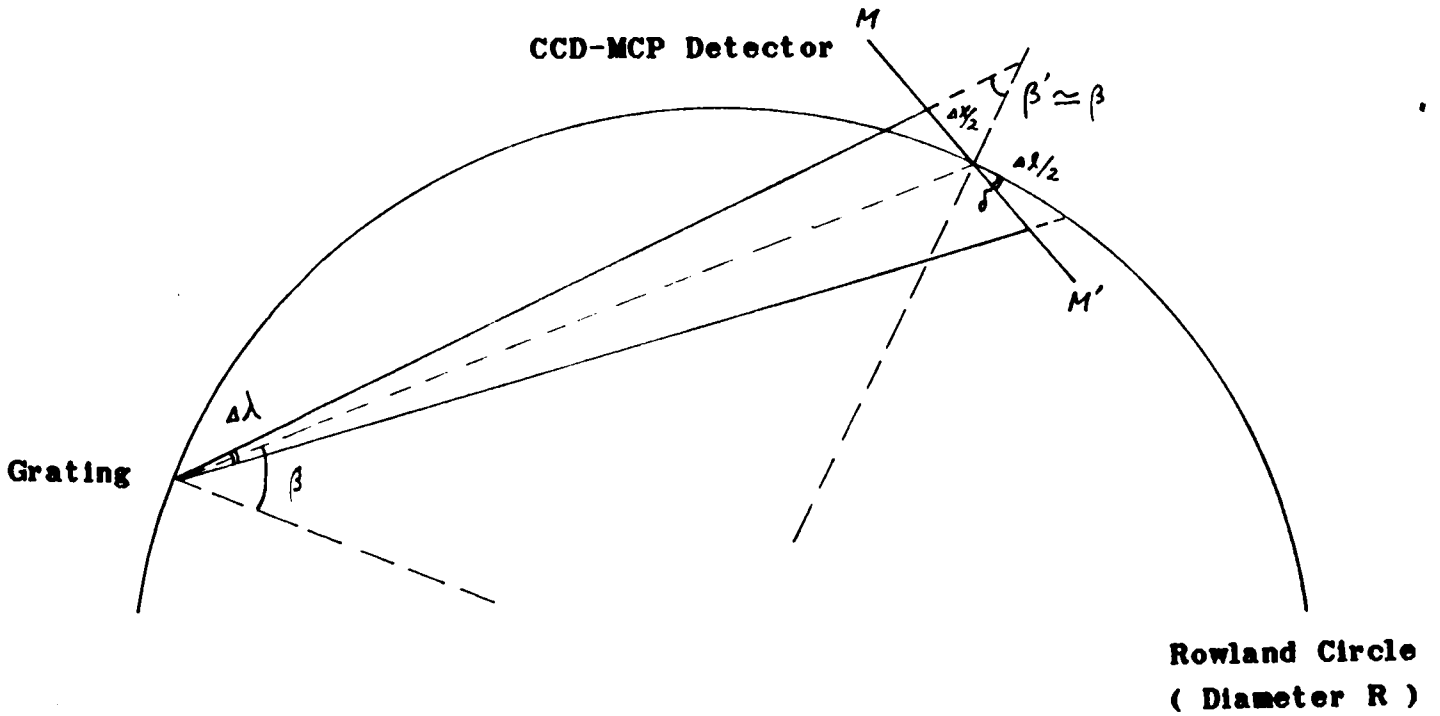

Fig.A-1
CCD-MCP detector system and the Rowland circle geometry.δ is an added tilt angle between the detector(M-M') and the tangent segment $\Delta\ell$ on the Rowland circle.

data points within the resolution $\Delta\lambda$, so the number of binned pixels n for a data point is

$$1 \leq n \leq \frac{\Delta x}{k\ t\ p}, \qquad \text{(A-4)}$$

where t is distance between two pixels (mm), k is amplification of fiber-optic bundles. Substituting eq. (A-3) in eq. (A-4), finally we obtain

$$1 \leq n \leq \frac{\Delta S}{k\ t\ p\ \cos(\beta - \delta)}\ 10^{-3}. \qquad \text{(A-5)}$$

In our spectrometer, k = 2, t = 2.2 X 10^{-2} mm, S = 50 μm. For maximum resolution, we have

$$1 \leq n \leq \frac{1.136}{p\ \cos(\beta - \delta)}. \qquad \text{(A-6)}$$

Table A-1

Calculated results of Δx, the projection of $\Delta\ell$ on M-M'

β	λ (Å)	ΔX (mm)
β_1 83.1°	80 (600 l/mm)	0.25
β_2 78.1°	320 (600 l/mm)	0.18

APPENDIX B

These methods have been used to calculate the transmission factor T(n), n = 1~128. In order to emphasize the essential features of these methods, the following discussion will employ a one-dimensional description. Assume x is the horizontal coordinate fixed on detector system in dispersion direction but having a tilt angle δ with respect to the Rowland circle. There are 128 discrete points along x; their coordinates are Δx, $2\Delta x$, $3\Delta x$ ....$128\Delta x$, where x is the distance on MCP surface between two points, which correspond to two adjacent data points in CCD, each of them consisting of 4 X 20 pixels. The intensity is read out on the computer terminal as I(n), n=1~128. Each n is for one data point connected with $x=n\Delta x$. It is assumed that read out noise and dark current have already been subtracted from each I(n). The remaining signal in I(n) includes the incident singal, random noise and scattering light. The fact that the scattering light is a function of x suggests that we need to obtain T(n) at different location on the Rowland circle. As concerns the random noise, we will show later that this problem can

be resolved to a great extent by method C which reduces noise by full use of the data obtained. Finally, we assume that a stable spectrum from a standard sample is distributed along the Rowland circle with intensity $I_0(n)$, n = 1~128. This distribution is fixed in space and is not dependent on the location of detector system.

Method A. Move detector system to the spectrum area and take two exposures $I_1(n)$ and $I_2(n)$ separated by one data point step. Refer to Fig. A-2, we have

$$I_1(n) = T(n)\, I_0(n), \qquad \text{(A-5)}$$

$$I_2(n) = T(n)\, I_0(n+1). \qquad \text{(A-6)}$$

Assume T(1) = 1, from eqs (A-5), (A-6) we get

$$T(1) = 1,$$

$$T(2) = \frac{I_1(2)}{I_2(1)}\, T(1),$$

.....

$$T(n) = \frac{I_1(n)}{I_2(n-1)}\, T(n-1),$$

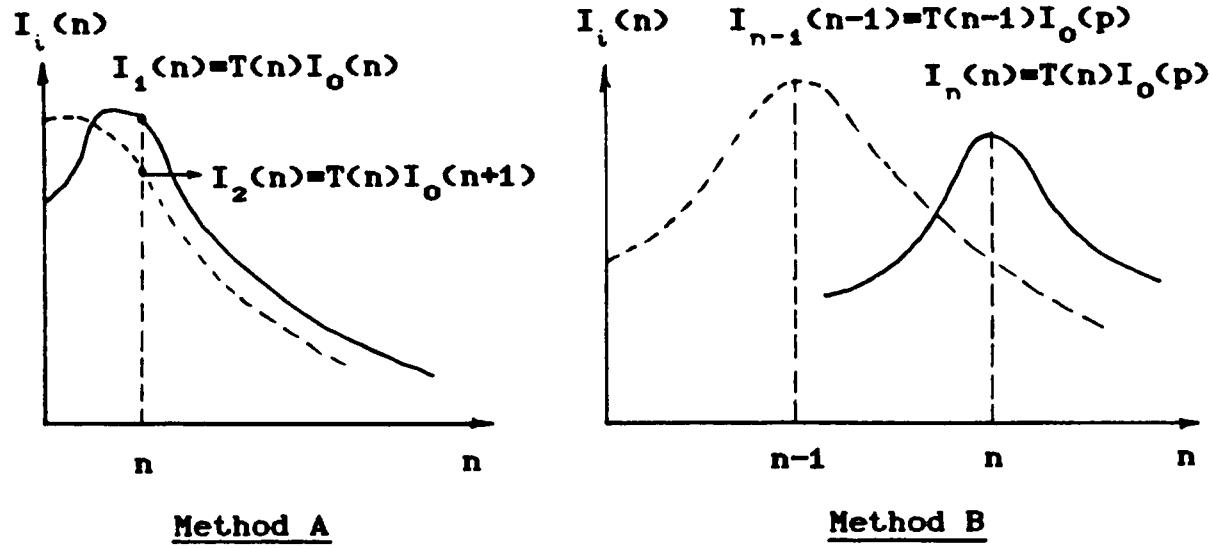

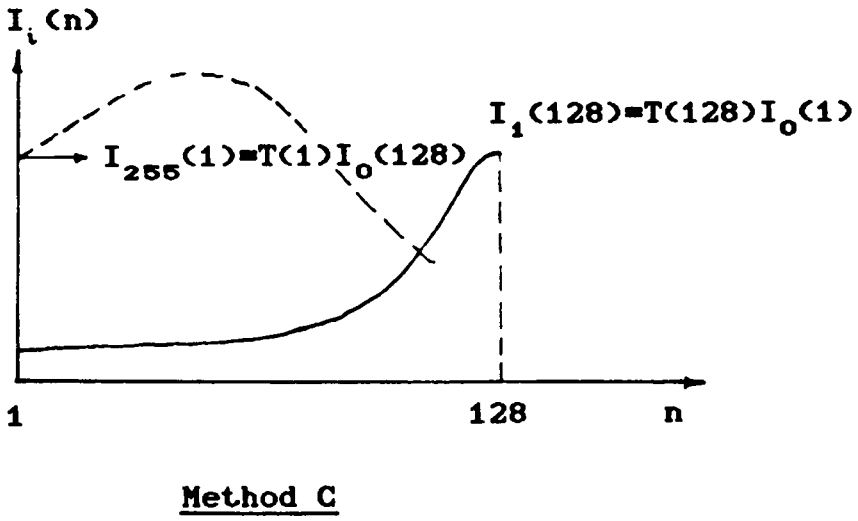

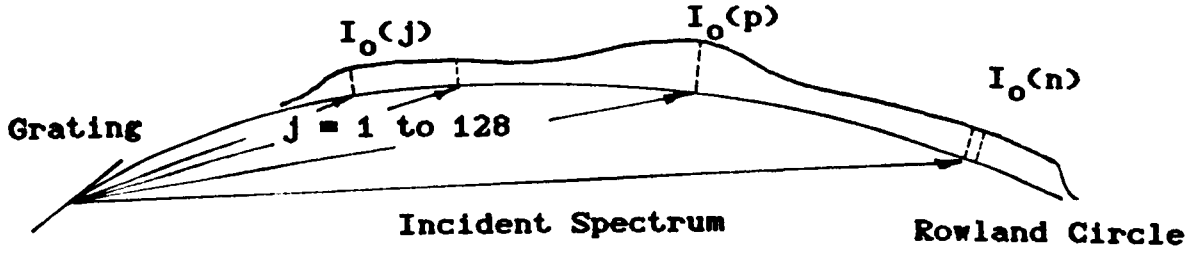

Fig. A-2
Scheme of measurement for transmission factor, T(n), of MCP-CCD system. $I_0(n)$ is the intensity distribution of incidence. $I_i(n)$ is the read-out distribution from the detector system.

or we write T (n) as the form

$$T(n) = \prod_{m=2}^{n} I_1(m) \Big/ \prod_{m=1}^{n-1} I_2(m). \qquad \text{(A-7)}$$

Although this method uses all the data available for only two consequtive exposures the big drawbacks are: a) Insufficant data results in very high random noise; b) There is an accumulative error due to eq. (A-7). Taking the logarithm of both sides of eq. (A-7) and differentiating we get

$$|\, d\, T(n)\,| = T(n)\left[\sum_{m=2}^{n} \frac{|dI_1(m)|}{I_1(m)} + \sum_{m=1}^{n-1} \frac{|dI_2(m)|}{I_2(m)} \right]. \qquad \text{(A-8)}$$

From eq. (A-8),we expect that a big error will be accumulated as n becomes large.

Method B. Move detector system to the spectrum area and take 128 exposures in such a way that a peak in an emission spectrum, $I_0(p)$, is scanned across the detector point by point as shown in Fig. A-2. Pick up one data per file, $I_n(n)$, we get

$$I_n(n) = T(n)\, I_0(p) \qquad \text{(A-9)}$$

with n = 1, ..., 128.

So the transmission factor T(n) can be written as

$$T(n) = \frac{n\, I_n(n)}{\sum_{n=1}^{128} I_n(n)}, \qquad \text{(A-10)}$$

where we have used

$$\sum_{n=1}^{128} I_n(n) = n\, I_0(p).$$

This method is a big improvement compared with method A, but the fluctuation due to the random noise still exists. We notice that the data available in each file is not efficiency used, since each data file supplies only one data point.

Method C. Refer to Fig. A-2, pick out smooth area on the emission spectrum with the intensities $I_0(j)$, j = 1,...128. Move the detector system across this area in such a way that the first distribution $I_1(n)$ only records one data from this area, i.e. $I_1(128)$ is the image of $I_0(1)$. In next step, $I_2(n)$ contains two data, i.e. $I_2(128)$, $I_2(127)$ correspond to $I_0(2)$, $I_0(1)$ respectively. We move 255 steps

to get 255 data files with the last file contained the image of $I_0(128)$ on $I_{225}(1)$. Then we make the following summations

$$\sum_{i=1}^{128} I_i(128) \cong T(128) \sum_{i=1}^{128} I_0(i),$$

$$\sum_{i=2}^{129} I_i(127) \cong T(127) \sum_{i=1}^{128} I_0(i),$$

$$\cdots\cdots\cdots\cdots\cdots\cdots\cdots$$

$$\sum_{i=128}^{255} I_i(1) \cong T(1) \sum_{i=1}^{128} I_0(i). \qquad \text{(A-11)}$$

Then the transmission factor T(n) becomes

$$T(n) = A \sum_{i=129-n}^{256-n} I_i(n), \qquad \text{(A-12)}$$

with n = 1, ...128.

Here we have used $A^{-1} = \frac{1}{n} \sum_{n=1}^{128} \sum_{i=129-n}^{256-n} I_i(n)$ instead of $\sum_{i=1}^{128} I_0(i)$.

In method C, we have most efficiently used the data available from the 255 data files; it combines the advantages of methods A and B.

The 2D problem can be solved just by applying the same

method to 16 columns to get total transmission factor. In practice, the double-point approach has been employed to determin T(n). Using method C, the detector system is moved 2 data points per step, each file supplies double information, and a total of 128 data files are needed.

VITA

Cheng Heng Zhang was born in Yunan, China on November 2, 1944. In August, 1967, he was graduated from Nanking University, Nanking, China, with a Bachelor of Science degree in Atmospheric Physics. After graduation, he worked in a semiconductor device manufacturing plant as an electronic engineer for nine years.

He enrolled in the graduate program of the University of Tennessee at Knoxville in March of 1981 and received the degree of Doctor of Philosophy in March of 1987 for investigations carried out in the field of solid state physics.

used to obtain the photon flux, this value is in satisfactory agreement with the 100 photon/s/800 pixel flux determined above.

Signal-to-noise Ratio. We have measured the signal to noise (S/N) ratio directly and show the results in Fig. 3-11. The S/N ratio was determined from the ratio of total signal level to high frequency scatter of data points. This plot was obtained by varying the integration time of the SX emission spectrum produced by a 20 μA, 2 kV electron excitation beam on silicon. S/N ratios were measured at 134.7Å with data summed over 4 X 200 pixel spectral slices in a manner similar to the other calibration procedures discussed above. Similar data were obtained by using a fixed integration time and varying the excitation current. The number of incident photons, shown on the second abscissa scale of Fig. 3-11, was estimated using our value of the proportionality constant (6.5 counts/incident photon) relating the number of counts from the detector system to the incident photon flux. The dashed line is a S/N proportional to N, where N is the total number of photons detected, that is characteristic of a photoemissive detector. Our measured S/N curve has a slightly